UNVEILING TRANSIENT BEHAVIORS IN HETEROSTRUCTURE NANOWIRES

UNVEILING TRANSIENT BEHAVIORS IN HETEROSTRUCTURE NANOWIRES

By JONATHAN PAUL BOULANGER, B.Sc.

A Thesis

Submitted to the School of Graduate Studies

in Partial Fulfillment of the Requirements

for the Degree

Doctor of Philosophy

McMaster University

© Copyright by Jonathan Paul Boulanger, July 2013

DOCTOR OF PHILOSOPHY (2013) McMaster University

(Engineering Physics) Hamilton, Ontario

TITLE: Unveiling Transient Behaviors in Heterostructure Nanowires

AUTHOR: Jonathan Paul Boulanger, B.Sc. Engineering Physics (Queen's University)

SUPERVISOR: Dr. R.R. LaPierre

NUMBER OF PAGES: xvi, 129

Abstract

GaAs/GaP heterostructure nanowires (NWs) were grown on GaAs(111)B and Si(111) substrates by gold (Au) assisted vapor-liquid-solid (VLS) growth in a molecular beam epitaxy (MBE) system. NW morphology and crystal structure were characterized by scanning electron microscopy (SEM) and transmission electron microscopy (TEM). Early results indicated substantial differences in the length and crystal structure of the GaAs/GaP heterostructures. Efforts to remove these inhomogeneities required an improved Au VLS seed deposition method as well as a better understanding of VLS growth across GaAs/GaP hetero-interfaces.

Experiments with GaAs/GaP heterostructures yielded the observation of changes in crystal phase in GaP, including the first reported occurrence of the 4H polytype. These observations revealed the presence of transient growth behavior during the formation of the GaAs to GaP hetero-interface that was unique to the VLS technique. Further characterization required the need to move from VLS seeds formed by annealing thin Au films to Au particles formed precisely by electron beam lithography (EBL). NW growth using EBL patterned Au seeds was discovered to be inhibited by the formation of a thin silicon oxide layer, formed at low temperatures by Au-enhanced silicon oxidation. Elimination of this layer immediately prior to growth resulted in successful patterned VLS growth.

A systematic study of the transient GaP growth behavior was then conducted using patterned arrays to grow GaAs/GaP heterostructure NWs with frequent, periodic oscillations in the group V composition. These oscillations were measured by high angle

annular dark field (HAADF) to determine the instantaneous growth rate of many NWs. A phenomenological model was fit to the data and transient growth rate behavior following a GaAs to GaP hetero-interface was understood on the basis of transient droplet compositions, which arise due to the large difference in As or P alloy concentrations required to reach the critical supersaturation.

Acknowledgements

I would like to express my gratitude to my friend and supervisor Dr. Ray LaPierre, who displayed great faith and trust in me from the very beginning. Even as a Master's student I was given a wide berth to explore and an amazing learning experience in managing my own project goals and results. Famously, his dedication to keep me as a PhD student persisted into the moments before submitting my Master's thesis. The fact this PhD thesis exists is proof. Ray's patience and commitment in the face of uncertain results and extravagant ideas will always be remembered. I would also like to thank my committee members Dr. Kitai and Dr. Kleiman for their helpful advice along the way.

This work would not have been possible without the great people of "Team LaPierre". Martin Plante and Subir Ghosh's foundational work on MBE nanowire growth were the basis for my work. I would also like to thank Chris Haapamaki, Andrew Chia, Parsian Mohseni, and Sandra Gibson for your advice, assistance, friendship, and willingness to listen to put up with me while I develop my (sometimes crazy) ideas.

Behind every paper, image, or nanowire growth was the great technical staff at McMaster University. Having bleeding edge technology is one thing, but having an amazing technical staff with the operational expertise to push it to the limits and keep it running is truly special. At the center of all my work was MBE growth. For this I would like to thank both Brad Robinson and Shahram Tavakoli, not only for dealing with what is at times one of the most maddening pieces of equipment, but for their sound advice and many helpful discussions. Next, I would like to acknowledge the Centre for Emerging

Device Technologies (CEDT) and specifically thank Doris Stevanovic and Zhilin Peng for keeping the clean room running (seemingly against all odds) and always promptly saving the day. As electron microscopy was my central analysis tool, I'd like to acknowledge the Canadian Centre for Electron Microscopy (CCEM) and thank Carmen Andrei, Fred Pearson, Chris Butcher, Julia Huang, Glynis de Silveira, Steve Koprich, and Andy Duft. I will always value the countless hours of operation, technical assistance, training, and discussion that made this thesis possible. I would also like to acknowledge the Toronto Nanofabrication Center (formerly ECTI) and Aju Jugessur, Edward Xu, Mariya Yagnyukova, and Harlan Kuntz. They displayed unmatched technical expertise within the area of electron beam lithography and on more than one occasion went the extra mile to complete a write job on a tight schedule. Finally, I'd like to thank the Department of Engineering Physics and CEDT: Marilyn, Samantha, Alexa, and Linda.

This work would not have been possible without funding. I would like to thank the Department of Engineering Physics at McMaster University, the Ontario Graduate Scholarships, and the Natural Science and Engineering Research Council of Canada. I would also like to thank the McMaster Create and the Photovoltaic Innovation Network.

Finally, I must thank my family and friends, their collective encouragement and support made this possible. To my mother and father, thanks for your unwavering support of my ongoing education over nearly 27 years. A few lines cannot express how much I appreciate all you have done for me. They say it takes a village to raise a child. The collective encouragement from my parents, uncles, and aunts towards the pursuit of science is undoubtedly responsible for where I am today.

A special thanks to Irina for standing with me and supporting me throughout all of this. One day, *after spending several months writing my Master's thesis*, I came home and said "I think I'll stay for a PhD". I think most reasonable people would have run screaming in exasperation, but she unequivocally supported me in that decision and handled it with grace when "one more year" turned into *three*. Irina pushes me to be more than "just an engineer" and I hope I can live up to that. Thanks so much for your support and for making my graduate school experience far more diverse in experiences and perspectives than I could have expected.

I dedicate this work to my family and friends

Table of Contents

Abstract iii

Acknowledgements v

List of Figures xii

1 Background 1

1.1 Introduction 1

1.2 Vapor-Liquid-Solid Growth 3

1.2.1 Fundamentals 3

1.2.2 Axial and Radial Nanowire Growth 7

1.2.3 Lattice Mismatch Accommodation 14

1.2.4 Crystal Structure 17

1.2.5 Nanowire Patterning 21

1.3 Motivations and Thesis Overview 22

2 Experimental Methods 25

2.1 Gas Source Molecular Beam Epitaxy 25

2.2 Characterization by Electron Microscopy 28

2.2.1 Electron Microscopy Fundamentals 29

2.2.2 SEM Analysis 30

2.2.3 TEM Analysis 32

2.2.4 STEM Analysis 33

2.2.5 Analytical TEM 36

2.2.6 TEM Sample Preparation 37

2.3 Electron Beam Lithography 39

2.3.1 Fundamentals 40

2.3.2 Summary of EBL Patterned Nanowire Growth Results 45

3 Axial GaAs/GaP Heterostructure Nanowires 50

3.1 Polytype formation in GaAs/GaP axial nanowire heterostructures 50

3.1.1 Introduction 50

3.1.2 Experimental Details 51

3.1.3 Results and Discussion 54

3.2 Summary 66

4 Patterned III-V Nanowire Growth on Si (111) Surfaces using Molecular Beam Epitaxy 68

4.1 Pattern Gold-Assisted Growth of GaP Nanowires on Si 68

4.1.1 Introduction 68

4.1.2 Experimental Details 69

4.1.3 Results and Discussion 72

4.2 Summary 82

5 Patterned GaAs/GaP Heterostructures with Group V Oscillations 83

5.1 Unveiling Transient Nanowire Growth Using Group V Oscillations 83

5.1.1 Introduction 83

5.1.2 Experimental Methods... 87

5.1.3 Results 91

5.1.4 Model Results... 95

5.1.5 Effect of V/III Ratio and GaP-to-GaAs transition 102

5.2 Summary 104

6 Conclusions and Future Work..105

6.1 Thesis Summary 105

6.2 Future Work 107

7 Bibliography 109

8 Appendix...117

8.1 Appendix A: Affine Transform Matlab Code 117

8.2 Appendix B: Electron Beam Lithography Procedure..................................... 117

8.3 Appendix C: Phenomenological Model Matlab Code 119

List of Figures

Figure 1.1. A simplified illustration of the VLS mechanism for NW growth. (a) A thin metallic Au film is deposited on a (111) wafer. (b) Upon annealing, the Au film alloys with the group III or IV elements present in the substrate, forming a eutectic with a melting point below the growth temperature. (c) The growth species are supplied through the vapor phase and preferentially diffuse towards the droplets increasing their level of supersaturation. (d) Preferential crystallization occurs beneath the droplets leading to single crystal pillars with matching diameters forming beneath. 3

Figure 1.2: A simulation of "self-regulated pulsed nucleation". The supersaturation increases due to the incorporation of group III and V adatoms. When the supersaturation nears the critical level, the probability for nucleation sharply builds. A single nucleation event followed by rapid island growth is likely to occur in the shaded window area. Afterward, the droplet is depleted of growth species and the supersaturation must again build to the critical level. Reproduced from [34]. 6

Figure 1.3: SEM (a, c) and TEM (b, d) images of (a, b) rod-like NWs formed under growth parameters that exclusively enabled VLS as the sole growth mode and (c, d) core-shell NWs formed under growth parameters than enable VS growth. 8

Figure 1.4: Axial heterostructures composed of GaAs and GaP. (a) – (c) HAADF images of a 10 period superlattice. (d) HR-TEM image with sufficient contrast to see the abruptness of the hetero-interfaces of only a few layers thick. While all images show some variance in the superlattice structure dimensions, (a) exhibits an extreme example of this. HAADF images have been bandpass filtered to remove noise. Scale bars indicate 10nm. 11

Figure 1.5: Radial heterostructures composed of GaAs and GaP. (a) High magnification HAADF showing the GaAs core, the alternating GaP/GaAs/GaP layers and finally the outer GaAs shell. The outer dark shell is the result of oxidation. (b) Demonstrates the impact of shadowing by nearby neighbors. (c) HR-TEM and (d) HAADF image of two NWs that began growing very close together. Prior to merging, shadowing resulted in a reduced growth rate of the sidewalls that were in close proximity - as indicated by the dark GaP hexagons. All scale bars indicate 20 nm. 12

Figure 1.6: The critical thickness (h_c) of mismatched axial heterostructures in NWs with radius r_o. Theoretical curves are marked as % mismatch. To the left of the vertical asymptotes the critical thickness is infinite. As $r_0 \rightarrow \infty$, the critical thickness approaches that of a 2D film. Reproduced from [61]. 15

Figure 1.7: Atomistic models of ZB, 4H, and WZ with the three different layer arrangements labeled A, B, and C. Reproduced from [65]. 18

Figure 1.8: Nucleation (a) probabilities and (b) rates for varying droplet compositions and a fixed droplet volume, temperature, contact angle, and nucleus positioning. $\Delta\mu_C$ represents the critical supersaturation whereby nucleation occurs at, but not below, and arbitrarily set to 300meV/pair. Reproduced from [39]. 19

Figure 2.1. A simplified illustration of the GS-MBE system used for the growth of all NW samples studied within this thesis. 27

Figure 2.2: Deposition of Au dots into SiO_2 wells. (a) A clean Si (111) wafer. (b) An SiO_2 layer may optionally be deposited by CVD or grown by thermal oxidation. Afterward a resist layer is applied through spin deposition. (c) The pattern is written by EBL and immersed in a solvent solution that dissolves the exposed areas only. (d) The SiO_2 layer is selectively removed by an etchant. (e) The surface is metalized by electron beam evaporated Au. (f) The resist and overlying Au film are lifted-off by ultrasonication in a solvent. The drawing is not to scale. 42

Figure 2.3: An annealing experiment performed with EBL written patterns. Annealing was conducted at 550°C. (a,c) As-deposited. (b,d) post anneal. (a,b) The Au "disks" alloyed with the Si substrate and became liquid forming either one or two droplets. Scale bar indicates 250 nm. (c,d) The larger shapes could not form a single droplet and instead formed many droplets, but retained the original shape. Scale bar indicates 10 µm. 46

Figure 2.4: (a) Preliminary EBL results. NWs appear randomly oriented. Intentional, vertical NW yield was near 0%. (b) NW array with greater than 90% yield along with some unintentional, thin NWs. Scale bars indicate 1µm. 47

Figure 2.5: GaAs patterned NW array with hexagonal symmetry and a 2 µm pitch. 48

Figure 3.1: Summary of MBE growth parameters for samples A-1 and A-2. Inset shows the gas switching sequence at a GaAs/GaP/GaAs segment (G.I. is growth interruption). 53

Figure 3.2: Cross-sectional SEM images of sample (a) A-1 and (b) A-2. The scale bar indicates 100 nm. 55

Figure 3.3: HAADF images of an A-2 NW with superimposed EDS linescan profiles (P: blue, Ga: red, As: green). Growth direction is from left to right. The lighter contrast segments are GaAs, while the darker are GaP. The segments from left to right are: GaAs base, 60 s GaP, 60 s GaAs, 40 s GaP, 40 s GaAs, 20 s GaP, 20 s GaAs, final 60 s GaP. Scale bar indicates 50 nm. 56

Figure 3.4: Sample A-1 and A-2 growth rates versus diameter for (a) GaAs and (b) GaP segments. The plots are placed in order of the segment growth durations: 60 s, 40 s, and 20 s from left to right. Open symbols indicate A-

1 NWs. Solid symbols indicate A-2 NWs. Circles: twinned ZB and WZ; diamonds: WZ with a low density of stacking faults. 57

Figure 3.5: Bright Field HR-TEM image of sample A-1, 115 nm diameter. (a) WZ with low stacking fault density (A-2 NW, 115 nm diameter). Scale bar indicates 10 nm. Insets contain power a spectrum from indicated area and the arrow points in the direction of growth. Hetero-interfaces were determined by HAADF images (not shown). 59

Figure 3.6: Bright Field HR-TEM image showing the polytypes observed in this sample A-2 NW, 28 nm diameter. Twinned ZB (t-ZB) is indicated by the long yellow line and middle power spectrum. The short yellow line at the NW tip indicates the ZB cooling neck. Scale bar indicates 10 nm. Insets contain power spectrums from indicated areas and the arrow points in the direction of growth. Hetero-interfaces were determined by HAADF images (not shown). 61

Figure 3.7: Schematic of different polytypes versus supersaturation (chemical potential difference $\Delta\mu$ between the Au-III-V droplet and the underlying solid) observed in the 60, 40 and 20 s segments of (a) GaAs and (b) GaP. The arrows indicate the observed range of phases in each segment and the trend with diameter or growth duration (increasing time). 62

Figure 3.8: HR-TEM image of 4H GaP following the 20 s GaAs/ final 60 s GaP hetero-interface. The power spectrums are taken from the shaded regions and indicate the WZ (top) and 4H (bottom) phases. Hetero-interfaces are marked according to HAADF images (not shown) and the growth direction is indicated by the arrow. The scale bar is 10 nm. 65

Figure 4.1: Plan view SEM image of EBL patterned Au seed particles formed by a 0.023 pC dose per Au dot. Scale bar is 1 µm. 70

Figure 4.2: SEM images of square symmetry, EBL patterned NW arrays formed by 0.023 pC/dot (a) – (c), 0.07 pC/dot (d) – (f), and 0.154 pC/dot (g) – (i). The left column shows sample A at normal incidence. The middle and right column show sample B at normal and 25° from normal incidence, respectively. The scale bars indicate 1 µm. 73

Figure 4.3: Plan view (a) and tilted view (b) SEM images of the lamella extraction area shown as a box in (a) and with a thin layer of carbon deposited in (b). (c) SEM image of the lamella after the ion milling of three windows labeled A, B and C from left to right. The scale bars indicate 1 µm. 75

Figure 4.4: DF-TEM image of a randomly oriented NW that grew outside of the patterned Au array. This NW was obtained from window A in Figure 3(c). This image shows a single crystal tilted GaP NW protruding from a surrounding polycrystalline GaP film. Scale bar indicates 100 nm. 76

Figure 4.5: TEM analysis of FIB cross-section of patterned NWs from sample A. (a) HAADF image of window C. NWs can be seen above each Au dot,

indicated by arrows, which is buried beneath a GaP film near the Si (111) substrate. (b) HAADF image of two NWs that originated from the right side of the Au dot (bright disk) where a film covering the Au dot is thinnest. (c) HAADF image showing the high-Z Au dot sunken into the Si substrate and covered by a low-Z film. (d) HR-TEM image of the Au dot in (c). The crystalline nature of the Si (111) substrate (bottom) and Au dot (middle) can be seen, but the overlying film (top) is amorphous. Scale bars are (a) 1 μm, (b) 100 nm, (c) 20 nm, and (d) 10 nm. 77

Figure 4.6: Composite HAADF image of an Au seed post-growth. The EDS linescan labeled “1” encompasses (from left to right) the GaP film, SiOx film, Au seed, and Si substrate. EDS linescan “2” encompasses the GaP film, SiOx film, Au residue, and Si substrate. EDS linescan “3” encompasses the GaP film and the Si substrate. Note that the P Kα1 and Au Lα1 x-ray peaks overlap, leading the EDS analysis software to misreport P in the Au seed in linescan “1”. The scale bar designates 20 nm. 78

Figure 5.1: Schematic showing different adatom incorporation pathways. A refers to direct impingement. B refers to sidewall impingement and diffusion to the droplet. C refers to substrate impingement and diffusion to the droplet via the sidewall. V is the nominal 2D growth rate and θ is the Ga impingement angle. 84

Figure 5.2: Samples used for the study of VLS growth of GaAs/GaP heterostructures. a) Sample A - GaAs. b) Sample B - GaP. c) Sample C - GaAs/GaP. d) GaAs/GaP/GaAs(V/III = 6)/GaAs(V/III=3). All samples were grown with the same 30 min duration of a GaAs base segment. 88

Figure 5.3: MBE group III and V impingement flux ratios normalized to Ga. a) Sample A. b) Sample B. c) Sample C, showing the procedure for forming a hetero-interface between GaAs and GaP as found in samples A and B, respectively. d) Sample D, showing the procedure used to reduce the V/III ratio. 89

Figure 5.4: 25-degree tilted SEM image of NW array from sample A. Scale bar is 1 μm. 92

Figure 5.5: a) HAADF image of a NW from sample B. b) Typical HAADF profile for sample B. 94

Figure 5.6: Left column shows β and R_{eff} values for several NWs. The right column shows the instantaneous growth rate as well as the separate contributions from direct impingement, sidewall diffusion, and substrate diffusion for a representative NW. Figures A) and B), C) and D), and E) and F) correspond to samples A, B, and C, respectively. The location of growth interruptions (hetero-interface) are indicated by grey shading. 96

Figure 5.7: The chemical potential difference per pair between the alloy droplet and the solid crystal ($\Delta\mu_{LS}$) at 600°C and several different Ga concentrations...... 98

Figure 5.8: $\Delta\mu_{LS}$ at 600°C and several different Ga concentrations. 101

Figure 5.9: a) β and R_{eff} values several sample D NWs. b) Instantaneous growth rate as well as the separate contributions from direct impingement, sidewall diffusion, and substrate diffusion for a representative NW. The location of growth interruptions (left: GaP-to-GaAs hetero-interface; right: V/III ratio changes) are indicated by grey shading. 103

1 Background

1.1 Introduction

The crucial role of semiconductors in the industries of computing, telecommunications, and energy has created an insatiable demand for increased performance and reduced cost. These demands are met by either expanding the capabilities of existing technology or by introducing new and sometimes radically different approaches. Progress within the semiconductor industry requires a shift from traditional top-down or thin film technologies. Future challenges will be met through bottom-up processes that combine the world of high performance III-V semiconductors with that of low cost manufacturing. A primary contender in this regard are epitaxially grown semiconductor nanowires (NWs).

In the last two decades NWs have received tremendous attention beginning with the first demonstration of nanoscale diameters (10-200 nm) and lengths measured in micrometers in 1991 [1,2]. It has since been demonstrated that the vapor-liquid-solid (VLS) mechanism for NW growth is possible under a number of epitaxial deposition technologies including molecular beam epitaxy (MBE) [3], chemical beam epitaxy (CBE) [4], chemical vapor deposition (CVD) [5], metal organic CVD (MOCVD) or metal organic vapor phase epitaxy (MOVPE) [1], and laser ablation [6]. Among these systems, the successful growth of group IV (Si, Ge) and group III-V (all known combinations of Al, Ga, and In with N, P, As, and Sb except AlSb) NWs has been achieved [7–15]. Moreover,

heterostructures and ternary combinations of these materials have been extensively demonstrated. Proof-of-concept devices have included light emitting diodes (LEDs) [16,17], lasers [18], photodetectors [19], solar cells [20–22], biosensors [23], wrap gate transistors [24,25], high electron mobility transistors (HEMTs) [26], resonant tunneling diodes (RTDs) [27], and single electron transistors [28]. Evidently, there is a massive potential for using semiconducting NWs in a broad range of applications.

In this Chapter, the primary concepts of NW fabrication are introduced. The fabrication method of choice within this study is the VLS mechanism, first proposed by Wagner and Ellis [5]. The growth of high aspect ratio single crystal semiconductor NWs presents the opportunity to explore different growth modes. Deposition conditions may be optimized to favor pure-axial VLS NW growth. Conversely, VLS growth may be limited in favor of thin-film-like growth on the NW sidewalls, termed radial growth. Both techniques may be used to create novel structures using doping or heterostructures [20,29]. Au-assisted VLS NW growth is described in section 1.2. A description of axial and radial growth in the context of NWs grown by the VLS mechanism follows in section 1.2.2. Crystal polytypism in VLS NWs will be introduced in section 1.2.3. The benefits of patterning VLS seeds for the fabrication of uniform NW arrays will be explored in section 1.2.5. This will lead to section 1.3, which describes the motivations behind the work presented, including an overview of the contents of this thesis.

1.2 Vapor-Liquid-Solid Growth

1.2.1 Fundamentals

The first description of single crystal semiconductor whisker growth was by Wagner and Ellis in 1964 [5]. The mechanism of high aspect ratio crystal growth was theorized to be the result of liquid metallic "impurities" on the substrate surface acting as preferential sites for crystal deposition during epitaxial growth. Since this first description of VLS crystal growth, significant progress towards modeling its behavior has been made [30–35]. It is now well understood that VLS growth is possible as a result of the selective incorporation of growth species onto the crystal surface beneath the metallic impurity particle. Consequently, the diameter of the metallic impurity determines the diameter of the newly formed, underlying crystal layers. As more layers are deposited, the metallic impurity ascends from the original substrate surface. This process is depicted in Figure 1.1.

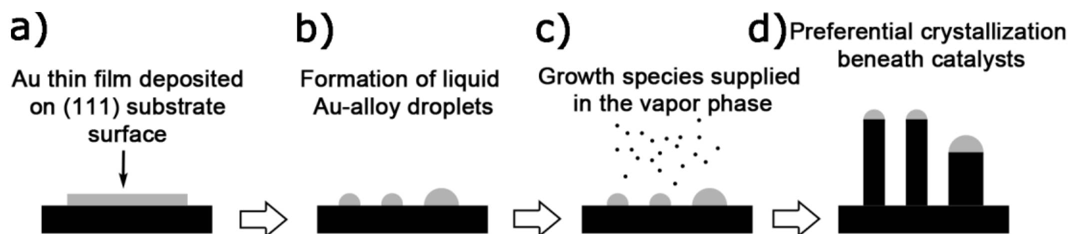

Figure 1.1. A simplified illustration of the VLS mechanism for NW growth. (a) A thin metallic Au film is deposited on a (111) wafer. (b) Upon annealing, the Au film alloys with the group III or IV elements present in the substrate, forming a eutectic with a melting point below the growth temperature. (c) The growth species are supplied through the vapor phase and preferentially diffuse towards the droplets increasing their level of supersaturation. (d) Preferential crystallization occurs beneath the droplets leading to single crystal pillars with matching diameters forming beneath.

The state of the impurity particle is traditionally liquid (hence the VLS moniker); however, NW growth has since been determined to be possible using solid metallic impurities through a vapor-solid-solid (VSS) mechanism [36]. VLS is also possible without a metallic impurity, but instead using liquid droplets of a crystal constituent, such as Ga or In [35,37]. In this thesis, gold (Au) assisted VLS growth is studied exclusively. Figure 1.1 shows the deposition of thin, solid Au films on the substrate. Upon reaching typical epitaxial deposition conditions for GaAs NW growth (500 - 600 °C), the Au film alloys with group III or group IV elements from the substrate surface. This process creates a eutectic alloy with a depressed melting point, resulting in the formation of Au-III-V alloy droplets as shown in Figure 1.1 (b). The further delivery of growth species in the vapor phase result in preferential collection, supersaturation, and incorporation beneath the droplets, Figure 1.1(c) and (d). Throughout this entire process, the VLS droplet stays on top of the growing crystal.

The droplet may act as a sink for growth species or chemical catalyst. In the case of NW growth by pre-cracked, elemental growth species under processes such as MBE, the droplet acts as a sink for adatoms on the substrate and NW sidewalls. Consequently, a positive diffusion flux of growth species towards the droplet will arise. NWs grown by this mechanism are said to be diffusion-induced. This behavior is explored in greater detail the subsequent chapter as well as section 5.1.

Epitaxial growth techniques that employ growth precursors that must be cracked on the substrate surface may use the droplet in a different manner. Instead of depositing elemental growth species uniformly over the substrate surface, growth

conditions may be optimized to selectively crack precursor molecules on the droplet surface only. In this case, the droplet is acting both as a chemical catalyst for the cracking of carrier molecules and a physical sink for atomic growth species. Therefore, the term catalyst is often used interchangeably with droplet, albeit often incorrectly in the case of MBE growth. The term seed particle or VLS seed is often more appropriate.

Substantial efforts have been expended to better understand the mechanics of VLS growth [31–35,38–40]. The current state-of-the-art description of the VLS method is that it is 2D nucleation limited and is described by the terms "nucleation anti-bunching" or "self-regulated pulsed nucleation" [33–35,38]. In either case, the terms describe nucleation from a nanovolume liquid, which will have the characteristic behavior depicted in Figure 1.2. When a droplet is under impingement by a molecular flux of growth species (eg. Ga and As_2), they will incorporate and the alloy droplet will gradually become supersaturated. As this supersaturation (ζ) increases, the probability for nucleation (P) will also increase; however, until a critical supersaturation is reached, nuclei formed will be less than the critical size and dissolve back into the liquid. Around a critical supersaturation, the probability of forming a 2D nucleus greater than the critical size will be very high. Following its formation, the nucleus will rapidly expand by incorporating adatoms at its edges until the entire layer has spread across the top facet of the NW. In this manner, NW growth proceeds as layer-by-layer growth. NWs with diameter much greater than 100 nm may have enough nucleation sites and growth material for polynucleation to occur [41]; however, the work in this thesis focuses on NWs that operate in the mononucleation regime as described above.

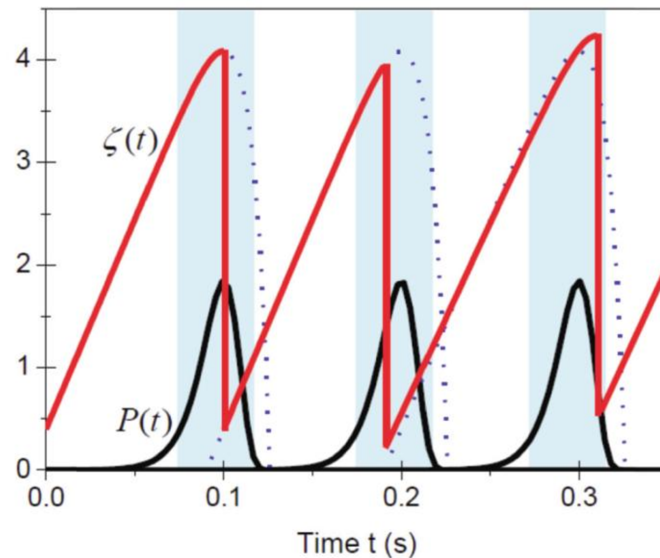

Figure 1.2: A simulation of "self-regulated pulsed nucleation". The supersaturation increases due to the incorporation of group III and V adatoms. When the supersaturation nears the critical level, the probability for nucleation sharply builds. A single nucleation event followed by rapid island growth is likely to occur in the shaded window area. Afterward, the droplet is depleted of growth species and the supersaturation must again build to the critical level. Reproduced from [34].

The formation of the 2D nucleus beneath the droplet is one of the most intensively discussed aspects of NW growth [31–35,38–40]. While the timing of the nucleation event has become agreed upon as discussed above, the location of the nucleus on the top facet of the nanowire holds great importance. Primarily, the nucleus location strongly dictates the atomic stacking sequence. This has major implications for the crystal structure of the NW and this will be discussed thoroughly in section 1.2.3. III-V VLS NWs typically grow in the energetically favorable [111] cubic or equivalent [0001] hexagonal crystallographic directions [3,42]. Therefore, VLS NW growth typically takes place on Si(111) or GaAs(111)B wafers such that they may grow perpendicular to the substrate surface (termed vertical); however, in the first order there are 4 equivalent

[111] directions above the substrate plane, which may also form if crystal phase twinning occurs [43].

1.2.2 Axial and Radial Nanowire Growth

As alluded to earlier, there are multiple growth modes possible during the growth of NW crystals by the VLS method. Growth conditions may be optimized such that VLS growth is favorable, albeit often in the presence of a rough (111) thin film. This method is generically termed axial NW growth, meaning NW growth will only occur beneath the VLS droplet. Growths employing axial NW growth exclusively will result in rod-like NWs where the diameter of the crystal corresponds almost exactly to that of the droplet. An example of axial NW growth is given in Figure 1.3(a) and (b). Growth conditions may also be optimized to promote vapor-solid (VS) growth on the NW sidewalls. This method is termed radial or core-shell NW growth. An example is given in Figure 1.3(c) and (d).

For MBE, axial NW growth is achieved by limiting vapor-solid (VS) growth on the NW sidewalls, which are typically six hexagonal {-1 1 0 0} or {-2 1 1 0} facets [44]. In this regard, growth conditions that discourage the formation of island nuclei on the sidewalls are desirable so long as VLS can continue to occur. Fortunately, the parameter window for GaAs VLS growth is very wide whereas the VS growth on the sidewalls occurs within a reduced set of these parameters. Experiments performed by Plante et al. demonstrated that high temperature (~600°C) and low or moderate V/III ratio (1.5-2.3) deposition conditions led to pure axial growth [45]. Conversely, low temperature and high V/III ratio led to tapered structures with significant sidewall nucleation, termed

radial growth. Furthermore, it was found that once the NW surpassed a critical length corresponding with the growth conditions, radial growth would occur, even under conditions that promote axial VLS growth over VS sidewall growth [3,30]. It is important to highlight that until this critical length was attained, no sidewall growth occurred and NWs sidewalls were smooth and without taper.

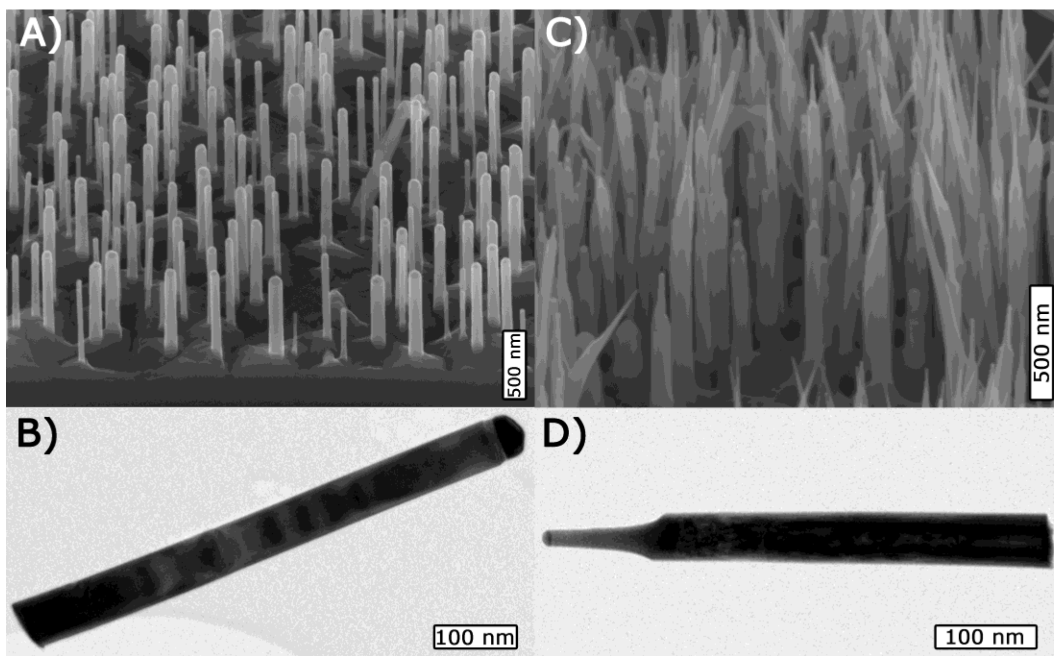

Figure 1.3: SEM (a, c) and TEM (b, d) images of (a, b) rod-like NWs formed under growth parameters that exclusively enabled VLS as the sole growth mode and (c, d) core-shell NWs formed under growth parameters than enable VS growth.

Experimental results concerning the onset of radial growth presented by Plante et al. were interpreted as a function of Ga diffusion lengths [3,30,45]. High temperature and low V/III flux conditions correspond to long Ga adatom diffusion lengths on NW sidewalls. Conversely, low temperature and high V/III ratio gave short diffusion lengths. This analysis was oversimplified and did not address the large disparity between the

experimentally determined diffusion lengths on typical NW sidewall facets {-1 1 0 0} and {-2 1 1 0}, typically quoted as 7 to 10 μm and as high as 19 μm [3,35], and the critical length when VS growth initiated on the sidewalls, typically less than 2 μm [30].

This simplified view of diffusion fails to account for VS sidewall growth that will occur when the driving force for vapor-solid, and thus adatom-solid, nucleation reaches a critical value and a stable island nucleus is formed [32]. The driving force for VS growth is the chemical potential difference between the sidewall adatoms and the NW sidewalls. The critical value of this chemical potential difference will be proportional to temperature, providing the expected result that solidification becomes more difficult at higher temperatures. In order for an island nucleus to form on the sidewall the supersaturation of the sidewall will need to increase the chemical potential difference beyond the critical value. To this effect, the growth temperature, V/III ratio, deposition rate, and NW length will all become factors in determining the supersaturation of adatoms on the sidewall surface. Models that compute the adatom surface density lead to highly complex expressions that require a multitude of assumptions and approximations regarding kinetic barriers, transition rates, and surface properties [32,35,46,47]; however, Plante et al. has already empirically determined the relationships as discussed. Evidently, decreasing the temperature, increasing the V/III ratio, and increasing NW length all lead to VS nucleation on the sidewalls either by increasing the supersaturation or by decreasing the nucleation barrier.

The utility of using axial NW growth to form structures is much like that for traditional thin film devices; a simple layer-by-layer structure can be formed. Along the

NW axis the composition can be altered through the introduction of impurity dopants or through changes in III and V growth species to form axial junctions.

Of particular interest in this work is using axial NW growth to make heterostructures of GaAs and GaP. These structures were created by switching the As_2 and P_2 sources during growth. Very abrupt hetero-interfaces can be formed using traditional MBE gas switching methods, which are elaborated in greater detail in sections 3.1.2 and 5.1.2. The As or P content in the alloy droplet is very low due to their poor solubility [48]. Moreover, the partial vapor pressure of the group V monomer and dimers, ie. As and As_2, are very high and result in fast desorption and removal from the system [35]. Consequently, when switching between As or P, there is an insufficient reservoir in the droplet to noticeably compromise the composition of the subsequent III-V bilayers and abrupt interfaces are therefore possible. Atomically abrupt hetero-interfaces are desired due to their superior electrical characteristics.

VLS NW growth is then perfectly suited for the formation of low dimensional, quantum well structures of GaAs/GaP and InAs/InP. For example, Figure 1.4 shows several GaAs/GaP quantum well superlattice structures. Figure 1.4(a)-(c) show high angle annular dark field (HAADF) images of three different NWs and Figure 1.4(d) is a high resolution transmission electron microscopy (HR-TEM) image that clearly shows structures only a few bi-layers thick can be formed. HR-TEM and HAADF techniques are discussed further in sections 2.2.3 and 2.2.4.

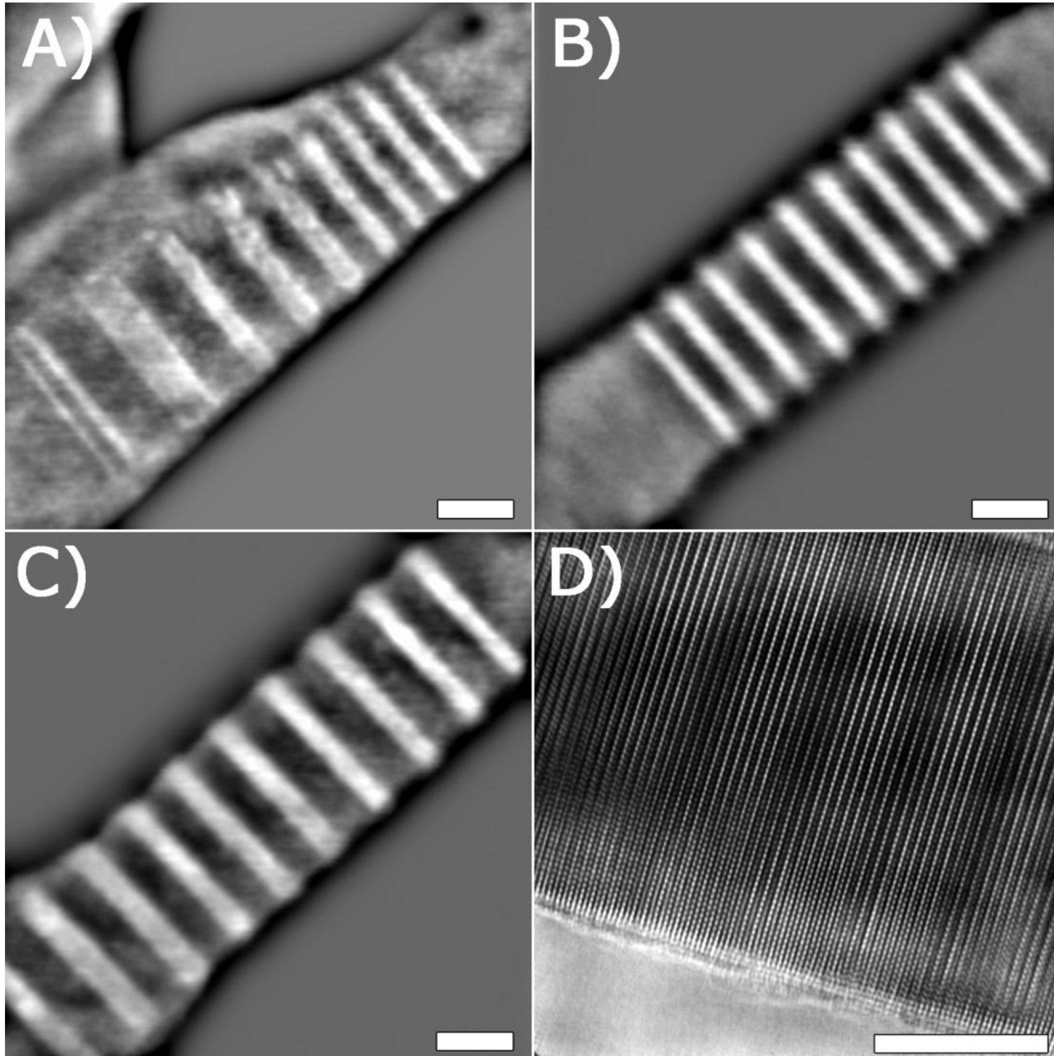

Figure 1.4: Axial heterostructures composed of GaAs and GaP. (a) – (c) HAADF images of a 10 period superlattice. (d) HR-TEM image with sufficient contrast to see the abruptness of the hetero-interfaces of only a few layers thick. While all images show some variance in the superlattice structure dimensions, (a) exhibits an extreme example of this. HAADF images have been bandpass filtered to remove noise. Scale bars indicate 10nm.

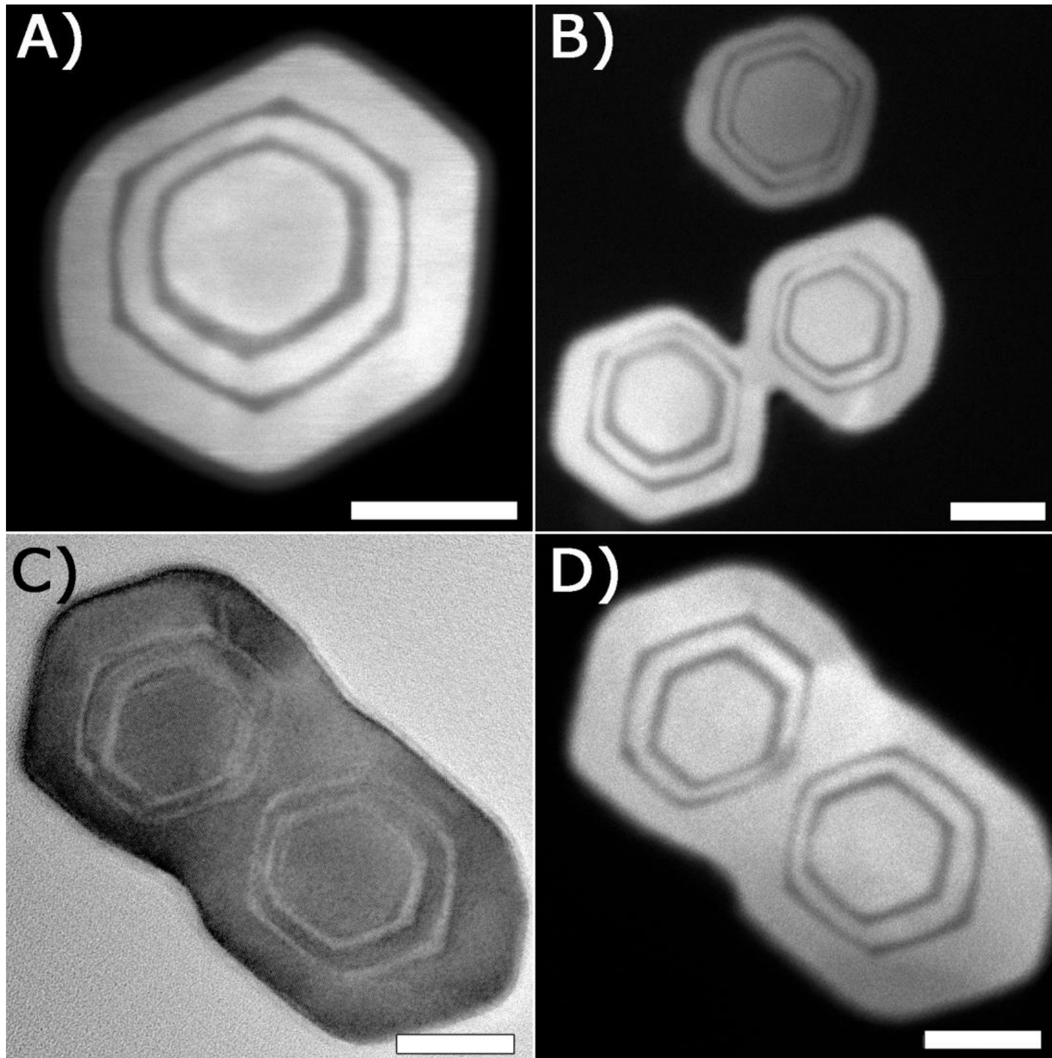

Figure 1.5: Radial heterostructures composed of GaAs and GaP. (a) High magnification HAADF showing the GaAs core, the alternating GaP/GaAs/GaP layers and finally the outer GaAs shell. The outer dark shell is the result of oxidation. (b) Demonstrates the impact of shadowing by nearby neighbors. (c) HR-TEM and (d) HAADF image of two NWs that began growing very close together. Prior to merging, shadowing resulted in a reduced growth rate of the sidewalls that were in close proximity - as indicated by the dark GaP hexagons. All scale bars indicate 20 nm.

Radial NW growth provides an entirely new domain of epitaxial semiconductor structure morphology that otherwise would be impossible to create using traditional

thin films. Whereas axial NW structures mimic their thin film counterparts, radial structures enable a new dimension of control by enabling the creation of so-called core-shell structures. By optimizing MBE growth parameters to enable VS growth on the NW sidewalls, radial growth will occur. The addition of dopants or different III and V materials enables the formation of diodes or heterostructures with this unique core-shell morphology. Radial heterostructures play a key role in enabling the electrical passivation of the NW surface, a vital component to many potential NW devices [49,50]. Figure 1.5 shows cross-sectional HAADF and HR-TEM images of core-shell NWs grown using radial growth.

Figure 1.4 and Figure 1.5 demonstrate the flexibility and precision of VLS NW growth. The fabrication of high quality, low dimensional structures with novel morphologies can be simple and borderline trivial; however, a closer look at those figures reveals the reality that these structures are not uniform; no two NWs are exactly alike. Disparities between NWs can be attributed to differences in diameter or proximity to nearest neighbors. When NWs grow in close proximity to one another, neighboring NWs can block or "shadow" each other from the impinging molecular beam. This can be plainly observed in Figure 1.5(b)-(d), where radial growth on sidewalls adjacent to neighboring NWs are clearly thinner than those without nearby obstructions. While MBE thin films can be made incredibly uniform across the surface of the substrate, this uniformity becomes lost during the relatively chaotic diffusion-induced VLS growth process. The NWs in Figure 1.4 and Figure 1.5 come from NW arrays like those shown in Figure 1.3. VLS seeds are randomly positioned with broadly varying diameters, which

lead to inhomogeneous growth conditions from NW to NW. This aspect is explored in greater detail in section 1.2.5. Lastly, in Figure 1.4, within every NW the length of every GaAs or GaP segment length differs slightly, some more dramatically than others. The variable growth rate within a NW was not expected and revealed the presence of unique VLS growth behavior.

1.2.3 Lattice Mismatch Accommodation

NW growth provides the opportunity to fabricate novel semiconductor heterostructures for a wide range of applications. The true novelty of these devices derives from the coherency of the interfaces despite the large lattice mismatch of the materials used. A myriad of such NW heterostructures have been demonstrated including (but not limited to) GaAs/GaP; InAs/InP; GaAs/InAs; GaAs/GaSb; and InSb with GaAs, InAs, and InP [9,29,50–57]. The large surface to volume ratio of NWs enables the growth of coherent, defect-free layers. The nearby presence of a free surface at the NW sidewalls permits the relaxation of elastic stress. Consequently, the effective critical thickness for mismatched layers is greater for NWs than a traditional 2D film.

Much work has been done to quantify the extent of lattice mismatch strain relaxation [50,58–64]. The behavior of mismatched layers in NW heterostructures is expected to be highly sensitive to the radius. Consider an axial heterostructure NW. In the limit of an infinitely large radius, the critical thickness should be equivalent to the 2D film critical thickness. In the limit of small radii it is expected that a critical radius exists for a given lattice mismatch, where for NWs with radii beneath this value the interface will remain coherent regardless of the layer thickness. This behavior was theoretically

determined by Glas, as shown in Figure 1.6 [61]. A NW with a radius below the critical value will have an infinite critical thickness for mismatched axial segments. As a result, coherent hetero-interfaces have been demonstrated with lattice mismatches as large as 7%, as shown by the solid data points in Figure 1.6. This is in stark contrast to 2D thin films, where finite critical thicknesses exist for lattice mismatches less than a fraction of a percent.

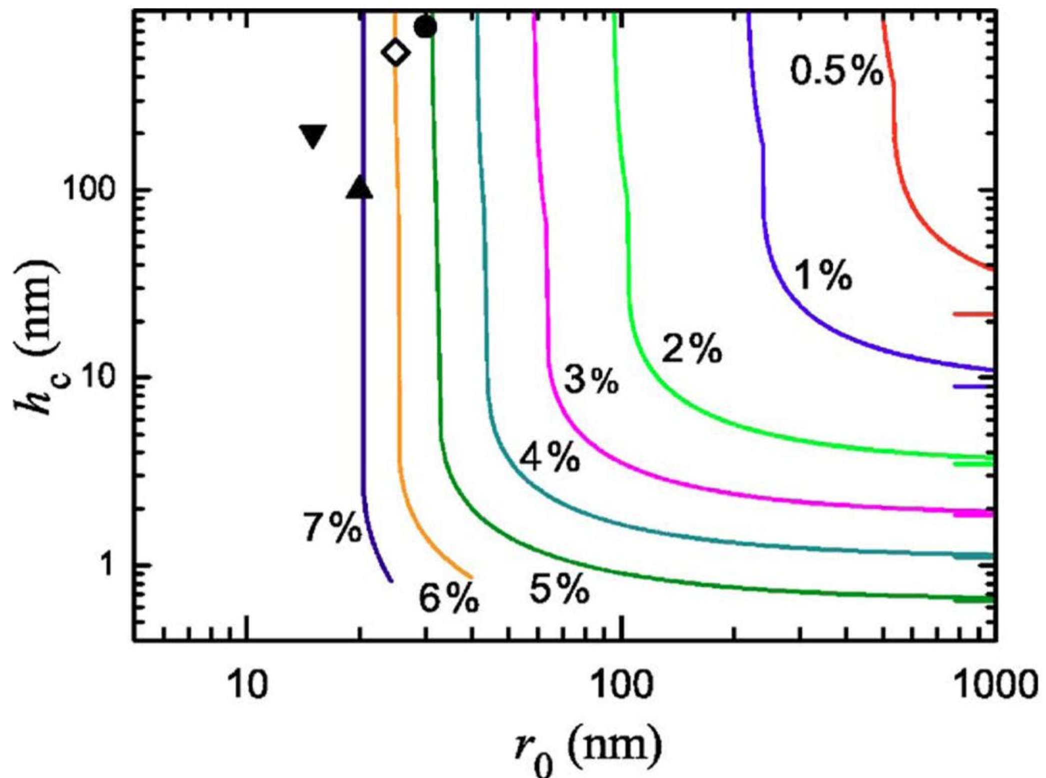

Figure 1.6: The critical thickness (h_c) of mismatched axial heterostructures in NWs with radius r_o. Theoretical curves are marked as % mismatch. To the left of the vertical asymptotes the critical thickness is infinite. As $r_0 \rightarrow \infty$, the critical thickness approaches that of a 2D film. Reproduced from [61].

While axial heterostructures closely mimic the geometrical arrangement of traditional thin films, radial heterostructures represent a novel arrangement. Once again, the proximity of the surface will allow for the elastic relaxation of strain, therefore reducing the lattice matching requirements for radial heterostructures as well. This behavior has been extensively modeled by Haapamaki et al. [50,56]. In the latter study, the existence of both a critical core radius and shell thickness was determined theoretically and compared to InAs/AlInP core/shell NWs. This mirrors the behavior of axial NW heterostructures discussed in earlier. For a NW with core radius less than the critical value, an infinitely thick shell can be grown without dislocations. In this circumstance, the strain energy in the core is insufficient to generate a dislocation. For a NW with a larger radius, the shell will be limited to a critical thickness.

Novel band structures have been predicted as a result of growing mismatched core-shell heterostuctures . Band alignments giving way to type-I, type-II, and type-III heterostructures as well as material transitions from semiconducting to metallic have been theoretically calculated. A plethora of possibilities lie in front of semiconductor device engineers upon the successful demonstration of controlled radial heterostructures.

Beyond the novelty of growing coherent, lattice mismatched structures, one of the most attractive aspects of III-V NW devices is the compatibility with growth on Si substrates [59]. The same relaxation of lattice matching requirements enables coherent NW growth on mismatched substrates. Thus the possibility for the direct integration of high performance III-V heterostructures with existing Si fabrication infrastructure is

closer to realization than ever before. This holds dramatic implications whether it is the integration of III-V optoelectronics onto Si CMOS devices or high performance photovoltaics or LEDs on affordable Si substrates.

1.2.4 Crystal Structure

Thus far much has been described about the nucleation mechanisms in VLS NWs. Axial NW growth proceeds layer-by-layer due to nucleation on the top facet of the NW crystal. There are three ways to spatially arrange an epitaxial III-V bi-layer on a (111) plane. These arrangements can be labeled A, B, and C. The different possible sequential combinations of these layers lead to different polytypes.

The simplest polytype is a repeating sequence of two layers, for example AB-AB-AB; CB-CB-CB; or AC-AC-AC. This polytype is designated 2H as it contains two repeating layers and the unit cell has a hexagonal symmetry. 2H is commonly called wurtzite (WZ). This polytype is commonly observed in bulk III-nitrides. The next polytype is a repeating sequence of three layers, for example ABC-ABC-ABC. This sequence is designated 3C as it contains three layers and the unit cell has a cubic symmetry. This is the most common sequence found in bulk III-V semiconductors, excluding nitrides. The final polytype considered here is a repeating sequence of four layers, for example ABCB-ABCB-ABCB. This sequence is designated 4H as it contains four layers and the unit cell is hexagonal. This polytype can be found in SiC thin films. It is interesting to note that the construction of the 4H sequence is an equal mix of cubic and hexagonal stacking. Making use of the prior example, ABC would result in cubic symmetry and BAB would result in hexagonal symmetry. This has important consequences with regards to the thermodynamics of

forming these sequences. The arrangement of the three layers needed to create these different crystal phases is depicted in Figure 1.7.

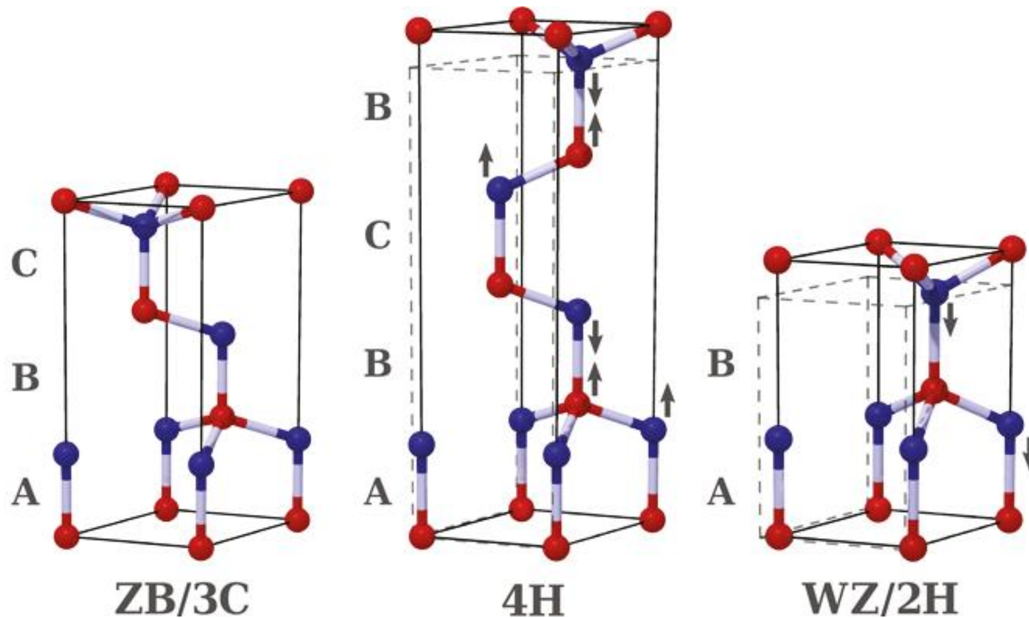

Figure 1.7: Atomistic models of ZB, 4H, and WZ with the three different layer arrangements labeled A, B, and C. Reproduced from [65].

A NW with a pure crystal phase would be composed of only one polytype. Pure WZ and ZB InAs NWs have been demonstrated [66]; however, the attainment of crystal phase purity for NWs across all III-V materials, deposition techniques, and seed types is far from a trivial affair as NWs typically exhibit stacking faults or rotational twins [51]. A stacking fault is considered to be an interruption of a regular stacking sequence. For example a C layer could be in inserted in the following WZ structure AB-AC-AB-AB. A rotational twin is a reversal or mirroring of the stacking sequence and are commonly

observed in ZB crystal structures, for example ABC-ABC-A-CBA-CBA [67]. Moreover, NWs that exhibit the 4H crystal phase only do so in brief segments [51,65,68,69].

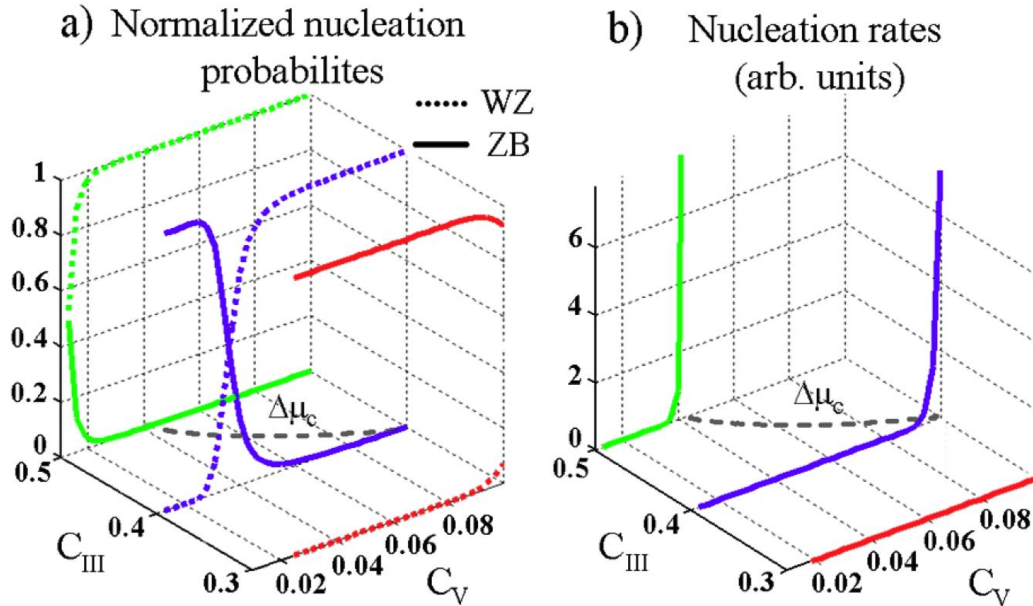

Figure 1.8: Nucleation (a) probabilities and (b) rates for varying droplet compositions and a fixed droplet volume, temperature, contact angle, and nucleus positioning. $\Delta\mu_C$ represents the critical supersaturation whereby nucleation occurs at, but not below, and arbitrarily set to 300meV/pair. Reproduced from [39].

The location of the nucleus determines the arrangement of the new III-V bi-layer on the underlying substrate. The nucleus may form entirely beneath the droplet and in the center of the (111)/(0001) facet. Alternatively, the nucleus may form in contact with the vapor, liquid, and solid phases, termed the triple-phase-line (TPL), by being positioned on the edge of the top facet. It has been determined that it is energetically favorable for nucleation to occur at the TPL [33,38]; however, if the liquid surface energy is sufficiently small and the droplet contact angle sufficiently large it may be

favorable for nucleation to occur away from the edge [39]. The formation of nuclei at the TPL is the source of polytypism during VLS NW growth whereas nucleation away from the TPL produces the polytype stable in the bulk [38], which is ZB for most III-Vs.

As nucleation is energetically favorable to occur at the TPL, this case must be examined further. Knowing that TPL nucleation occurs does not fully determine what crystal phase will form. Instead, many more factors remain in determining what arrangement the nucleus will have. Fixed factors for a set temperature, III-V material, and droplet composition include the liquid-vapor, solid-vapor (both the nucleus and the underlying NW), and solid-liquid (nucleus) surface energies. Also, a larger critical chemical potential difference between the liquid and solid phase ($\Delta\mu_{LS}$) is expected to enable the nucleation of WZ compared to ZB. At identical droplet compositions this occurs due to the higher volume free energy of WZ [70]. Other variables include the droplet volume, droplet contact angle above the nucleus, and the relative exposure of the vapor-facing edge of the nucleus to the sidewall facet or top facet [39]. Another important consideration is the initial diameter at the beginning of NW growth and the relative change in droplet composition, and thus volume, throughout growth. These parameters are all complex variables of the deposition conditions, and the exact prediction on where the nucleus will form is a topic beyond the scope of this thesis, but has been discussed thoroughly in others [35,71]; however, to give a sense of how polytypism arises during TPL nucleation, the normalized nucleation probabilities and nucleation rates for a particular droplet volume, temperature, contact angle, and nucleus position are plotted in Figure 1.8 as found in Ref. [39]. It can be seen that along

$\Delta\mu_C$, the critical chemical potential difference between the liquid and solid whereby nucleation occurs, Ga-rich droplet alloys will lead to a greater probability for WZ nucleation. This example serves to depict a simplified view of the source of polytypic behavior during VLS growth; however, these results are not directly applicable to experimental results as Ga concentration cannot increase freely for a fixed droplet volume, contact angle, and nucleus position.

1.2.5 Nanowire Patterning

Thus far NW growth has been described as arising from seed particles formed by annealing a thin film of Au. This process of self-assembly provides a relatively simple way to cover large areas of substrate with spatially random, 10 - 100 nm Au droplets. This process is inexpensive and requires only minimal wafer preparation prior to growth; however, the broad range of Au seed diameter and uncontrollable nearest neighbor distances lead to insurmountable complications to NW array uniformity and quality.

Therefore, a process to pre-pattern the Au seed particles prior to annealing must take place to form high quality NW arrays necessary for producing devices or conducting sensitive growth experiments. The objectives of this procedure are many-fold. First, NW growth by MBE is diffusion-induced such that growth behavior is dominated by the diffusion flux of adatoms. In this regard, pre-determining the spacing of NWs on the substrate surface will lead to an increased control over the growth environment in the early stages of growth. Furthermore, the effects of nearest neighbor shadowing of the impinging adatom flux, like that observed in the structures shown in Figure 1.5, can only be controlled and homogenized through the strict arrangement of

NWs on the substrate. Secondly, the growth rate of diffusion induced NWs are known to have an inverse radius dependence [3]. The accurate deposition of Au particles of a particular size will reduce the spread in NW diameter and thus length. Thirdly, the ability to control the diameter, length, and spacing of the NW array creates the opportunity to engineer its optical characteristics [72,73]. Fourthly, the engineering of adequate spacing between adjacent NWs allows for the uniform deposition of radial core-shell structures for doping, passivation, or other heterostructure devices [9,20,29,49]. Finally, the achievement of a uniform NW array will greatly simplify contacting of NW ensembles [74]. The process of forming patterned arrays of Au seeds are discussed at length in Chapter 2.3

1.3 Motivations and Thesis Overview

The motivations behind the work in this thesis stem from numerous sources within the overarching theme of improving the quality of NW arrays for device applications. As was outlined, several challenges stand in the way of fabricating an array of NW devices. At the beginning of this project, the single largest detriment to NW uniformity, crystal phase control, and reproducibility was the use of annealed Au films for the self-assembly of VLS seed droplets [3,30,51,74,75]. Furthermore, polytypism during NW growth by MBE has been a systemic problem in almost every material system. Efforts to address this issue were based on conducting series of growths under varying conditions not determined or even guided by the understanding of the impact growth conditions had on VLS growth behavior [45,51,52]. Finally, while novel mismatched heterostructure NWs were grown and reported in numerous instances,

there were few accounts of how such dramatic changes in growth conditions impacted VLS growth [69]. Therefore, the goal of this work was to enhance the overall state of MBE NW growth towards the formation of device quality arrays by improving the understanding and implementation of VLS growth mechanics.

The experimental methods used for the purpose of this study are first reviewed in Chapter 2. These include molecular beam epitaxy (MBE), wafer preparation for VLS growth, electron microscopy methods, and electron beam lithography for the patterning of VLS seeds. Chapter 3 identifies transient growth behavior and the resulting polytypism that may be associated with it. This study reports the first experimental observation of 4H GaP and suggests the change in crystal phase following GaAs/GaP hetero-interfaces are due to transient growth conditions. The entirety of this analysis was previously published in the Journal of Crystal Growth [51]. Chapter 4 elaborates on a phenomenon that is likely to be encountered when working with patterned arrays of Au nanoparticles on Si and how to counteract it to enable the formation of NW arrays with large vertical yields. This work was published in the journal Semiconductor Science and Technology [76]. Chapter 5 describes an extensive study regarding transient growth behavior surrounding GaAs/GaP heterostructures, relating this behavior to the underlying growth mechanics of VLS growth. This experiment required meticulous preparation, leveraging EBL patterned NW arrays and employing an advanced marker scheme produced by oscillating the composition of group V constituents in the NW along its axis. Extensive electron microscopy studies were performed to identify and subsequently model the transient behavior following GaAs/GaP hetero-interfaces. This

work is currently submitted for publication in the Journal of Crystal Growth. Finally, Chapter 6 will present the conclusions and suggested future work for the continued improvement of NW arrays grown by MBE.

2 Experimental Methods

2.1 Gas Source Molecular Beam Epitaxy

Within this study, molecular beam epitaxy (MBE) was exclusively used for the fabrication of III-V NWs. MBE is a form of crystalline film growth utilizing ultra high vacuum (UHV, 10^{-9} Torr) and atomic or molecular growth species. Due to the UHV conditions, growth species from evaporated or gas sources have a mean free path greater than the length of the chamber and do not undergo collisions with each other or with residual gases in the deposition chamber. In this way, the growth species form molecular beams. Most growth species condense onto the substrate while those that do not are either condensed on liquid N_2 cryopanels or evacuated by vacuum pumps. The molecular beam behavior is advantageous for the formation of semiconductor devices as growth species may be switched quickly, enabling the formation of atomically abrupt hetero-interfaces or doping profiles. The extremely low pressure conditions aids in the minimization of unwanted impurities within the growing crystal.

Growth species typically originate from solid effusion cells or gas sources. The former consists of high purity solid elements that are resistively heated such that their vapor pressure is increased until the desired molecular flux is obtained. The magnitude of the molecular flux may be controlled by the effusion cell temperature whereas the cell can be switched on or off by shuttering via mechanical means. Effusion cells in the McMaster system are used for group III sources as well as n and p-dopants (see Figure 2.1). While group V species may also be supplied from solid effusion cells, the McMaster

system makes use of the thermal decomposition (cracking) of group V hydride gases. MBE systems such as this are referred to as gas source MBE (GS-MBE) or hydride-source MBE. The replacement of solid group V sources by gas sources was first proposed by Panish in 1980 and has since become a well developed technique [77,78]. The advantage of a gas source for group V's is that the flux is determined by fast-acting mass-flow controllers for each hydride species as opposed to the slow-reacting resistive heating elements on solid effusion cells. Hydrides are thermally decomposed by a cracking cell. In the case of the McMaster GS-MBE, both P and As containing hydrides are cracked by a single cracking cell. The composition of the cracked products and by-products is determined by the temperature and pressure of the cracking cell. The cracking cell of the McMaster GS-MBE operates at 950 °C and under conditions such that the molecular flux is primarily group V dimers (P_2 and As_2). Unwanted byproducts such as atomic species (P and As), tetramers (P_4 and As_4), atomic hydrogen and hydrogen containing molecules (PH and AsH) will also be present, but at low levels.

A simplified representation of the McMaster GS-MBE system is shown in Figure 2.1. This system was built by SVT Associates under the custom specifications of Dr. Brad Robinson, McMaster University's epitaxial growth specialist. The substrate growth surface faces the bottom of the system where the hydride gas cracker and effusion cells are located, directed at an angle of 35° to the surface normal. Temperature control is accomplished via a thermocouple attached to the stage (not shown) and a pyrometer. The thermocouple provides sufficient control of growth temperature and is calibrated using standard thin film samples. While the pyrometer provides high accuracy

temperature measurement during thin film growth, the presence of NWs renders this measurement technique less effective due to the light trapping properties of NWs. Not shown in Figure 2.1 are the liquid N_2 cryopanels that surround the stage for the purpose of trapping atomic and molecular species that do not remain condensed on the substrate surface.

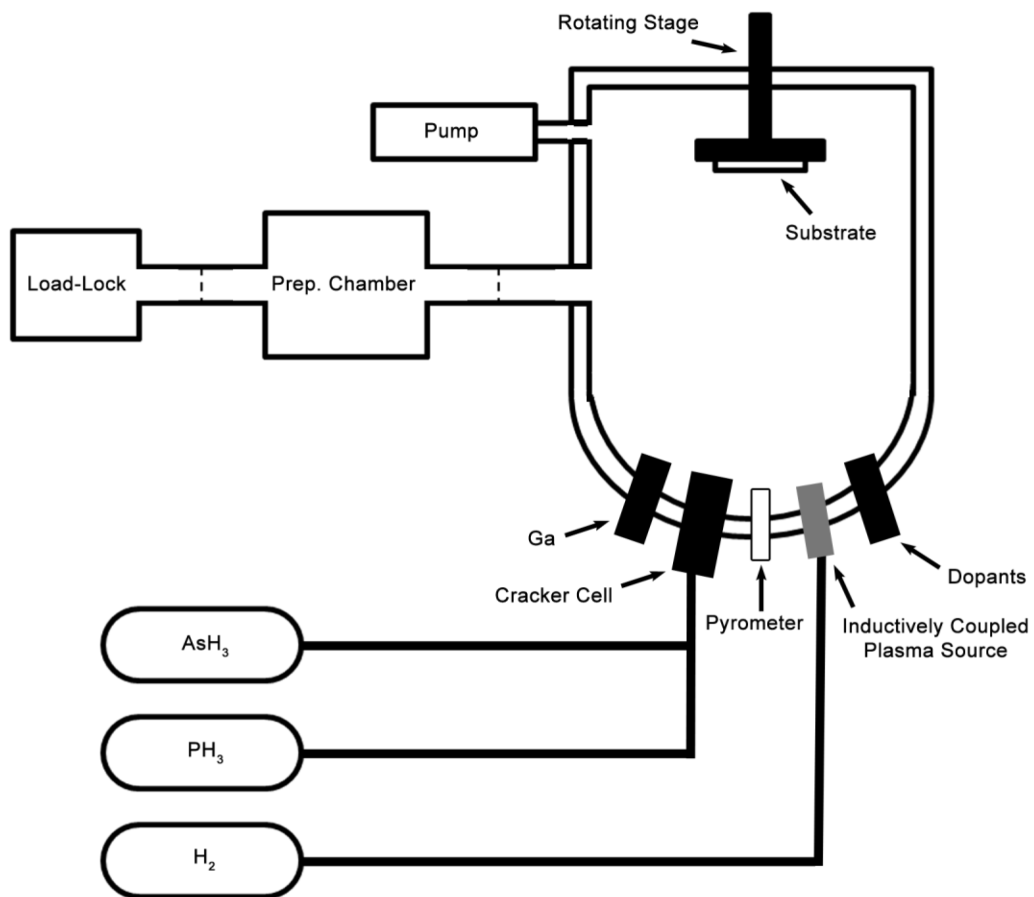

Figure 2.1. A simplified illustration of the GS-MBE system used for the growth of all NW samples studied within this thesis.

NW growth will only be initiated during MBE deposition if the substrate is adequately prepared. For Au-assisted VLS, Au seeds need to be distributed across the substrate. There are multiple approaches to accomplishing this goal, as alluded to in Chapter 1. The primary methods in this work were either self-assembled droplets from annealed Au thin films and lithographically patterned Au seeds. These methods are discussed in greater detail insections 3.1.2 and 2.3, respectively. A review of several Au nanoparticle preparation methods, including thin film annealing and EBL, is given in Ref. [79].

2.2 Characterization by Electron Microscopy

The principle tools for the analysis of NWs in this study are derivatives of electron microscopy. In particular, two types of information were sought. First, information was obtained regarding the surface morphology and distribution of NWs as-grown on the substrate. Second, high resolution structural information was sought so as to reveal the crystal phase, defects, elemental contrast, and interface abruptness. Unfortunately, no single instrument can achieve both goals simultaneously. Scanning electron microscopy (SEM) was used for the characterization of as-grown NW morphology whereas transmission electron microscopy (TEM) was implemented for structural and compositional information along with accompanying techniques such as scanning transmission electron microscopy (STEM), energy dispersed X-ray spectroscopy (EDS) and electron energy loss spectroscopy (EELS). A brief description of the fundamental operating principles is presented in the following. Information specific to the measurement of NWs is also given where relevant.

2.2.1 Electron Microscopy Fundamentals

Microscopy, using electrons in place of photons, permits the detailed analysis of structures much smaller than the wavelength of visible light. This is made possible by the wave-particle duality of the electron, which was first proposed by de Broglie and independently verified by subsequent experiments [80]. The wavelength λ of the electron with momentum *p* is expressed by the following:

$$\lambda = \frac{h}{p} \tag{2.1}$$

where *h* is Planck's constant (6.626 x 10^{-34} J s). Therefore, the wavelength of an electron of rest mass m_e is effectively controlled through its velocity. An electron has a negative elementary charge *e*. When passed through an accelerating electric potential *V*, the kinetic energy imparted to the electron is equivalent to the product of the electric potential and the elementary charge, with units eV. The velocity *v* and momentum of the electron is related to the kinetic energy through Equation (2.2).

$$p = m_e v = \sqrt{2m_e eV} \tag{2.2}$$

At accelerating voltages exceeding 100 kV, it becomes necessary to account for relativistic effects as the electron velocity approaches the speed of light *c* (2.998 x 10^{8} m/s):

$$\lambda = \frac{h}{\sqrt{2m_e eV\left(1 + \frac{eV}{2m_e c^2}\right)}} \tag{2.3}$$

At even modest accelerating voltages experienced in an SEM (typically between 5 and 30 kV), the electron wavelength is much less than the spacing between atoms (between

17.3 and 7.1 pm, respectively). Typical TEM accelerating voltages are 120, 200, and 300 kV, which corresponds to a smallest wavelength of about 2 pm . Unlike optical microscopy, the wavelength of impinging electrons is no longer the limiting factor. Chromatic and electro-magnetic lens aberrations severely limit the practical resolution of an electron microscope. Furthermore, surface topology and composition also dramatically impact the achievable image resolution.

2.2.2 SEM Analysis

An SEM image is formed through the collection of backscattered or secondary electrons (SE) generated from the primary electron (PE) beam as it interacts with the sample. Within the studies encompassed by this thesis, imaging was exclusively accomplished via SE. These are very low energy electrons that have been knocked free from the valence bands of atoms within the material of interest. SE are typically only collected from a thin layer (about 10 nm) near the sample surface as SE generated deeper in the material have insufficient energy to escape. Therefore, images formed from SE signals give excellent topographical information; however, complications arise with low dimensional structures like NWs, where the PE beam does not terminate within the structure but transmits or scatters outside.

The penetration depth of the PE beam far exceeds the width of a typical NW (less than 100 nm). Therefore, SE are collected not only from the surface initially penetrated by the PE beam, but from the entire circumference of the NW. Additional SE are collected from neighboring NWs which receive the transmitted or scattered PE. The image formed under such a situation yields a loss of detail. As the beam is scanned

across the area of interest, the SE signal collected at any given time is composed of far more SE than originated from the front facet of the NW. To mitigate this issue, the use of the lowest accelerating voltage (3 - 5 kV), beam current (~100 pA), and working distance (6mm for normal, 8mm for 25° tilted) works to reduce the PE spot size as well as the strength of the unwanted SE signals and was found to achieve the best image quality.

Outside the optimization of the operating conditions for the sample morphology, the SEM is generally limited by the diameter of the electron probe as it enters the solid surface [81]. This will be determined by beam parameters such as brightness, energy, energy spread (ΔE); lens parameters such as spherical (C_s) and chromatic (C_c) aberration coefficients; and operating conditions such as probe current and aperture angle. The JEOL JSM-7000F was equipped with a field emission electron gun (FEG) and used exclusively in this thesis by the author. The use of a FEG produces a brighter source from a smaller point that has a reduced ΔE compared with thermionic emission from traditional tungsten or LaB_6 sources. Lens aberrations will ultimately limit the beam diameter. In general, the spherical aberration (C_s) limits resolution above 5 kV whereas the chromatic aberration in conjunction with ΔE will be limiting below 5 kV [81].

NW samples were affixed to a variety of SEM stubs for different purposes. When plan view or moderate tilts (up to 45°) were required, a flat stub with screw-tightened clamps were used. No additional conductive paste or tape was necessary. When greater tilt angles were desired, such as 90° cross-sectional views, 45° SEM stubs were

used. This was required as the SEM sample stage does not permit 90° tilt. By mounting samples on a 45° angle, all angles within 0 to 90 ° could be viewed within a tilt range of 45° and in conjunction with a 180° stage rotation. Due to the difficulty of mounting a small piece of NW covered substrate onto a 45° angled stub, both double-sided carbon tape and silver paint are used. The edge of the substrate is allowed to hang over the 45 ° lip on the top facet of the stub.

2.2.3 TEM Analysis

In contrast to the relatively low energy electrons used in SEM to observe the surface topology and morphology of NWs, TEM uses higher energy electrons (usually greater than 100 kV) to transmit through thin specimens (less than 200 nm). The interaction between the high energy electrons and the NW crystal provides insight into its structure and composition. Conventional TEM (CTEM) in bright field (BF) mode combines amplitude and phase information from transmitted and diffracted electrons to simultaneously reveal the specimen density, thickness, or elemental composition along with its crystal structure [80]. If the objective aperture is positioned such that only diffracted electrons from a particular lattice plane are collected then a dark field (DF) image is produced. In this case the transmitted beam is blocked and therefore regions that do not diffract electrons through the objective aperature cannot show brightness contrast. At high magnifications referred to as high resolution TEM (HR-TEM), Bragg reflections from numerous crystal planes are combined to produce lattice fringes, which communicate information regarding crystal phase and the presence of dislocations. It is important to highlight that despite the resemblance to the atomic lattice, HR-TEM

images do not infer the actual position of atomic columns in a crystalline solid. Such information may only be interpreted after the TEM operating conditions are carefully assessed [80]. CTEM and HR-TEM are extensively used within this thesis to characterize the crystal structure of NWs.

Another useful TEM method for the characterization of crystal structure is selected area diffraction (SAD). This method permits, through the use of apertures in front of the sample, the collection of electron diffraction information from small areas. Diffraction patterns are collected digitally by changing the strength of the intermediate lens beneath the sample such that the back focal plane instead of the image plane is projected [80]. Similar information may also be collected from HR-TEM images by performing a fast Fourier transform (FFT) of a region of interest.

2.2.4 STEM Analysis

A complementary technique to TEM is scanning transmission electron microscopy (STEM). Here the electron beam is raster scanned like the beam in an SEM. The resolution of this technique is largely based on the probe size. In a typical FEG STEM the probe size can be less than 0.3 nm [80]. Unlike with SEM, broadening of the PE beam in the sample is minimal with such high accelerating voltages and thin foil samples. A planar detection device is no longer appropriate when operating in STEM mode. Instead, multiple types of detectors may be used, sometimes simultaneously. A BF detector is placed directly along the optic axis of the TEM and primarily collects transmission amplitude information along with some coherent scattering from diffraction. An annular dark field detector (ADF) is a ring detector surrounding the BF

detector. This detector omits transmitted electrons (which are collected by the BF detector), only collecting coherently scattered diffracted electrons as well as some incoherently scattered electrons due to Rutherford scattering. Lastly, a high angle annular dark field (HAADF) detector is a much larger diameter ring detector. The collection angle of this detector is large enough that coherently diffracted electrons are no longer collected. Instead, only incoherently scattered electrons from electron collisions with the atomic nuclei are collected. As the cross-section for electron scatter is proportional to the square of the element's atomic number (Z), HAADF is a highly Z-sensitive technique [80].

Of all the STEM modes discussed, HAADF imaging was used most extensively. By collecting highly scattered electrons greater than 50 mrads (2.87 °) off axis with a HAADF detector, lattice resolved imaging can be easily achieved under ideal, aberration corrected conditions. Without an aberration corrector, lattice resolved imaging may be approached under ideal conditions. Furthermore, collecting Rutherford scattered electrons yields highly Z-sensitive information. Therefore, when imaging a NW with GaAs and GaP segments, the former will appear brighter in a HAADF image due to the higher Z group V element. With a spherical aberration (C_S) corrected STEM, the accuracy of this method approaches the probe diameter. While no C_S corrected microscopes were available for this study, non-C_S corrected HAADF images in this study revealed alternating GaAs/GaP layers less than 1 nm thick. This is made possible by the probe size being less than 1nm, approximately 0.5 nm in the case of the JEOL 2010F. Indeed, the probe diameter during studies in Chapter 5 were less than the spacing between adjacent

III-V bi-layers and therefore sufficient for lattice resolved images under high magnification imaging conditions.

TEM and STEM images presented in this thesis were captured using a 200 kV JEOL 2010F in Chapter 3, and a 300 kV FEI Titan G2 60-300 in Chapter 4. The extensive TEM work performed for Chapter 5 was conducted on the JEOL 2010F. Additional CTEM characterization was performed on a 120 kV Phillips CM-12.

TEM image processing and analysis was performed through the use of three programs. First, imaging took place using Gatan Digital Micrograph software. Rudimentary analysis such as FFT power spectrum, diffraction pattern indexing, and simple length measurements were conducted with this software. More advanced features were available with a freely available software package called FIJI Is Just ImageJ (FIJI) [82]. Such functions including advanced image stitching algorithms were available for the precise merging of multiple high magnification images [83]. In addition, useful tools for image rotation, area measurements, intensity profile measurements, band pass filtering of HAADF images, and annotation were available. The final program used for the processing was MATLAB for the manual correction of image drift in high resolution HAADF scans. This program uses a simple affine transform and requires the user to manually adjust the affine matrix parameters to create an undistorted image based on prior knowledge of the sample (eg. a CTEM image). As the affine transformation will render the scale of the image incorrect, they must be manually corrected afterward using a CTEM reference. The program is included in Appendix A.

2.2.5 Analytical TEM

The high magnification nature of STEM provides a unique opportunity to perform compositional analysis on low dimensional structures. Inelastic scattering between PE and bound electrons around atomic nuclei can provide unique elemental signatures. Two primary techniques were used within this thesis: energy dispersive spectroscopy (EDS) and electron energy loss spectroscopy (EELS). The former operates on the detection of x-rays produced from electronic transitions while the latter measures energy loss of transmitted PE. Both are powerful compositional analysis tools; however, EDS is not very sensitive for low Z elements. Therefore in cases where low Z sensitivity was required, particularly if oxides were of interest, EELS was the preferred technique. EDS was sufficient for general characterization of GaAs/GaP heterostructures and measuring Ga composition in the alloy droplet.

For EDS characterization to take place, the PE must interact inelastically with an inner-shell electron. This collision excites the core electron to a less bound orbital. The inner-shell vacancy is quickly filled by an electron from an outer shell. This process will produce a characteristic X-ray or an Auger electron. In the case of the former, the X-ray had energy equal to the difference in binding energy of the electron levels. The energy of this X-ray is unique to each element and may be used to identify the composition of the specimen. By measuring the X-ray spectra produced by a material, the presence of elements and even the specimen's stoichiometry can be quantitatively determined. The detector in the JEOL JEM-2010F is a Si(Li) ultrathin polymer window (Moxtek™ AP3.3, with a 30 mm^2 active area and 0.114 sr solid angle) energy dispersive detector from

Oxford instruments. Data was collected, processed, and analyzed using INCA, which also performed active drift correction during the long acquisition periods. The detection limit for EDS measurements is approximately 1 at%.

EELS detection of elemental composition occurs through the inelastic scattering of PE with bound electrons, phonons, and plasmons. The energy of the transmitted electrons is measured with an electron spectrometer, which measures energy differences with a resolution as small as 1 eV. The typical operating range is between 100 and 1000 eV. Low Z elements give sharper excitation edges, which gives more accurate quantification.

2.2.6 TEM Sample Preparation

The small NW diameters that were a disadvantage for SEM analysis now become an advantage for TEM analysis as no mechanical polishing or ion milling is required for sample preparation. Instead, NWs were transferred to TEM grids through mechanical abrasion, ultrasonication within solution, ultramicrotomy, or focused ion beam (FIB) lamella preparation. Ultrasonication was performed by immersing a small piece of substrate with NW in methanol solution inside a small vial, which was placed in an ultrasonic bath for 1 to 2 minutes. Afterward, multiple 2 µL droplets were deposited on a carbon holey or carbon lacey coated copper TEM grid by a mechanical micropipettor (Cole-Parmer, model # EW-21600-62). This method was effective at separating NWs from the substrate by fracturing near the base but often resulted in bunching of NWs and residual hydrocarbon contamination on the TEM grid that interfered with TEM imaging. It was often necessary to clean the grid post-deposition

with an O_2 plasma on the "Carbon Film" setting (30 s, 27.5 sccm O_2, 6.4 sccm H_2 , 50 W) using a Gatan Model 950 Advanced Plasma System. In this regard, a lacey carbon grid was desirable as it was more durable to the plasma cleaning process. In contrast, a carbon holey grid could endure no more than 10 s under the same recipe.

The second method employed in this study was the use of mechanical abrasion to transfer NWs by lightly rubbing a holey carbon TEM grid against the substrate surface. This method produced a higher density of individual NWs than ultrasonication with a significantly lower amount of hydrocarbon contamination. One possible drawback of the mechanical method compared with the ultrasonication method was that abrasion fractured NWs not only at the base, but sometimes closer to the tips. This problem was mitigated by the large number of NWs on the TEM grid; however, if patterned NW arrays often had limited area then too few NWs were transferred and therefore mechanical abrasion was not an option.

The third TEM preparation method was ultramicrotomy. Small pieces of substrate were placed into embedding moulds, which were filled with hard Spurr's epoxy resin and polymerized overnight at 60 °C. Afterward, thin sections (50 to 60 nm) were cut with a diamond knife mounted in a Leica Ultracut UCT ultramicrotome. A glancing angle produced cross-sectional samples useful for characterizing compositional changes in the radial direction (ie. core-shell structures). A cutting angle perpendicular to the substrate surface was useful for the examination of nanowires still attached to the substrate, bases included; however, the substrate was usually heavily fractured.

The final TEM preparation method was FIB milling, where a section of the substrate is milled with a Ga ion beam, thinned for electron transparency, transferred, and attached to a TEM grid. This technique provides information regarding the spatial location of the NWs, which was found to be most beneficial in Chapter 4. The disadvantage of FIB preparation with NWs was that the NWs were often covered in a thick carbon coating layer as part of the milling procedure, which negatively impacted image quality and often caused the NWs to bend.

2.3 Electron Beam Lithography

The motivations and advantages of using pre-patterned Au seed arrays were elucidated in section 1.2.5. A method of depositing Au VLS seeds with monodisperse diameters and a controlled nearest neighbor distance, referred to as pitch hereafter, is necessary in order to form uniform NW arrays. Several techniques have been demonstrated for the controlled deposition of Au nanoparticles. These include electron beam lithography (EBL) [51,84], nano-imprint lithography [85,86], block co-polymers, porous anodic alumina masks [87], and poly-styrene spheres [88]. While these methods ubiquitously employ electron beam evaporation for the deposition of Au, alternative methods such as galvanic reaction have also been demonstrated [89]. Of these methods, EBL is attractive as it is an extremely versatile research tool that allows the engineering and flexible design of particle diameters and pitches. While this technique is useful for proof-of-concept studies, EBL is a very slow process due to its serial nature; however, the more economical patterning of full wafers remains possible through the use of massively parallel processing techniques such as nano-imprint lithography.

2.3.1 Fundamentals

EBL is a marriage of electron microscopy and photolithography techniques. The formation and focusing of an electron beam that can be precisely raster scanned across a flat surface is heavily influenced by the scanning electron microscope, which was introduced in section 2.2.2. The application of this technology largely differs from image formation, more closely mimicking photolithography methods of selectively exposing areas for strategic additive or subtractive modification.

The EBL system itself appears much like a SEM due to their shared heritage. Many of the performance characteristics that are attractive for SEM are also desired for EBL. Namely, the smallest electron probe size is usually the most desirable; however, while SEM systems often seek to accomplish this with low beam current, EBL systems must balance the trade-off between high current and probe size. This difference speaks to the vastly different applications each system is designed for.

The ultimate objective of an EBL system is to modify the properties of a thin resist layer applied overtop a substrate. As with photolithography, this resist may be of the positive or negative type. Following exposure to high energy electrons, the exposed resist will become selectively soluble (positive) or insoluble (negative) when soaked in a developer solvent. The action of selectively removing regions of the resist allows for the further modification of the substrate through additive means, ie. thin film deposition, or through subtractive means, ie. etching. The pattern is defined by electron exposure, termed dose in units of charge per area (typically $\mu C/cm^2$). The resolution of the EBL pattern will be defined by the minimum area of interaction possible and the time to

write an area with a certain dose value will be a function of the beam current. Therefore, the EBL and SEM systems will differ with respect to their accelerating voltage and beam current.

The probe size of an EBL system will be limited by the same factors that were discussed in section 2.2.2. A typical SEM or EBL probe size on the scale of a nanometer is impressively small when compared with the dimensions of typical VLS seed particles (10 - 100 nm); however, the ultimate EBL resolution is not only dictated by the electron beam probe size, but also by secondary and backscattered electrons that are created as the primary electrons (PE) interact with the resist and the underlying substrate. It is the management of the secondary and backscattered electrons that separate the design of EBL and SEM systems. Namely, where SEM systems seek to promote the extraction of secondary or backscattered electrons, EBL systems are designed to eliminate or spread them across a very broad area. This is accomplished by using large accelerating voltages, such as 100 kV in dedicated EBL systems. A typical SEM will operate at accelerating voltages up to 30 kV and therefore will have a substantially more concentrated secondary and backscattered electron dose.

As typical EBL systems only have a single electron beam, writing is serial and completion time scales linearly with current; however, increasing the beam current will lead to a corresponding increase in the minimum probe size as the electrons repel one another. Further limitations on the translation frequency of the PE beam exist, limiting the use of higher beam currents to speed the writing of resists that only require a low dose. For example, industrial grade EBL equipment are limited to a maximum rate of

50MHz for beam blanking and deflection, which results in a minimum beam dwell time of 20 ns. Beam blanking is a necessary function of an EBL system whereby the PE beam is deflected such that it does not reach the substrate. Blanking is necessary to prevent unintentional exposure when translating the beam between areas being intentionally exposed. When writing patterns for VLS seeds, the frequency can be a limiting factor for patterns that require low doses. The EBPG 5000+ at the University of Toronto could write typical VLS seed patterns with currents between 15 to 30 nA and become frequency limited for typical dose levels. Comparatively, SEM systems with integrated EBL functionality are limited to currents on the order of 100 pA.

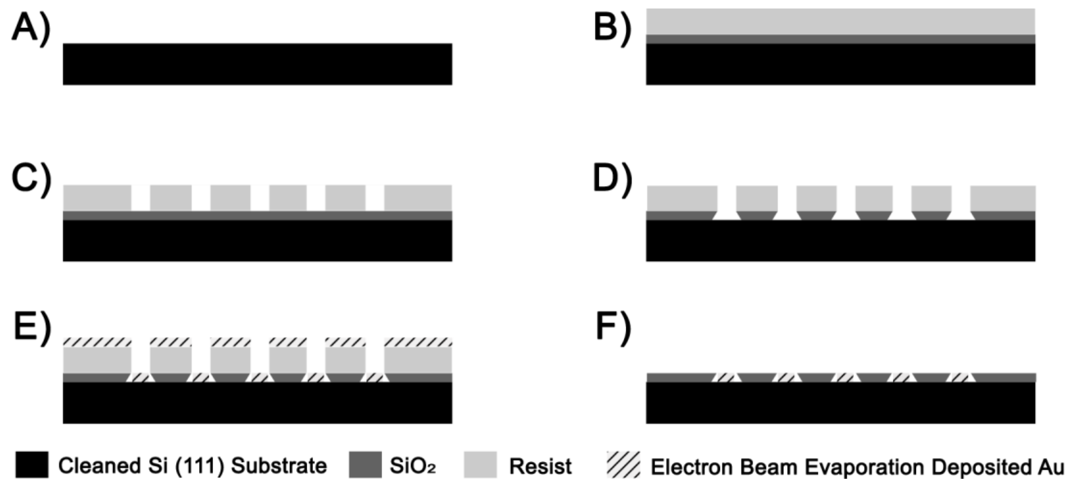

Figure 2.2: Deposition of Au dots into SiO_2 wells. (a) A clean Si (111) wafer. (b) An SiO_2 layer may optionally be deposited by CVD or grown by thermal oxidation. Afterward a resist layer is applied through spin deposition. (c) The pattern is written by EBL and immersed in a solvent solution that dissolves the exposed areas only. (d) The SiO_2 layer is selectively removed by an etchant. (e) The surface is metalized by electron beam evaporated Au. (f) The resist and overlying Au film are lifted-off by ultrasonication in a solvent. The drawing is not to scale.

The process for writing and depositing VLS seeds is depicted in Figure 2.2. A detailed procedure is given in Appendix B. The process begins with cleaning a Si(111) wafer. The intensity of this cleaning step can vary between 1 min ultrasonication in acetone and iso-propanol (IPA) or full "RCA clean" consisting of steps to remove organic and metallic contaminants as well as any resulting oxide films. A silicon oxide layer may then be deposited by CVD or grown thermally if desired. Next, a positive EBL resist is spun onto the substrate and soft baked to evaporate any solvent left in the resist film. After the EBL pattern is written, the substrate is soaked in a solvent called the developer, which preferentially dissolves the exposed regions. At this stage, it is a good practice to perform an O_2 plasma ash such that residual resist in the developed areas is appropriately removed. Immediately prior to depositing the Au film the silicon oxide, whether intentional or due to ambient oxygen exposure, must be removed by an HF etch. This etch will leave the Si(111) surface passivated with hydrogen bonds and without an oxide for a brief period of time afterward, allowing enough time to load the wafer into a load lock to be placed under vacuum before oxide formation begins. The subsequent deposition of an Au film will cover the resist, and the exposed regions of the Si(111) surface. Afterward, the resist layer is removed through ultrasonication in a solvent, removing the undesired Au film with it and leaving a patterned array of Au discs behind. Additional organic removal procedures are advisable, such as aggressive rounds of O_2 plasma ashing and even brief sulphuric acid etches.

During the development step, the complete thickness of the film will be removed so long as an adequate dose was delivered to the area. This is called a clearing

dose. The clearing dose is empirically found by performing a dose test and will be depend on the resist type and thickness, accelerating voltage and beam current, as well as the proximity and density of neighboring writes. While standard recipes may exist, every pattern can be optimized for minimum write times and optimal pattern integrity through the use of dose tests. These tests generally consist of writing the same pattern repeatedly at incrementally different doses, processing the patterns, and then evaluating what the clearing dose was. In the case of writing patterned arrays for VLS seeds, a small area on every wafer should be dedicated to writing a dose test in every run. This adds seconds to the total write time and can help inexpensively diagnose problems when EBL results are not as expected.

The method to form VLS seed holes in the resist differs from standard EBL practices. As VLS particles are usually less than 100 nm in diameter, it is sufficient to write such a feature with a single exposure, referred to as spot lithography. This is accomplished by allowing the beam to dwell at that position for an extended period of time in comparison with the dwell time when writing 2D shapes, where a standard clearing dose is approximately 250 $\mu C/cm^2$. In comparison, the minimum clearing dose for a hexagonal spot lithography array with a 1 µm pitch was determined via dose test to be approximately 7000 $\mu C/cm^2$, or 0.9 pC/seed. Such a dose yielded a hole with a diameter of 40nm. The size of the VLS droplet during growth will not only depend on this diameter, but also on how thick of a Au layer was deposited, the growth conditions, and droplet composition when NW growth was initiated.

2.3.2 Summary of EBL Patterned Nanowire Growth Results

Patterned growth was carried out on Si(111) substrates exclusively. Early NW growth experiments were carried out on GaAs(111)B wafers and Au VLS seeds were formed via the thin film annealing process; however, GaAs wafers were unsuitable for patterned growth as Au droplets were highly mobile on the surface during the thermal ramp to MBE growth conditions. This was reported by Ghosh et al. where it was observed that Au droplets created etch pits along the [011] directions on the substrate surface of the GaAs(100) surface [90]. Annealing experiments of patterned Au droplets on Si(111) under MBE conditions have demonstrated that droplets are stationary prior to the introduction of group III and V flux, see Figure 2.3.

Early results for patterned arrays of Au-assisted VLS NWs on Si(111) were very promising. While initial attempts gave poor yields of vertical NWs, as shown in Figure 2.4(a), the mechanism responsible for this behavior was discovered and eliminated. This investigation is described in detail in Chapter 4. Subsequent growth gave yields of vertical GaP NWs greater than 90% with a growth rate of 0.5 μm/h, V/III ratio of 2.3, and a temperature of ~600°C. This growth was carried out on an indium mounted wafer, a process where a small substrate was affixed to another using the capillary force of liquid indium. This was necessary so that small, Si pieces that did not fit pre-existing substrate trays could be loaded into the MBE. As a result of this process, there was a substantial amount of liquid indium on the substrate. Furthermore, the pyrometer method of measurement was rendered inaccurate by the presence of liquid indium, so the exact temperature of this successful experiment is not known.

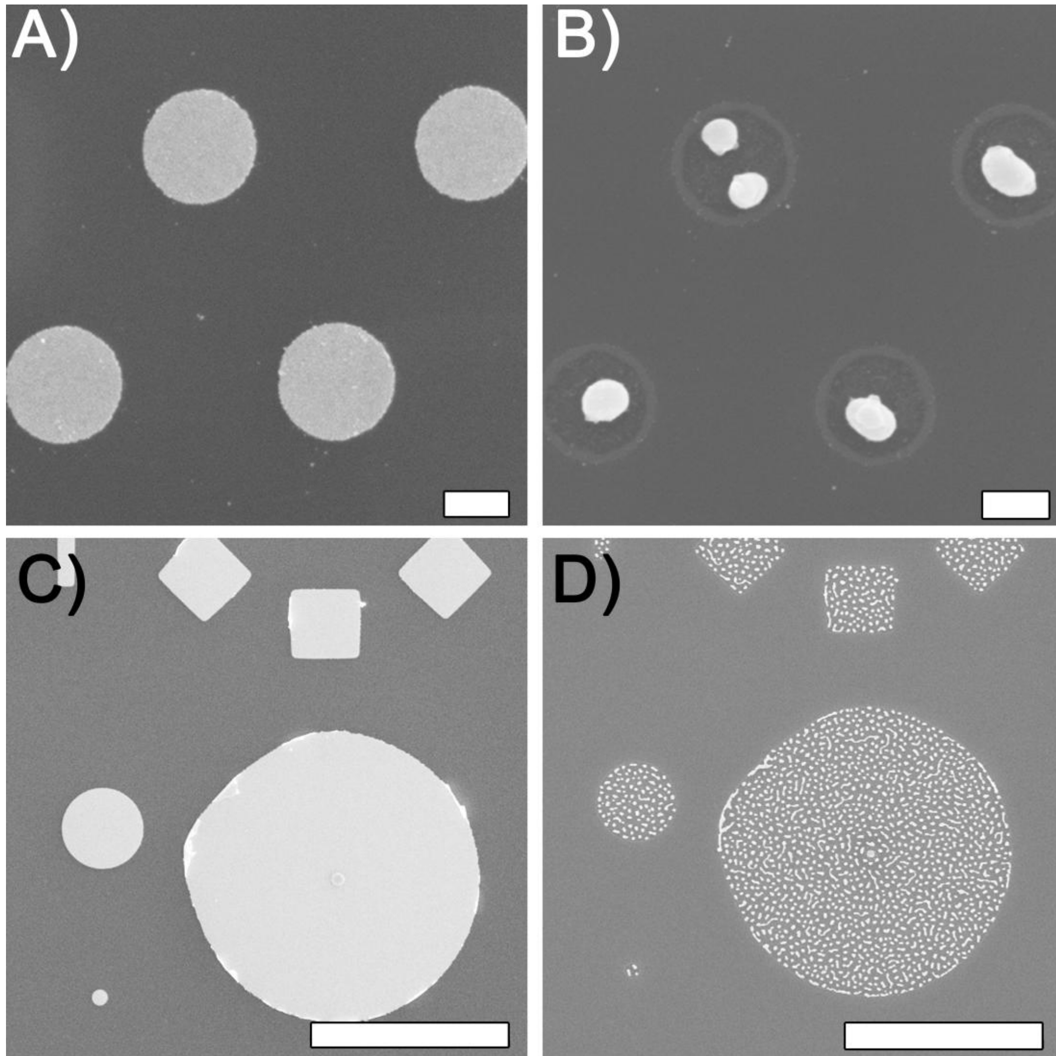

Figure 2.3: An annealing experiment performed with EBL written patterns. Annealing was conducted at 550°C. (a,c) As-deposited. (b,d) post anneal. (a,b) The Au "disks" alloyed with the Si substrate and became liquid forming either one or two droplets. Scale bar indicates 250 nm. (c,d) The larger shapes could not form a single droplet and instead formed many droplets, but retained the original shape. Scale bar indicates 10 µm.

Representative SEM images of patterned NW growth are given in Figure 2.4(b). The smallest doses led to the highest yield of single, vertical NWs and very few unintended NWs; however, even the unintended NWs had a vertical growth orientation.

The largest doses resulted in droplets that broke into many small, yet still vertical NWs surrounding a central, large diameter NW. The GaP thin film appeared finely grained and very rough. Subsequent attempts were not able to reproduce these results after duplicating the deposition conditions on full Si(111) substrates without indium mounting. Re-introducing indium into the system was not explored as a change in the NW composition was not desirable; however, the presence of indium may have been a key component in attaining the high yield result. Trace levels of indium have been reported to stabilize the Au droplet in MOCVD experiments [91].

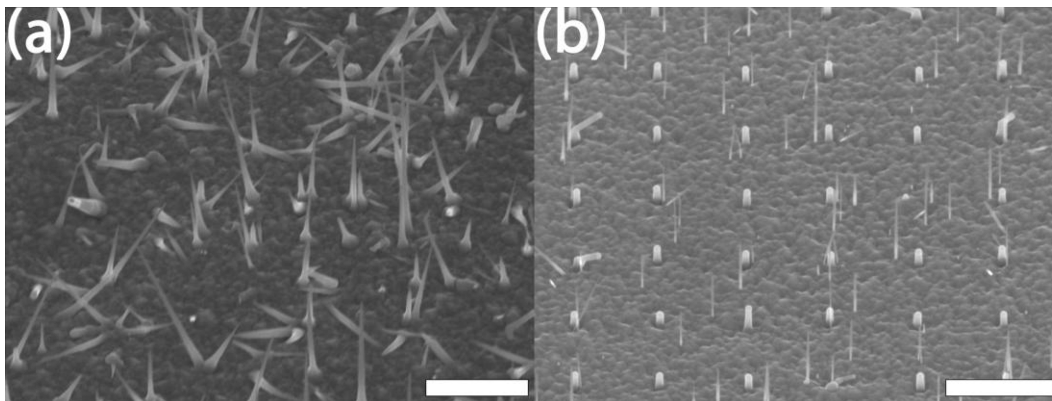

Figure 2.4: (a) Preliminary EBL results. NWs appear randomly oriented. Intentional, vertical NW yield was near 0%. (b) NW array with greater than 90% yield along with some unintentional, thin NWs. Scale bars indicate 1µm.

After a broad parameter search to obtain high yield of GaAs NW growth on Si(111), growth conditions that gave vertical NW yields near 50% were determined. These included extensive substrate preparation, as described in detail in Appendix B. GaAs growth conditions included a 5 s Ga pre-deposition at 600°C followed by initiating growth at 0.25µm/h with a V/III flux of 6. A representative image of the resulting NW

array is shown in. The yield dependence on pattern pitch is very strong, with the 1 and 2 µm pitch patterns producing the highest yields of intended NWs while the 250 and 500 nm pitch patterns were overwhelmed by a substantial number of unintended, long NWs. Significant detractors from attaining a better yield appear to be a combination of single VLS seeds splitting into multiple droplets with smaller diameters, the formation of kinked NWs, and the growth in equivalent [111] orientations [92].

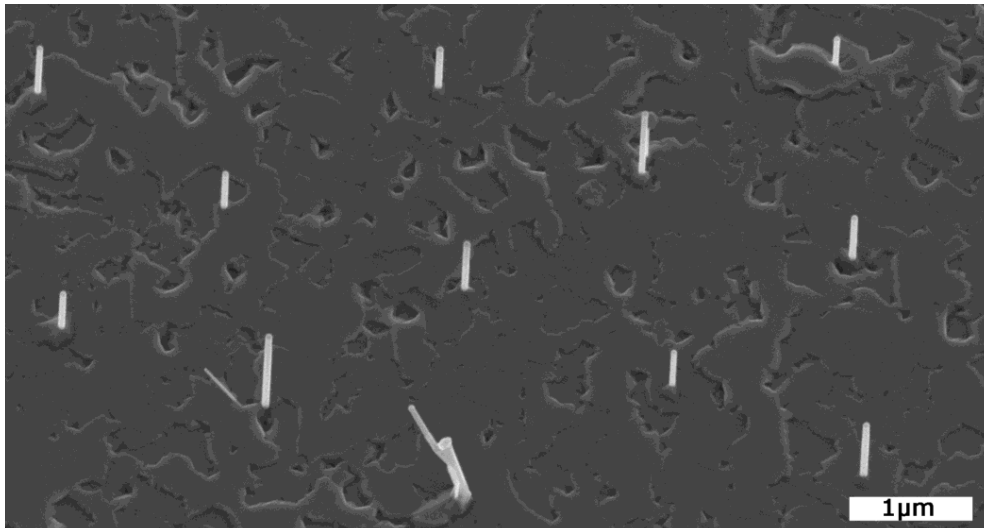

Figure 2.5: GaAs patterned NW array with hexagonal symmetry and a 2 µm pitch.

A major factor inhibiting a high yield of vertical GaAs NWs on Si(111) has been theorized to be the lower interfacial energy between the droplet and the Si(111) substrate versus GaAs(111)B. It has been shown that droplets will remain in contact with the substrate so long as the Si(111) surface is exposed [93]. Over time a GaAs film will cover the substrate and contact between the droplet and the Si(111) surface is no longer possible. In other words, [111] VLS growth perpendicular to the substrate is energetically unfavorable during the early moments of GaAs growth on Si(111)

substrates. This leads to a number of non-ideal behaviors, principally, the VLS droplet does not rise above the rough (111) GaAs film, but instead remains in contact until the film and the droplet collide. The resulting collision may promote non-ideal behaviors such as nucleating on a facet of the rough GaAs thin film instead of the Si(111) substrate or the burying or partial burying of the droplet.

Changes in MBE growth parameters and the introduction of indium in early experiments have a prominent effect on the composition and the surface energy of the droplet as well as an effect on the GaAs(111) film itself. It is proposed that the success of the early patterning results was due to a decrease in droplet surface energy and prompt [111] growth upon the impingement of Ga and P adatoms. In general, high patterned yields of Au-assisted GaAs NWs on Si require that it be energetically favorable for a droplet to nucleate a (111) GaAs layer beneath the droplet and break contact with the surface. A lowering of the surface energy of the droplet can be affected by supersaturating the droplet with Ga adatoms before introducing As or P. Lastly, the role of Si in the droplet is unclear at this time, although a Au-Si alloy certainly develops during the ramp to MBE growth temperatures [94]. No Si has yet been observed in the droplet when examined by EDS during TEM analysis.

3 Axial GaAs/GaP Heterostructure Nanowires

This Chapter contains published work from "Polytype formation in GaAs/GaP axial NW heterostructures" by J.P. Boulanger and R.R. LaPierre, published in 2011 [51]. The structures grown in this work were designed to provide more information regarding the growth rates for GaAs and GaP under identical deposition conditions. Instead of multiple separate growths, many GaAs and GaP segments could be compared simultaneously; however, these samples became ultimately much more interesting with regards to their crystallographic properties. The observation of a unique polytype was the sign that interesting growth physics were occurring after a GaAs/GaP hetero-interface. Subsequent research efforts to understand and identify transient growth phenomenon took shape following this discovery.

3.1 Polytype formation in GaAs/GaP axial nanowire heterostructures

3.1.1 Introduction

One of the key challenges in the growth of nanowires (NWs) is the control of NW crystal structure. III-V NWs are frequently observed to have the wurtzite (WZ) crystal structure while the stable bulk or thin film crystal structure is zincblende (ZB). Stacking faults, whereby the crystal structure alternates between WZ and ZB along the NW axis, or ZB twinning, is also frequently observed. The presence of WZ structure in NWs has been explained by a nucleation-based model [38]. Due to different interface energies between WZ and ZB, nucleation of WZ is favored at the VLS triple-phase line at

high liquid supersaturation. On this basis, the influence of NW radius and growth conditions (e.g., temperature, V/III flux ratio, growth rate) on NW crystal structure has been modeled [40,95,96]. These issues are well described in a number of recent review articles [10,31]. The present paper contributes to the earlier experimental work by reporting polytype phases observed in III-V heterostructured GaAs/GaP NWs grown by MBE.

3.1.2 Experimental Details

Experiments were conducted on GaAs (111)B Epi-ready substrates. A sacrificial oxide was formed by a 20 minute UV ozone treatment to remove residual hydrocarbon contamination. The oxide was later removed by a 30 second 10% buffered HF etch. The substrate was then immediately loaded into a metallization chamber where a 1 nm thick Au film was deposited at room temperature.

Upon loading the substrate into a gas source MBE system, the substrate was degassed for 15 minutes at 300 °C under UHV conditions. The substrate was then heated to 580 °C under an As_2 overpressure followed by a 10 minute inductively coupled H_2 plasma (ICP) cleaning to remove residual surface oxides and form Au-Ga alloy droplets [97]. The substrate was rotated with a period of 4.5 seconds. NW and 2D film growth was initiated upon the opening of the Ga effusion cell shutter. In the gas source MBE system, Ga was supplied from an elemental effusion cell while As_2 and P_2 were supplied from high temperature (950 °C) cracking of AsH_3 and PH_3, respectively.

Two experiments involving GaAs/GaP axial heterostructured NWs were conducted and are represented in Figure 3.1. Samples A-1 and A-2 differed only by the base GaAs segment, which was grown with a group III impingement rate (2-D equivalent growth rate) of 0.5 and 1.0 μm/h, respectively. Besides the difference in growth rate of the base GaAs segment between the two samples, all other segments of both samples were grown at 0.5 μm/hr. Both samples were grown with a V/III flux ratio of 2.3. Hence, sample A-2 that was grown at the higher group III impingement rate compared to sample A-1 was also grown with a corresponding increase in group V flux to maintain a constant V/III flux ratio of 2.3. All other growth parameters were identical between the two samples.

Pure axial NW growth can be achieved by using MBE growth conditions that decrease the probability of island nucleation on the NW sidewalls. Optimal conditions for promoting pure axial NW growth were previously found to be a combination of high temperature (~ 580°C), low Ga flux (a 2D equivalent growth rate of 0.5 μm/h), and an intermediate V/III flux ratio of about 2.3 [3]. These MBE parameters give adatoms the longest diffusion lengths before incorporating and therefore promote pure-axial growth for greater NW lengths. Consequently, these conditions were used in the present study.

Axial NW heterostructures were formed by the following process (see inset of Figure 3.1). In the case of switching from GaAs to GaP growth, the GaAs segment was terminated by closing the Ga effusion cell shutter. Immediately afterward, the group V dimers were switched by simultaneously providing the full P_2 flow rate and stopping the flow of the As_2. The time delay between terminating the As_2 flow and opening the Ga

shutter was 20 seconds. When switching from GaP to GaAs, the same procedure was followed, but with the group V dimers reversed. After the desired structure was formed (as shown in Figure 3.1), NW growth was terminated by shuttering the Ga beam and cooling under P_2 overpressure.

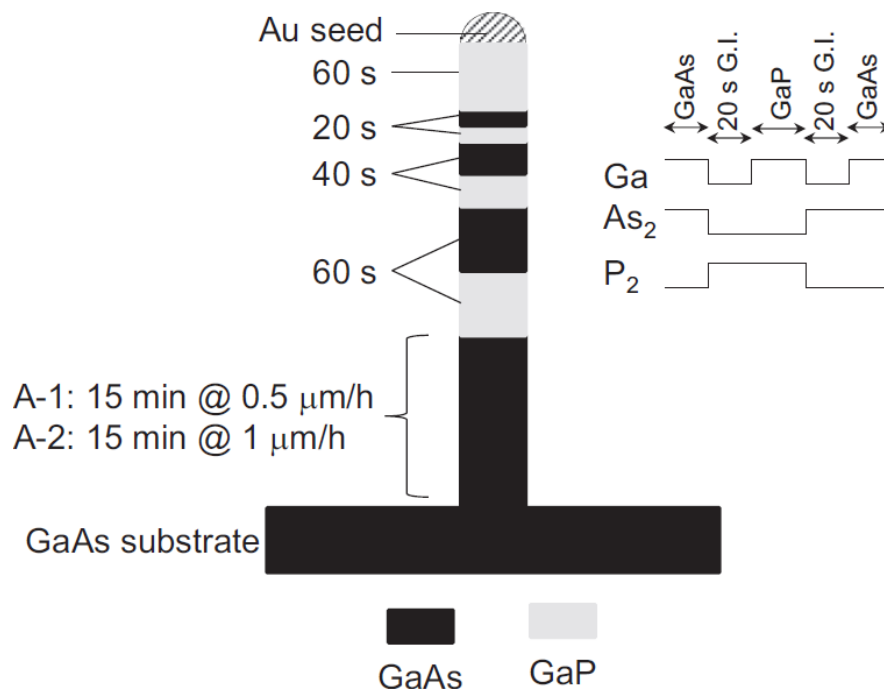

Figure 3.1: Summary of MBE growth parameters for samples A-1 and A-2. Inset shows the gas switching sequence at a GaAs/GaP/GaAs segment (G.I. is growth interruption).

Following growth, NWs were characterized by both scanning electron microscopy (SEM) and transmission electron microscopy (TEM). Cross-sectional SEM imaging was performed in a JEOL JSM-7000 instrument. NWs were removed from their substrate for TEM analysis either by ultrasonication, mechanical abrasion or ultramicrotomy. Conventional TEM was performed on a Philips CM-12. High resolution

TEM (HR-TEM), high angle annular dark field (HAADF) imaging, and energy dispersive x-ray spectroscopy (EDS) were performed on a JEOL 2010F at 200 kV and an FEI Titan G2 60-300 at 300 kV. Each NW was imaged on the <-2110> zone axis to reveal crystal phase changes and measure the abruptness of hetero-interfaces. Extended zincblende (ZB) and wurtzite (WZ) segments in NWs are easily distinguished via HR-TEM when viewing on the <-2110> zone axis; however, short segments of 4H polytypes can be difficult to differentiate from ordinary stacking faults. In the present study, the criteria used for identification of the 4H phase was the observation of at least four consecutive 4H unit cells in HR-TEM or HAADF which provided sufficient length to perform a power spectrum for identification of the 1/4 <0002> reflection. HR-TEM and HAADF images in this study were filtered for clearer phase identification. In the case of HR-TEM images, filtering was performed in Digital Micrograph using the freely available "HRTEM Filter" script. This script rotationally averages the image power spectrum to subtract amorphous components and is based on the work of R. Kilaas [98]. HAADF images were post-processed by bandpass filtering of the power spectrum (3 - 40 pixels) using ImageJ freeware.

3.1.3 Results and Discussion

Cross-sectional SEM of samples A-1 and A-2 in Figure 3.2(a) and (b), respectively, showed significant differences in NW morphology. Au particles used for seeding the NW growth were visible at the top of the NWs. The average and standard deviation of the NW diameter measured directly beneath the Au particle, as obtained from the cross-sectional SEM images, was 63 ± 37 nm for sample A-1. The average

height of the A-1 NWs was 350 ± 83 nm. On the other hand, sample A-2 NWs exhibited a broader height and diameter distribution compared to sample A-1 as seen by comparing the SEM images in Figure 3.2(a) and (b). A-2 NWs with diameter less than 35 nm had heights ranging from 1 μm to 2 μm. Accurate measurement of the diameters and heights of these long (> 1 μm) and thin (<35 nm diameter) NWs by SEM was complicated by the bending and vibration of NWs during observation, presumably due to charging effects. Excluding these long and thin NWs, the average diameter and height of the sample A-2 NWs was 67 ± 28 nm and 570 ± 190 nm.

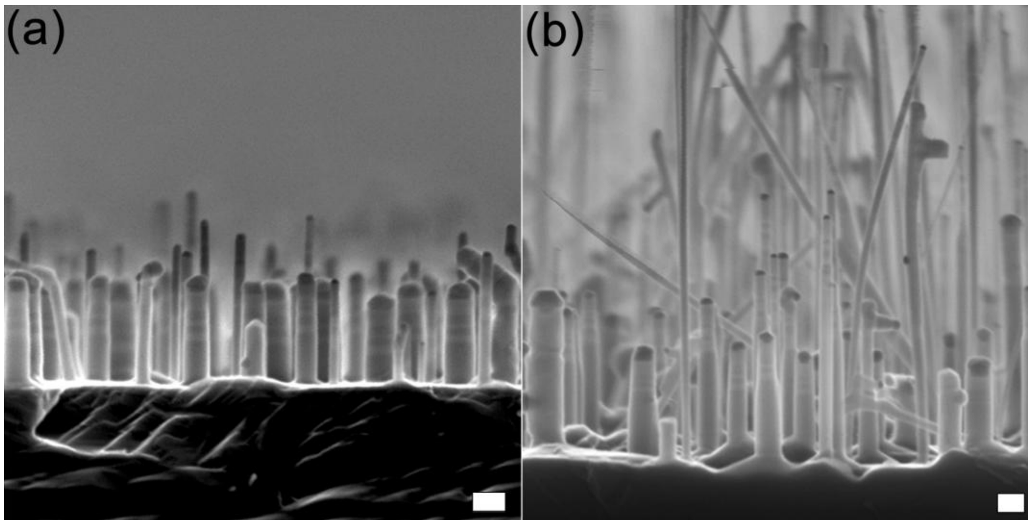

Figure 3.2: Cross-sectional SEM images of sample (a) A-1 and (b) A-2. The scale bar indicates 100 nm.

A representative HAADF image of an A-2 NW is shown in Figure 3.3 with superimposed EDS compositional profiles along the axis of the NW. The abrupt change in As and P content measured by the $K\alpha_1$ x-ray counts, indicates abrupt GaAs/GaP interfaces and no significant intermixing of Group V elements. As expected, the segment

lengths decreased with decreasing growth duration (60, 40, and 20 s) in the direction of growth. Similar results were obtained for the sample A-1 NWs.

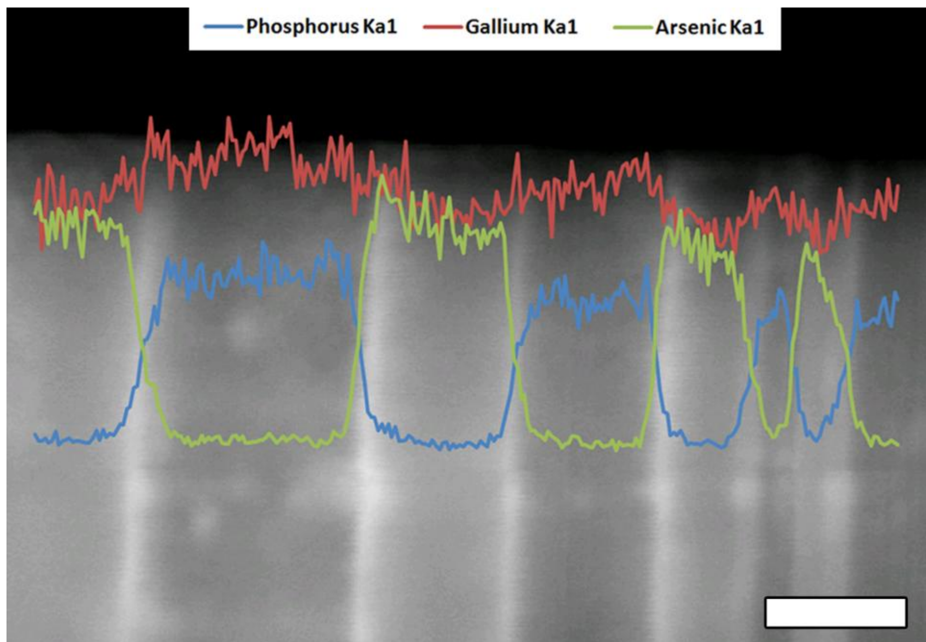

Figure 3.3: HAADF images of an A-2 NW with superimposed EDS linescan profiles (P: blue, Ga: red, As: green). Growth direction is from left to right. The lighter contrast segments are GaAs, while the darker are GaP. The segments from left to right are: GaAs base, 60 s GaP, 60 s GaAs, 40 s GaP, 40 s GaAs, 20 s GaP, 20 s GaAs, final 60 s GaP. Scale bar indicates 50 nm.

The segment length of each GaAs and GaP segment in the A-1 and A-2 NWs were obtained for a variety of NW diameters by direct measurement from HAADF images such as that in Figure 3.3. The growth rate was then determined as the segment length divided by its growth duration as presented in Figure 3.4. The symbol type in Figure 3.4 is indicative of the crystal phase of each NW segment as discussed below. The growth rate of all segments decreased with increasing diameter, which is commonly observed for MBE grown NWs. The latter observation is attributed to the diffusion of

adatoms from the NW sidewalls resulting in a NW length that is inversely proportional to radius, owing to the ratio between the NW sidewall collection area and the growth area beneath the Au droplet [30,31].

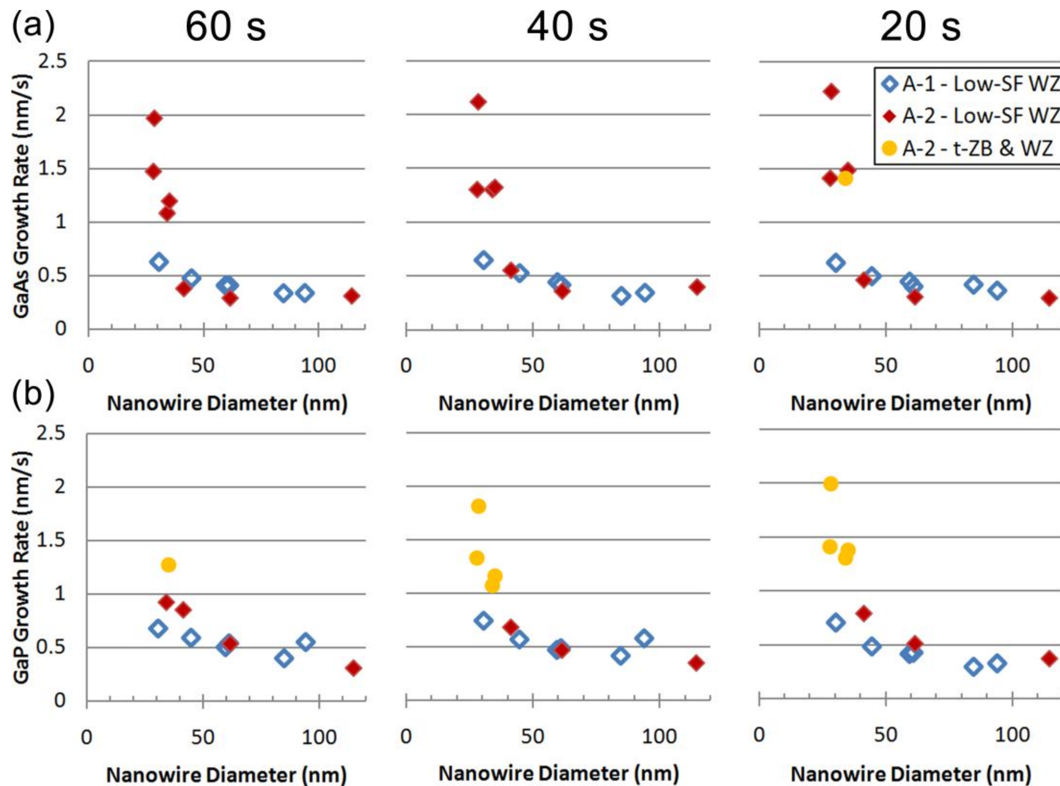

Figure 3.4: Sample A-1 and A-2 growth rates versus diameter for (a) GaAs and (b) GaP segments. The plots are placed in order of the segment growth durations: 60 s, 40 s, and 20 s from left to right. Open symbols indicate A-1 NWs. Solid symbols indicate A-2 NWs. Circles: twinned ZB and WZ; diamonds: WZ with a low density of stacking faults.

As observed in the SEM images of Figure 3.2, and confirmed in Figure 3.4, sample A-2 exhibited smaller diameters and thus taller NWs compared to sample A-1. Due to the identical substrate preparation methods used for samples A-1 and A-2, the difference in NW heights and diameters between these two samples can only be

ascribed to the higher group III (and V) flux for the base GaAs segment in Sample A-2 compared to A-1. We postulate that the differences between A-1 and A-2 NWs can be explained by the diameter dependence of growth rate [99,100]:

$$R = \frac{P - P_{\infty}\exp\left(\frac{2\sigma\Omega}{r_w k_B T}\right)}{\sqrt{2\pi m k_B T}} \quad (3.1)$$

where R is the impingement rate of adatoms (Ga), k_B is Boltzmann's constant, T is the growth temperature, P is the reactant pressure surrounding the NW, r_w is the Au alloy particle radius (~NW radius), σ is the vapor-liquid surface energy of the particle, Ω is the atomic volume of the reactant element in the Au particle, m is the mass of the reactant species, and P_{∞} is the reactant pressure in a particle of infinite radius of curvature. The second term in the numerator of Equation (3.1) describes the well-known Gibbs-Thomson effect which can reduce the growth rate of the smallest Au alloy particles (~20 nm in the present study) [31,40,95,96]. The Gibbs-Thomson effect can be overcome by increasing the alloy droplet supersaturation (i.e., by increasing the group III and V flux to the Au particle). Thus, the increased group III and V flux within the first 15 min of growth in the A-2 NWs contributed to a taller base GaAs segment in the smallest diameter droplets as compared to those in sample A-1. A similar effect was previously observed in InGaP NWs [101]. At small diameters (~20 nm), the growth rate for each of the segments (60 s, 40 s, 0 s) at the top of the NWs in Figure 3.4(a) and (b) was greater for the A-2 sample (filled symbols) compared to A-1 (open symbols). Evidently, the differences in height of the earlier GaAs base segment (as discussed above) influenced the growth rate in the later, identically grown segments at the top of the NW. The taller

and thinner NWs resulting in the A-2 sample compared to A-1 presumably presented a larger sidewall surface area for adatom collection from the base GaAs segment and thus a higher growth rate for the short GaAs and GaP segments at the top of the NWs (20 s, 40 s, and 60 s segments). These results indicate the importance of the sidewall collection area in defining the growth rate of the NW segments. As will be discussed below, these growth rate differences also influence the NW crystal structure.

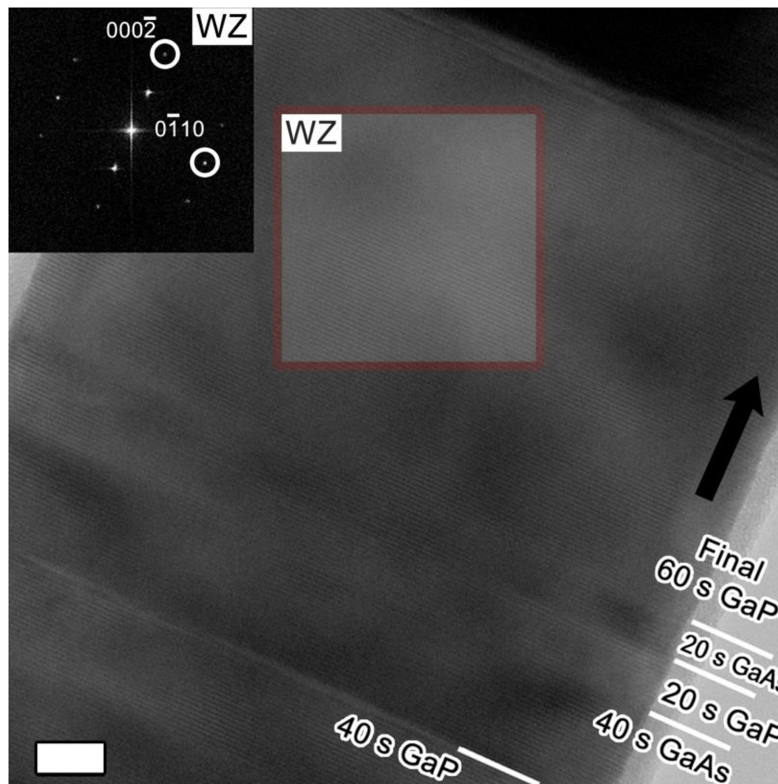

Figure 3.5: Bright Field HR-TEM image of sample A-1, 115 nm diameter. (a) WZ with low stacking fault density (A-2 NW, 115 nm diameter). Scale bar indicates 10 nm. Insets contain power a spectrum from indicated area and the arrow points in the direction of growth. Hetero-interfaces were determined by HAADF images (not shown).

TEM analysis revealed significant structural differences between the NWs in samples A-1 and A-2. Figure 3.5 and 3.6 show representative HR-TEM images of the crystal structures found in A-1 and A-2 NWs, respectively. The location of each hetero-interface is indicated based on the corresponding HAADF images (not shown). Within the consecutively grown 60 s, 40 s, and 20 s GaAs and GaP segments, two phases were present as represented in Figure 3.4: twinned ZB (t-ZB, filled circles) and WZ with low stacking fault density (diamonds). Regardless of NW diameter, the GaAs segments in both A-1 and A-2 NWs had the wurtzite (WZ) phase with a low density of stacking faults (open or solid diamonds in Figure 3.4(a). A representative HR-TEM image of the latter case is presented in Figure 3.5 along with a power spectrum as inset. Similar to the GaAs segments, the GaP segments for both A-1 and A-2 NWs exhibited a similar WZ phase for large diameters (>35 nm). On the other hand, for smaller diameters, the A-1 and A-2 NWs exhibited different polytypes in the GaP segments. In A-1 NWs, WZ with low stacking fault densities (open diamonds) remained as the principle polytype for diameters below 35 nm. Conversely, for A-2 NWs in the same diameter range, WZ was observed for only a short segment (~20 nm) following the GaAs/GaP hetero-interface. Thereafter, ZB with a high density of twinning faults (solid circles), with only 2 – 10 nm between faults, was the dominant phase until the following hetero-interface. A representative HR-TEM image of this polytypic behavior is presented in Figure 3.6 along with a power spectrum for the indicated regions. In summary, all segments exhibited the WZ phase with low stacking fault density, except the GaP segments in sample A-2 at small diameter (large growth rate) where the twinned ZB phase was observed. As will be

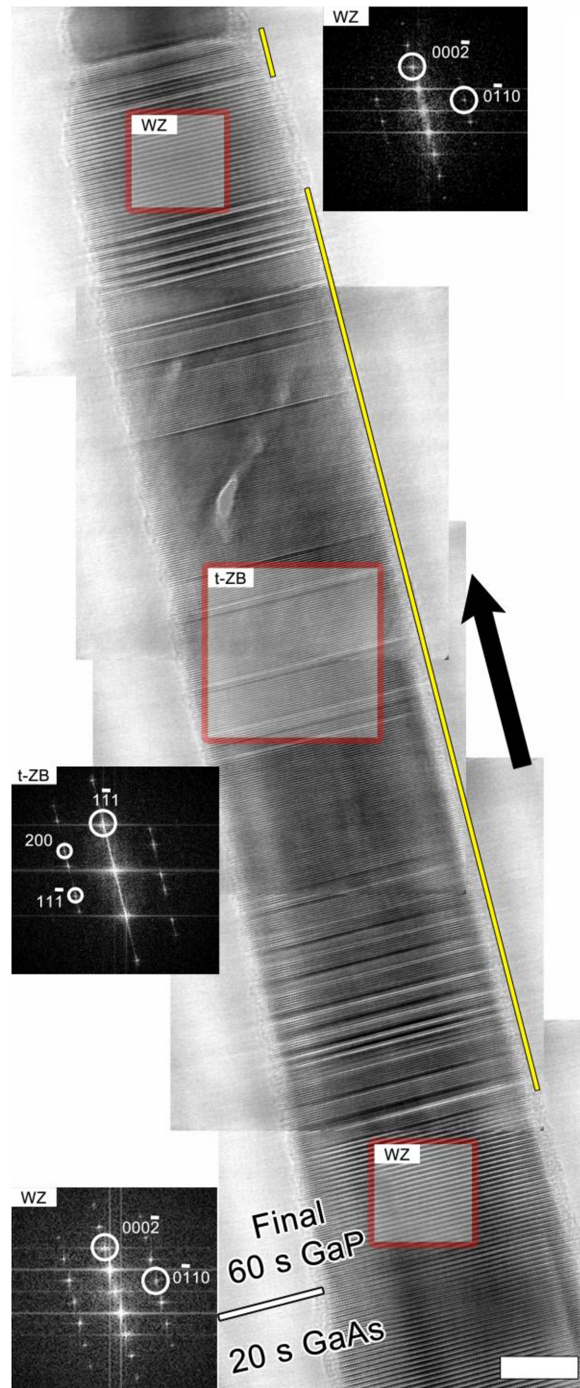

Figure 3.6: Bright Field HR-TEM image showing the polytypes observed in this sample A-2 NW, 28 nm diameter. Twinned ZB (t-ZB) is indicated by the long yellow line and middle power spectrum. The short yellow line at the NW tip indicates the ZB cooling neck. Scale bar indicates 10 nm. Insets contain power spectrums from indicated areas and the arrow points in the direction of growth. Hetero-interfaces were determined by HAADF images (not shown).

argued below, the results summarized in Figure 3.4 suggest a dependence of crystal structure on growth rate or, equivalently, the supersaturation of the alloy droplet.

In addition to the aforementioned polytypes, all of the A-1 and A-2 NWs exhibited a short segment (< 10 nm) of ZB structure at the NW tip directly beneath the Au particle, which was observed to coincide with a slight tapering of the NW diameter (See Figure 3.6). This is consistent with the previously reported "cooling neck" phenomenon [38]. Preceding the ZB cooling neck, we also observed a short segment of WZ in the final GaP segment as shown, for example, at the top of the NW in Figure 3.6.

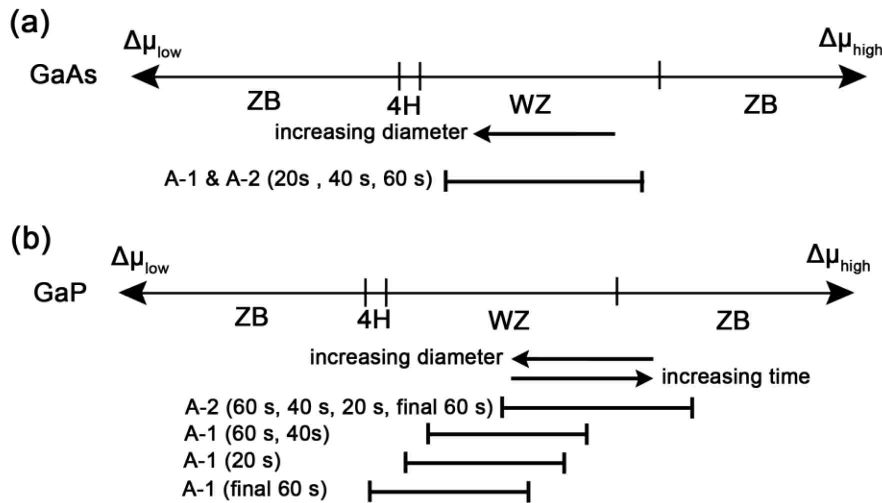

Figure 3.7: Schematic of different polytypes versus supersaturation (chemical potential difference $\Delta\mu$ between the Au-III-V droplet and the underlying solid) observed in the 60, 40 and 20 s segments of (a) GaAs and (b) GaP. The arrows indicate the observed range of phases in each segment and the trend with diameter or growth duration (increasing time).

To explain the appearance of the different polytypes in samples A-1 and A-2, we suggest that the ZB, 4H, WZ and twinned ZB polytypes occur in order of increasing Au

droplet supersaturation as indicated in Figure 3.7 in a manner similar to Dheeraj et. al. [13]. The results summarized in Figure 3.7 are consistent with other reported results. Firstly, it has been argued that the existence of ZB at the base and tip of MBE and CBE grown NWs demonstrates that ZB forms at lower supersaturation levels [28], consistent with the observation of ZB structure in the cooling neck at the tip of all A-1 and A-2 NWs. Secondly, MBE growth of GaAs/GaAsSb axial heterostructured NWs has demonstrated the progression of ZB to 4H to WZ in GaAs following a GaAsSb/GaAs hetero-interface [13]. This same order has been observed in InAs and InSb NWs grown by MOVPE [65]. Thirdly, our past studies have indicated that highly faulted WZ occurs at high supersaturation levels in GaP and GaAs [45,52]. Fourthly, Ren et al. demonstrated experimentally and theoretically that GaAs NWs will form ZB at very high supersaturation levels [102]. Finally, phase transitions in GaAs are expected to occur at higher supersaturations than GaP. This is in part due to the lower stacking fault energy of GaP as well as the increased sidewall energy [31,102,103]. The above considerations are consistent with the ordering of the polytype phases in Figure 3.7.

The supersaturation (and growth rate) is anticipated to decrease with diameter as observed in Figure 3.4. This trend is indicated in Figure 3.7 by the arrows labeled “increasing diameter”. Evidently, the smaller diameter A-2 NWs had sufficiently high supersaturation to produce a twinned ZB phase in GaP segments as observed in Figure 3.5, while all other segments remained in the WZ phase.

Next, we consider the change in crystal structure from WZ to twinned ZB with increasing growth time within the GaP segment following each GaAs/GaP hetero-

interface in A-2 NWs. This behavior was depicted in Figure 3.6, where the transition from WZ to twinned ZB occurred and the twinning period became noticeably longer over time. This trend is illustrated in Figure 3.7(b) by the arrow labeled "increasing time". We postulate that this crystal phase change arises due to transient supersaturation behavior during growth after each hetero-interface. As growth progresses from the hetero-interface, the supersaturation gradually climbs and ZB becomes increasingly stable over WZ. This effect was previously observed and discussed in detail in Ref. [45].

Finally, we focus on the final 60 s GaP segment in the A-1 NWs (not shown in Figure 3.4), which behaved in a different manner compared to the earlier segments. This segment was found to contain the 4H crystal structure in all but the smallest diameter NW observed. To our knowledge, this is the first report of 4H GaP. The power spectrum of a ~10 nm segment is shown in Figure 3.8 showing the ¼ (000-2) reflection consistent with the 4H phase. The diameter fluctuations in Figure 3.8 were atypical and were neither observed on the other side of the shown NW nor on other NWs with 4H. Each 4H segment typically began within a few bi-layers of the GaAs/GaP hetero-interface and persisted between 10 to 14 nm in length along the GaP segment. WZ with a low density of stacking faults followed the 4H segment. The 4H phase was only observed in the final GaP segment of the A-1 NWs, and not in any of the preceding GaP segments. All NWs containing 4H exhibited a significant decrease in growth rate in the final GaP segment (<0.3-0.5 μm/h) compared with the previous GaP segments. Such a decreased growth rate would allow the supersaturation to fall to a level where 4H formation was preferred for a short duration.

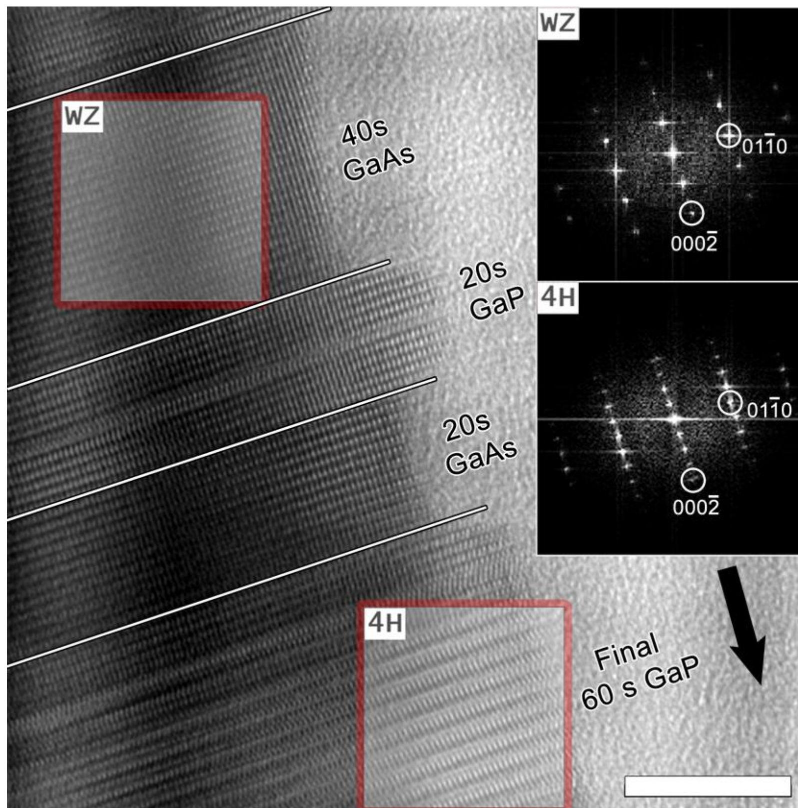

Figure 3.8: HR-TEM image of 4H GaP following the 20 s GaAs/ final 60 s GaP hetero-interface. The power spectrums are taken from the shaded regions and indicate the WZ (top) and 4H (bottom) phases. Hetero-interfaces are marked according to HAADF images (not shown) and the growth direction is indicated by the arrow. The scale bar is 10 nm.

The observation of different polytype phases in the present study has been linked to the segment growth rates (supersaturation). Although the present results have been explained on the basis of supersaturation, recently it has been demonstrated that the liquid-vapour interface energy is affected by a variation of the gallium pressure [104]. This interface energy influences the particle shape and the contact angle which in turn can affect the crystal structure [38,39]. On the basis of this theory, the Ga content of the droplet must vary with the NW radius, sidewall collection area, group V species, and growth interruptions to explain the present results.

3.2 Summary

At the time of publication, the predominant view that the chemical potential difference between the Au-III-V alloy droplet and the underlying semiconductor crystal controlled the crystal structure was being challenged. This was alluded to in the concluding paragraph of the discussion. Published almost simultaneously was the study by Algra et al., which described an experiment that leveraged the appearance of twinned ZB superlattice to correlate the supersaturation and the droplet surface energy with the twinning frequency [104]. This study convincingly removed the supersaturation as the direct cause of polytypism in NWs and instead demonstrated that the liquid-vapor surface energy of the VLS droplet controlled the twinning frequency in their experiments. At the same time a theoretical study on TPL nucleation was published by Krogstrup et al. examining the effect of droplet shape on the nucleation probabilities of ZB and WZ [39]. This study largely agreed with Algra et al. in that the wetting angle, and thus the droplet surface energy, had a large role to play in the formation of different polytypes. Moreover, the total volume of the droplet was also a factor. Under these revelations, crystal phase control during NW growth can only be achieved by achieving optimal contact angles for a specific droplet volume. These will in turn depend on the Ga content in the droplet to determine the volume and contact angle, but also the growth temperature, the effective V/III ratio at the droplet, and any other possible surfactants as demonstrated by Algra et al with Zn doping [39,104].

With these revelations, the results of "Polytype formation in GaAs/GaP axial heterostructures" can be placed in greater context. What was considered to be a change

in supersaturation ($\Delta\mu$) during writing was in fact a change in Ga concentration in the droplet. This change led to a change in volume and contact angle whereby the nucleation probabilities for different crystal phases changed accordingly. Further work was required to properly characterize the transient behavior following the GaAs/GaP hetero-interface which led to the formation of these polytypes.

Precise control of the local growth conditions of each NW is required in order to achieve such strict compositional and dimensional control over the VLS droplet. To this end, the method of fabrication used above was inadequate for future work. Instead, lithographic methods were required to exactingly position Au seed particles of identical diameters. While the benefits for controlled, uniform NW growth are obvious, numerous challenges exist and are discussed further in the subsequent Chapter.

4 Patterned III-V Nanowire Growth on Si (111) Surfaces using Molecular Beam Epitaxy

As introduced in sections 1.2.5 and 2.3, electron beam lithography (EBL) was used to precisely position Au particles on a substrate prior to MBE growth. This Chapter contains published work from "Pattern gold-assisted growth of GaP NWs on Si", by J.P. Boulanger and R.R. LaPierre, published in 2012 [76]. The work examines an interesting phenomenon that occurs when working with Au nanoparticles on Si substrates. The understanding of this behavior enabled the production of high yield, patterned NW arrays on Si(111) substrates.

4.1 Pattern Gold-Assisted Growth of GaP Nanowires on Si

4.1.1 Introduction

Nanowires (NWs) are commonly grown by the vapor-liquid-solid (VLS) method where a metal seed particle (usually Au) collects vapor-deposited material using molecular beam epitaxy (MBE) or metal organic vapor phase epitaxy (MOVPE). VLS growth by MBE is driven by the diffusion of adatoms from the substrate surface and NW sidewalls to the seed particle, where the growth rate exhibits an inverse dependence on NW diameter [3,30,31]. Thus, the seed particle diameter and deposition conditions control the NW growth rate and thus the crystal structures produced. Conversely, the lack of control of seed diameters leads to substantial spread in NW growth rates and variation in crystal structure of the NWs, as was demonstrated in the prior Chapter [51].

A further complication arises with a high surface density of NWs where shadowing effects from neighboring NWs can influence the local growth rate [45]. Therefore, it is desirable to control the seed particle diameter and position to enable the fabrication of a uniform array of NWs across large areas [79].

Several techniques have been demonstrated for the controlled deposition of Au seed particle diameter and position for patterned VLS growth. These include electron beam lithography (EBL) [84], nano-imprint lithography [85], poly-styrene spheres [88], and anodic aluminum oxide masks [87]. EBL is the most common technique for the fabrication of Au-assisted, ordered NW arrays using metal organic chemical vapor deposition (MOCVD) [84] and chemical beam epitaxy (CBE) [4]. Patterned MBE-grown NWs have also been shown previously [105]. Additionally, EBL has been used extensively in the patterning of MBE-grown self-catalyzed NWs [106]. In the present paper, we extend these earlier studies by discussing some subtleties in the growth of GaP NW arrays using EBL-patterned Au particles on Si substrates.

4.1.2 Experimental Details

Si (111) substrates were prepared with a 950k A3 PMMA resist, which was spin-cast at 2000 rpm for 1 minute followed by baking at 180 °C for 90 seconds. This process yielded a nominal resist thickness of 200 nm. EBL was conducted using a JEOL JSM-7000 field emission scanning electron microscope (SEM). The technique of spot lithography was used, where each Au seed particle was defined by a single beam shot of the resist. The dose per seed particle was varied systematically from 0.023 to 0.154 pC to achieve a

range of diameters from 70 to 140 nm. Both square and hexagonal symmetry patterns were fabricated with pitch varying from 500 nm to 1 µm.

Resists were developed in a 3:1 isopropyl alcohol (IPA) / methyl isobutyl ketone (MIBK) solution for 4 minutes. This was followed by a 1 minute bath in IPA and a 5 minute flowing deionized water rinse. The native oxide layer on the Si (111) surface in the developed regions was removed by a 10% buffered HF etch for 30 seconds and rinsed for 5 minutes in flowing DI water prior to Au deposition. A 10 nm thick layer of Au was deposited under high vacuum conditions and the resist lift-off was performed by ultrasonication in acetone. The patterns were verified by visible light microscopy and SEM. A representative pattern is shown in the SEM image of Figure 4.1. The diameter of the Au seeds was determined by SEM. Finally, the Si (111) substrate was indium mounted at 275 °C to a (100) Si wafer for compatibility with an existing substrate holder.

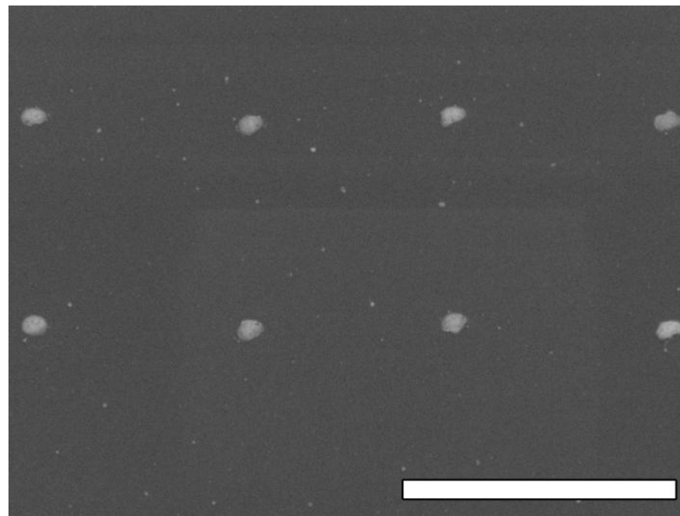

Figure 4.1: Plan view SEM image of EBL patterned Au seed particles formed by a 0.023 pC dose per Au dot. Scale bar is 1 µm.

Two samples were investigated. Sample A was directly loaded into the MBE following the indium mounting procedure. Sample B was subjected to a 30 second dip in 10% buffered HF immediately before loading into the MBE. As will be shown later, the HF etch was critical to successful growth of a patterned NW array. After loading into the MBE, both samples were degassed at 300 °C for 15 min under UHV conditions and annealed at 550 °C in an H_2 ICP plasma for 10 min. NWs were grown for a total duration of 15 minutes using a nominal 2-D equivalent GaP growth rate (Ga impingement rate) of 1 μm/h, a V/III flux ratio of 2.3, and a substrate temperature of 550 °C. Following growth, the NWs were cooled under a P_2 overpressure.

After growth, the NWs were characterized by SEM and scanning transmission electron microscopy (TEM) using a JEOL 2010F instrument at 200 kV. TEM was also performed using an FEI Titan G2 60-300 with an accelerating voltage of 300 kV and spherical aberration correction. A number of techniques were used including bright field (BF), dark field (DF), high resolution (HR), and high angle annular dark field (HAADF) imaging. Energy dispersive x-ray spectroscopy (EDS) was used to identify the composition of the Au particle and surrounding areas, whereas electron energy loss spectroscopy (EELS) was used to identify the presence of lower Z elements such as Si and O. Lamellas for TEM were prepared by a Zeiss NVision 40 focused ion beam (FIB) system. Additional TEM samples were prepared by removal of NWs from the substrate via an ultrasonication procedure.

4.1.3 Results and Discussion

Following growth, the samples were examined by SEM. Striking differences existed between samples A and B as shown in Figure 4.2. Tilted view SEM images for sample A NWs are shown in Figure 4.2 (a), (d) and (g) for e-beam doses of 0.023, 0.07 and 0.154 pC per Au dot, respectively, in a square pattern array. The latter doses corresponded to initial Au seed particle diameters, as determined by SEM images (e.g., Figure 4.1), of 71±4 nm, 126±1 nm and 145±1 nm, respectively. The positions of NWs appeared to be correlated to the expected positions of the patterned EBL Au dots. However, sample A exhibited tapered NWs, and many were without any preferred growth direction relative to the substrate surface. Multiple NWs were observed at the expected positions of the Au seed particles for all seed particle diameters. The occurrence and number of NWs originating from a single seed was a function of diameter, where larger diameter seeds led to a greater number of NWs. The latter observation is evident by comparing Figure 4.2(a), (d) and (g). Finally, a low density of NWs were found to exist near, but outside, the Au patterned areas as well as in small, isolated patches across the substrate. These NWs were highly tapered and randomly oriented like those found in the patterned arrays. No dependence of the NW array on pitch (i.e., spacing between the Au dots) was observed, indicating no proximity effects from neighboring NWs.

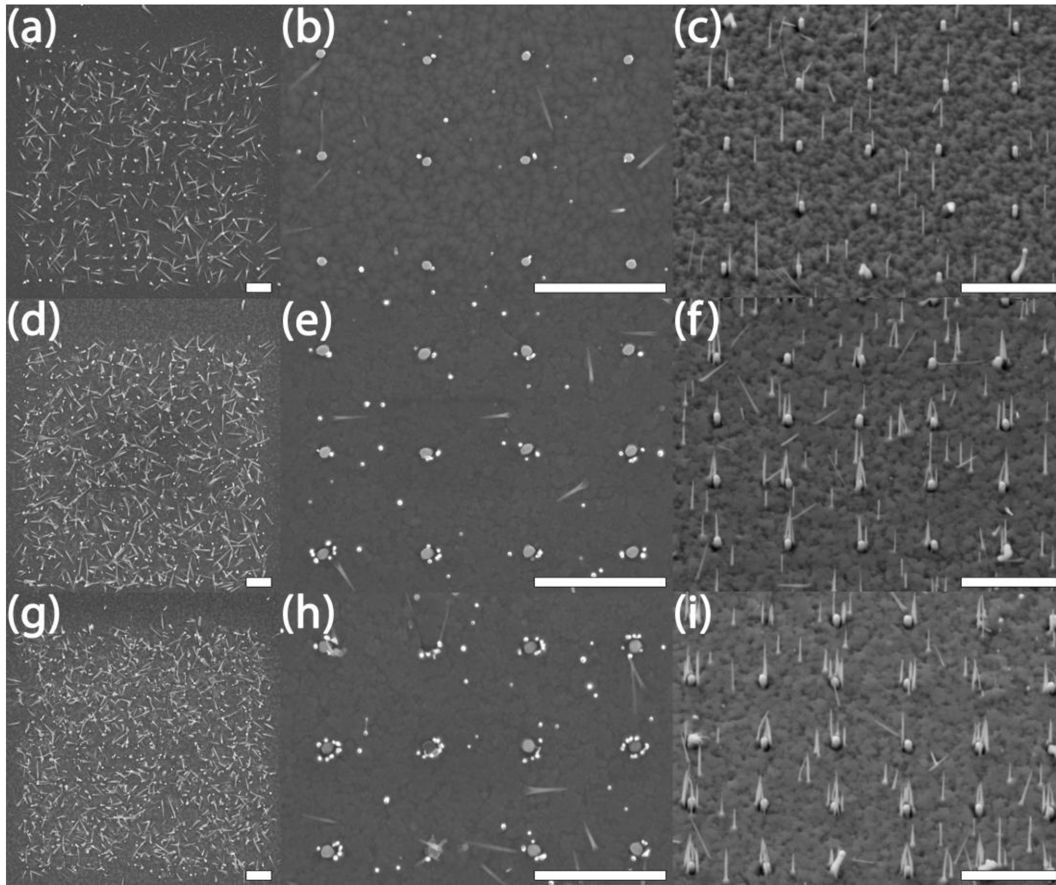

Figure 4.2: SEM images of square symmetry, EBL patterned NW arrays formed by 0.023 pC/dot (a) – (c), 0.07 pC/dot (d) – (f), and 0.154 pC/dot (g) – (i). The left column shows sample A at normal incidence. The middle and right column show sample B at normal and 25° from normal incidence, respectively. The scale bars indicate 1 μm.

In contrast to sample A, sample B NW positions coincided with the EBL pattern and the NW orientation was perpendicular to the substrate surface suggesting epitaxial growth from the Si substrate. Au was clearly visible at the tips of the EBL patterned NWs indicating that the NW grew by the VLS process. The yield of EBL patterned dots that resulted in NWs exceeded 90%. Figure 4.2 (b, c), (e, f) and (h, i) correspond to e-beam doses of 0.023, 0.07 and 0.154 pC per dot, respectively, identical to that used in

Figure 4.2 (a), (d), and (g) as discussed earlier for sample A. The latter doses resulted in initial Au particle diameters of 71±4 nm, 126±1 nm, and 145±1 nm as mentioned earlier for sample A. The NW diameter will depend on the diameter of the Au seed particle as well as the thickness of Au deposit and the wetting behavior of the Au particle on the substrate surface after heating the substrate to the growth temperature. The NW diameters determined by SEM were therefore 69±2 nm, 85±2 nm, and 97±1 nm with increasing dose as observed in Figure 4.2 (b, c), (e, f) and (h, i), respectively. Hence, unlike sample A, the NW diameter in sample B correlated with the diameter of the initial EBL patterned Au seed particle. Similar to sample A described above, sample B also exhibited a low density of thin, tapered NWs that were largely localized within and around the patterned areas as shown in Figure 4.2, but also found in random clusters across the substrate. Also, no dependence of the NW array with pitch was observed.

Sample A was further examined by TEM to ascertain the origin of the highly tapered, randomly oriented NWs. Although SEM was unable to resolve the Au seed particles at the tip of NWs in sample A, TEM performed on ultrasonicated NWs from sample A confirmed that all NWs were terminated with Au seed particles, verifying that NWs grew by the Au-assisted VLS process; however, the average diameter of the Au seeds at the tip of the NWs was only 6 nm, much smaller than the diameter of the patterned Au dots.

To determine the origin of the small Au nanoparticles described above for sample A, further TEM studies were performed using a TEM lamella prepared by FIB. This process facilitated the isolation and removal of NWs originating from the EBL

patterned locations (referred to as windows B and C) as well as those NWs originating from outside the patterned areas (window A), as shown in the SEM images of Figure 4.3(a) and (b). In the cross-sectional SEM image of the TEM lamella in Figure 4.3(c), the Si substrate, the GaP NWs and a thin GaP film that grew between the NWs are all visible. A carbon film highlights the extracted region in Figure 4.3(b) which protects the NWs during the FIB process.

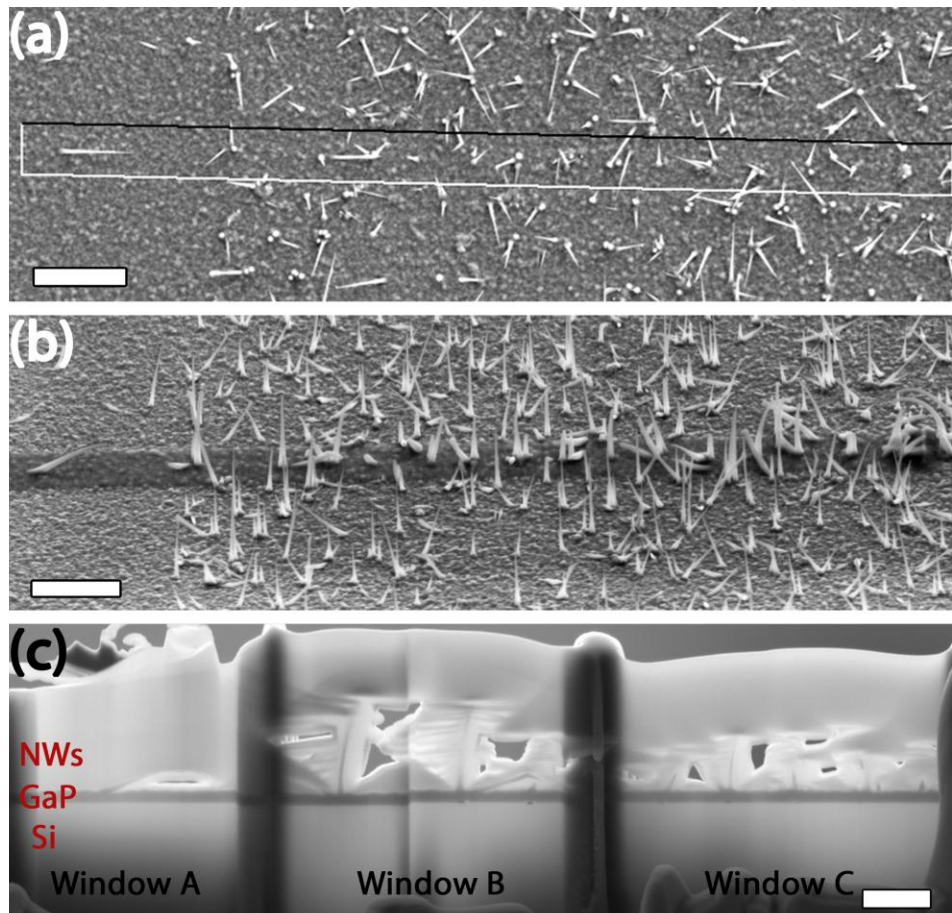

Figure 4.3: Plan view (a) and tilted view (b) SEM images of the lamella extraction area shown as a box in (a) and with a thin layer of carbon deposited in (b). (c) SEM image of the lamella after the ion milling of three windows labeled A, B and C from left to right. The scale bars indicate 1 µm.

Beginning with window A, a representative NW located outside the EBL patterned area was examined by DF-TEM as shown in Figure 4.4. The tilted GaP NW is embedded in a surrounding GaP film that grew concurrently between the NWs. The highly tapered morphology of the NW suggests that the Au seed particle, and original NW diameter, was very small. We believe these NWs grew from Au seed particles left as contamination on the substrate surface after the lift-off process. Indeed, Au contamination can be observed in Figure 4.1 as smaller Au nanoparticles located between the larger EBL patterned Au dots.

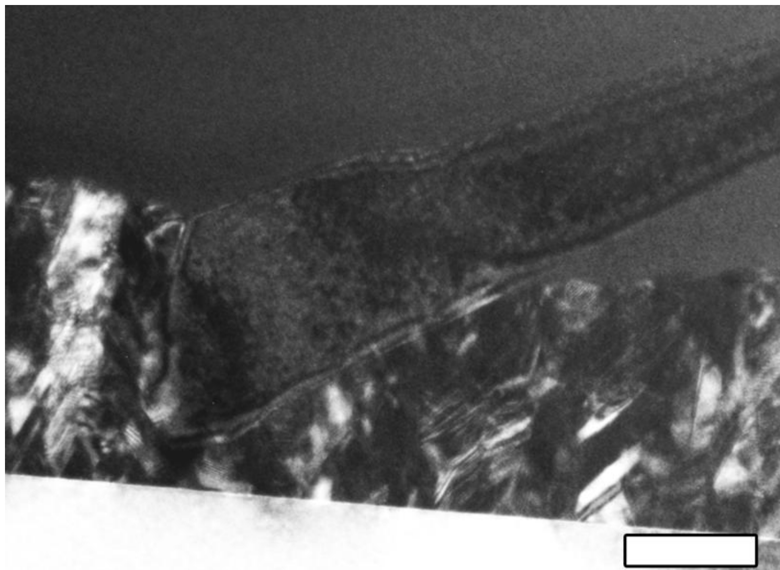

Figure 4.4: DF-TEM image of a randomly oriented NW that grew outside of the patterned Au array. This NW was obtained from window A in Figure 3(c). This image shows a single crystal tilted GaP NW protruding from a surrounding polycrystalline GaP film. Scale bar indicates 100 nm.

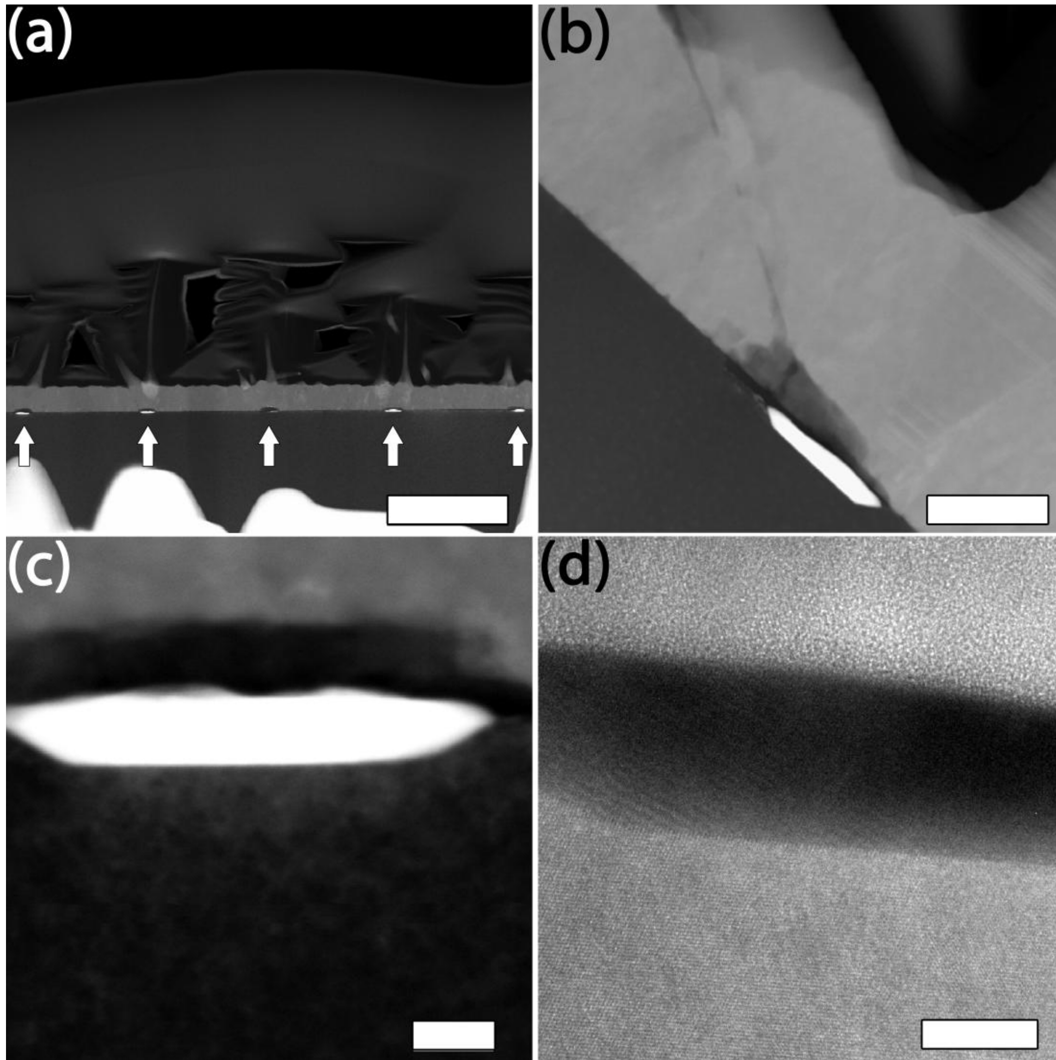

Figure 4.5: TEM analysis of FIB cross-section of patterned NWs from sample A. (a) HAADF image of window C. NWs can be seen above each Au dot, indicated by arrows, which is buried beneath a GaP film near the Si (111) substrate. (b) HAADF image of two NWs that originated from the right side of the Au dot (bright disk) where a film covering the Au dot is thinnest. (c) HAADF image showing the high-Z Au dot sunken into the Si substrate and covered by a low-Z film. (d) HR-TEM image of the Au dot in (c). The crystalline nature of the Si (111) substrate (bottom) and Au dot (middle) can be seen, but the overlying film (top) is amorphous. Scale bars are (a) 1 µm, (b) 100 nm, (c) 20 nm, and (d) 10 nm.

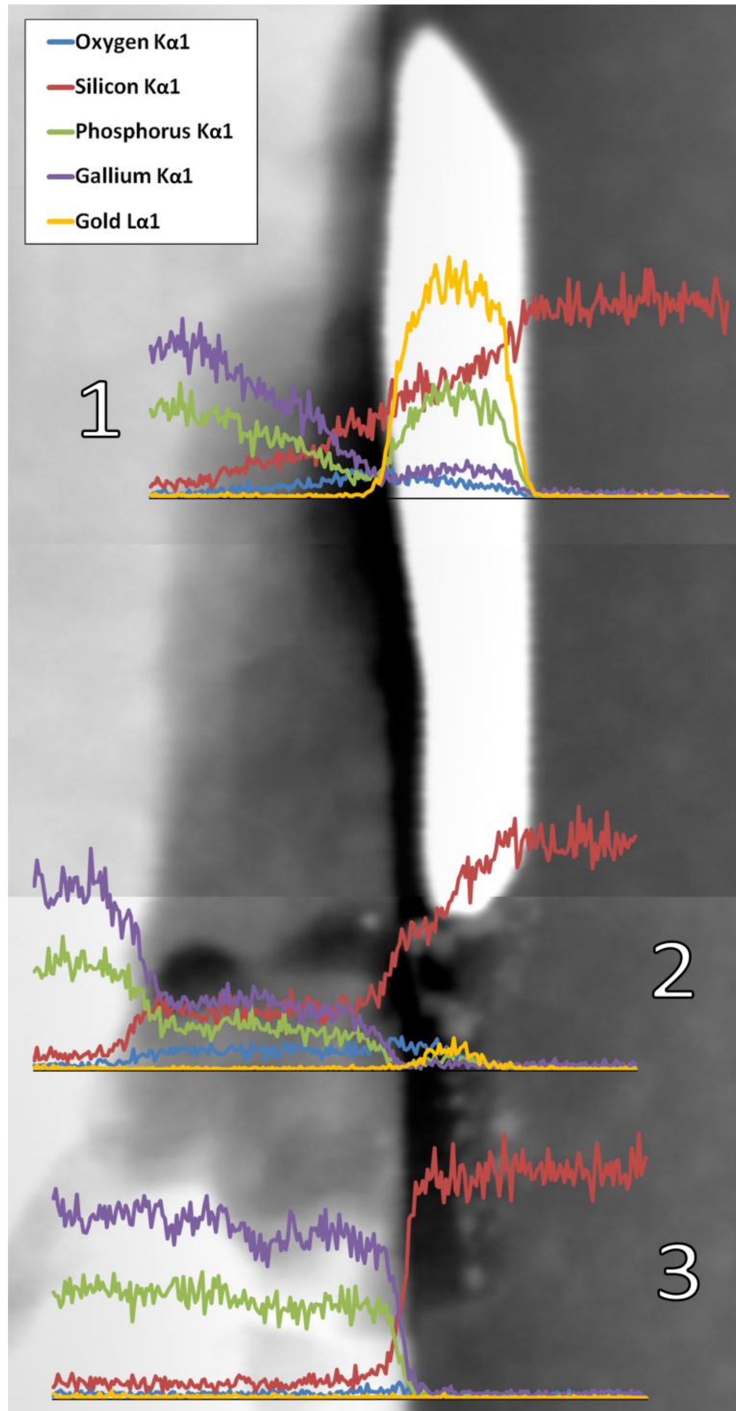

Figure 4.6: Composite HAADF image of an Au seed post-growth. The EDS linescan labeled "1" encompasses (from left to right) the GaP film, SiOx film, Au seed, and Si substrate. EDS linescan "2" encompasses the GaP film, SiOx film, Au residue, and Si substrate. EDS linescan "3" encompasses the GaP film and the Si substrate. Note that the P Kα1 and Au Lα1 x-ray peaks overlap, leading the EDS analysis software to misreport P in the Au seed in linescan "1". The scale bar designates 20 nm.

Next, NWs in sample A were examined whose location was correlated to the patterned Au seed positions. Au seeds were visible at the Si/GaP film interface, directly beneath the NWs in windows B and C as indicated by the arrows in Figure 4.5(a). Therefore, while the NW positions were correlated to the Au seed particle positions, the bulk of the deposited Au seed was buried and did not appear to contribute to NW nucleation in the usual Au-assisted VLS process.

Closer examination by TEM revealed that the EBL patterned Au particle clearly alloyed with the underlying Si substrate since the bottom Au-Si interface was positioned beneath the original Si (111) surface as clearly observed in Figure 4.5(b) and (c). HR-TEM imaging, as shown in Figure 4.5(d), revealed the presence of an amorphous layer covering each Au seed particle. The composition of these layers was determined qualitatively by EDS linescans, as shown in Figure 4.6. Linescan "1" was performed across a buried Au dot, indicating the presence of a silicon oxide layer positioned between the Au dot and the overlayer of GaP film, while only GaP and Si were detected outside the patterned Au dots (linescan "3"). The presence of an oxide above the Au dot is also suggested by the dark region between the Au dot and GaP in the HAADF image of Figure 4.5(c), indicating the presence of elements with low atomic number, Z. The composition of the amorphous capping layer was confirmed by EELS, which has greater sensitivity to low-Z elements than EDS. Targeting the region directly above the Au seed, EELS peaks were observed at 99 and 532 eV, corresponding to the $L_{2,3}$ shell for Si and the K shell for O, respectively [107]. No background levels of O were detected by EELS in the overlying GaP film. From the amorphous character in the HR-TEM, the HAADF

contrast, the EDS linescans, and the EELS measurements, it can be concluded that the amorphous layer is a silicon oxide of unknown stoichiometry (SiO_x).

As seen by the EDS linescan labeled “2” in Figure 4.6, some residual Au resided at the periphery of the large Au dot. This residual Au was probably left behind after either a movement or a shape change of the Au particle upon annealing at the growth temperature. As discussed earlier with regards to sample B, the initial Au dot diameters were indeed larger than the resulting NW diameters indicating a shrinking of the Au dot upon annealing. As seen in the HAADF TEM image of Figure 4.5(b), the thickness of the oxide covering the Au dot is non-uniform. Interestingly, two NWs extend from this region, suggesting that NWs were nucleated from the residual Au present at the edges of the Au dots. Thus, this may explain the origin of multiple NWs growing from the patterned Au dots in sample A as well as the proximity of parasitic NWs along the perimeter of the Au dots in sample B.

The appearance of a silicon oxide on the surface of thin Au films on Si substrates was reported by Hiraki et al. where a Au film on the Si surface acted as a catalyst for silicon oxide formation at temperatures far below the Au-Si eutectic [108,109]. The annealing of thin layers of Au on Si substrates at temperatures as low as 100 °C yielded oxide growth on top of the Au. Si migration through solid Au and oxidation on the top surface of the Au layer was proposed, despite being well below the Si-Au eutectic temperature of 363 °C. This phenomenon was briefly reported for EBL position-controlled GaP NW growth on Si (111) by MOCVD [110]. This report indicated the catalytic effect of Au with the Si surface to form silicon oxide was substantial even over

the course of a few days at room temperature. More recently, a comprehensive study of sub-10 nm Au nanodots on Si indicated the existence of a thin silicon oxide capping layer covering the Au nanodots due to Si diffusion through the nanodot followed by oxidation [111]. Moreover, evidence of Au diffusion through the oxide capping layer and Au particle formation was presented. Such behavior offers further explanation for the appearance of NWs over the SiO_x capped seed particles.

The indium mounting procedure used in the present study, which involved heating the substrate to 275 °C for 10-20 minutes, probably exacerbated the oxide formation process. The accidental growth of an oxide capping layer in sample A prevented the entire Au dot from becoming a seed particle for VLS growth as intended. Instead, it is evident that the trapping of the Au seed under the oxide layer led to NW growth from only small residual Au particles that escaped through oxide pinholes or uncovered edges of the original Au dot. In contrast, sample B underwent a buffered HF dip immediately preceding MBE growth. This resulted in the removal of the silicon oxide capping layer over the Au seeds, thus enabling patterned Au-assisted VLS growth.

The presence of some NWs outside the patterned regions of sample B is attributed to the lift-off procedure used during this experiment, where the substrate was submerged and ultrasonicated in acetone. During this step, some Au in solution may redeposit. The formation of stray NWs may be avoided by additional chemical cleaning as demonstrated recently [86].

4.2 Summary

In conclusion, the detrimental impact of low temperature oxidation on Au-assisted VLS growth of GaP NWs on Si (111) has been explored. Following Au deposition, a silicon oxide capping layer can form. Removal of the silicon oxide capping layer and restoration of Au-assisted VLS growth was achieved through buffered HF etching immediately preceding MBE growth. Optimizing the patterning processes to reduce or eliminate the Au-assisted oxidation process is pivotal in creating high quality, patterned III-V NW devices on Si substrates.

5 Patterned GaAs/GaP Heterostructures with Group V Oscillations

As the culmination of the work discussed in the prior Chapters, this Chapter contains work submitted for publication titled "Unveiling transient nanowire growth using group V oscillations", by J.P. Boulanger and R.R. LaPierre. In order to properly characterize the transient growth phenomenon observed in Chapter 3, the VLS seeds were patterned prior to growth using EBL. This technique was discussed thoroughly in sections 1.2.5 and 2.3 as well as Chapter 4. The patterned array of precise droplet dimensions and large nearest neighbor pitches provided the ideal environment in which to investigate VLS behavior.

5.1 Unveiling Transient Nanowire Growth Using Group V Oscillations

5.1.1 Introduction

Semiconductor nanowires (NWs) are a promising technology for novel heterostructures and the integration of III-V devices on Si. This largely arises from the small NW diameter, often only tens of nanometers, enabling elastic relaxation of strain arising from lattice mismatch or differences in the coefficient of thermal expansion [59,64,112]. This technology has promising applications in such areas as photovoltaics, photodetectors and LEDs [21,113,114]. Significant effort has been expended in furthering the understanding of NW heterostructures and related phenomenon [115–117].

Recently a marker technique capable of increasing the measurement resolution of axial VLS growth rates was demonstrated by Harmand et al. [32,33]. This method used group V composition modulations as marker layers to delineate the NW growth rate as a function of time. These oscillations are visible using high angle annular dark field (HAADF) imaging during scanning transmission electron microscopy (STEM). These oscillations can be counted and measured with regards to a spatial reference point and correlated with the real growth time. This technique enables measurements of NW length or instantaneous growth rate versus time without the need for complex *in situ* equipment or multiple growth experiments.

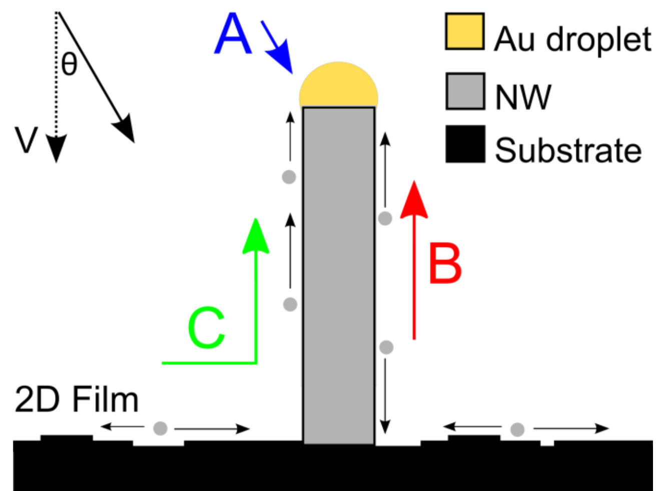

Figure 5.1: Schematic showing different adatom incorporation pathways. A refers to direct impingement. B refers to sidewall impingement and diffusion to the droplet. C refers to substrate impingement and diffusion to the droplet via the sidewall. V is the nominal 2D growth rate and θ is the Ga impingement angle.

Along with this experimental technique, Harmand et al. [32] fit the HAADF oscillation data in InAsP NWs with a phenomenological model, such as that first

introduced by Plante et al. and Tchernycheva et al. [30,118]. Here a similar model is introduced, schematically depicted in Figure 1.1, which describes the NW growth rate due to the impingement of adatoms:

$$\frac{\mathrm{dH_{NW}}}{\mathrm{dt}} = \frac{V\Omega_{\mathrm{NW}}}{\pi R_{NW}\Omega_{2DFilm}}(A + B + C) \quad (5.1)$$

$$\mathrm{A} = \frac{\alpha\pi\mathrm{R}_{\mathrm{Au}}^{2}}{\cos(\theta)} \quad (5.2)$$

$$\mathrm{B} = 2\beta R_{NW}H_{NW}(t)\tan(\theta) \quad (5.3)$$

$$\mathrm{C} = 0 \text{ if } \beta < 1 \quad (5.4)$$

$$\mathrm{C} = \pi R_{Eff}^{2} \text{ if } \beta = 1 \quad (5.5)$$

$$H_{NW}(t) = H_{NW,Total}(t) - H_{2D}(t) \quad (5.6)$$

As depicted in Figure 1.1, A in Equation (5.1) is the contribution due to direct impingement, B is the contribution due to adatom diffusion from the NW sidewalls, and C is the contribution due to adatom diffusion from the substrate. V is the nominal 2D film growth rate as determined by prior thin film calibrations; θ is the deposition angle of the group III source; Ω is the volume per group III atom in the respective solid; α is the fraction of group III adatoms that impinge on the droplet and contribute to axial NW growth (assumed to be unity); β is the fraction of group III adatoms that impinge on the NW sidewall, diffuse, and contribute to axial NW growth; and R_{Eff} is the effective collection radius on the substrate surface whereby all group III adatoms diffuse to the NW base, along the sidewalls, and then contribute to axial NW growth. $H_{NW}(t)$ describes the instantaneous height of the NW sidewall. H_{2D} is the 2D film thickness determined by

cross-sectional SEM and should approach the nominal film thickness for a sufficiently low density of NWs.

In this model, the two model parameters that describe growth are β and R_{eff}. β is a measure of the driving force for adatoms to diffuse to the droplet. When β values are low, there is an insufficient driving force for all the sidewall adatoms to diffuse to the droplet and therefore the remainder must diffuse towards the 2D film and incorporate near the base. Such a scenario has been previously described as a small chemical potential difference between the sidewall adatoms and the droplet [119]. Under such circumstances, a negligible diffusion flux from the substrate to the VLS droplet would occur (C=0). This is reflected in Equation (5.4) where C = 0 if $\beta < 1$. On the other hand, when β approaches unity, the driving force is such that all adatoms are collected from the sidewalls. Under these circumstances, adatoms from the substrate will now be collected as well by the VLS droplet and will be described by Equation (5.5).

In prior work with MBE grown GaAs NWs, β was found to take values between 0.27 and 0.4 [97]. Recent work by Harmand et al. found β approached unity during MBE growth of InAsP NWs [32]. In both cases, the data was fit assuming β was time-independent and that there was always a contribution of adatom flux from the substrate surface. Such an approach is appropriate if β=1 or if it is constant throughout growth; however, it will be shown that β is not strictly a constant and thus it must be allowed to vary with time. Therefore, the above model assumes that unless β approaches unity, the contribution from the substrate surface must be negligible.

5.1.2 Experimental Methods

NWs were grown on Si(111) wafers with lithographically patterned Au nanoparticle arrays. A 3” wafer was RCA cleaned prior to being spun with ZEP-520A resist. Six identical patterns were written across the wafer with an EBPG 5000+ electron beam lithography (EBL) system. The patterns were a hexagonal array of holes with a spacing of 2 μm. The patterns were developed in ZEP-N50 and then MIBK:IPA (9:1) solution. Remaining organic residue in developed areas was removed by a 20s O_2 plasma ash at 100W. The native silicon oxide layer was then removed with a 10% buffered HF etch for 30s and immediately placed under vacuum. 20 nm thick Au was deposited by electron beam evaporation onto a rotating substrate. The remaining ZEP-520A resist and undesired Au film was removed by a lift-off process that consisted of soaking and ultrasonicating the wafer in solutions of ZD-MAC, acetone, and IPA. Lastly, the wafer underwent a 2 min O_2 plasma ash to eliminate remaining organic residues. The 3” Si(111) wafer was then cleaved into six identical pieces, each with multiple 1mm x 1mm pattern areas in the center. The result of the preparation was six substrates with identical 2μm pitch hexagonal arrays with 65 ± 2 nm diameter Au disks.

Immediately prior to loading in the gas-source MBE, each substrate was etched for 30s in 10% buffered HF to remove any unwanted silicon oxide that may have accumulated around the Au nanoparticles. This Au-enhanced silicon oxidation was previously shown to inhibit NW growth [76]. Subsequently, the substrate was degassed in the MBE at 300°C for 15 min, ramped to the growth temperature of 600°C, and then subjected to an H_2 ICP plasma for 10 min as part of the standard growth procedure. The

substrate was rotated with a period of 4.6s during growth. Growths were conducted with a Ga impingement rate of 0.25µm/h as previously determined by (100) GaAs thin film calibrations. Group V species were supplied as As_2 and P_2.

In all samples, the first 30 min of growth was comprised of GaAs with a V/III flux ratio of 6. This step created a base segment from which subsequent structures could be spatially referenced. This base also produced enough height such that all subsequent NW structure was above the height of the 2D film growth and remained intact after NWs were detached from their substrate by ultrasonication for TEM. By the end of the 30 min GaAs base segment, NWs in each growth were thus far identical with respect to their preparation, diameter, and length.

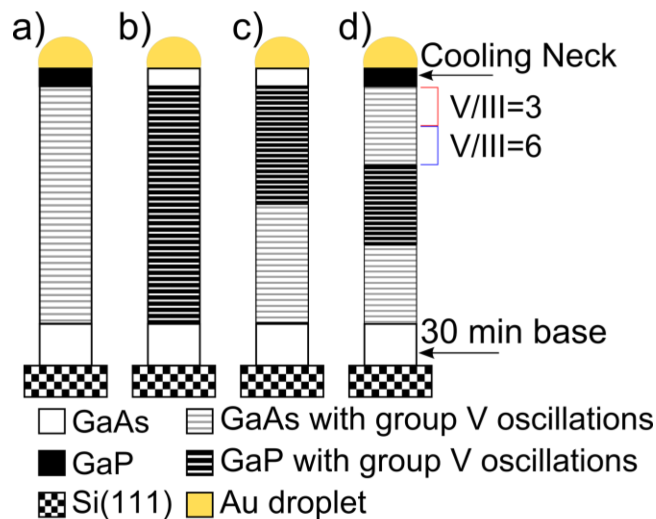

Figure 5.2: Samples used for the study of VLS growth of GaAs/GaP heterostructures. a) Sample A - GaAs. b) Sample B - GaP. c) Sample C - GaAs/GaP. d) GaAs/GaP/GaAs(V/III = 6)/GaAs(V/III=3). All samples were grown with the same 30 min duration of a GaAs base segment.

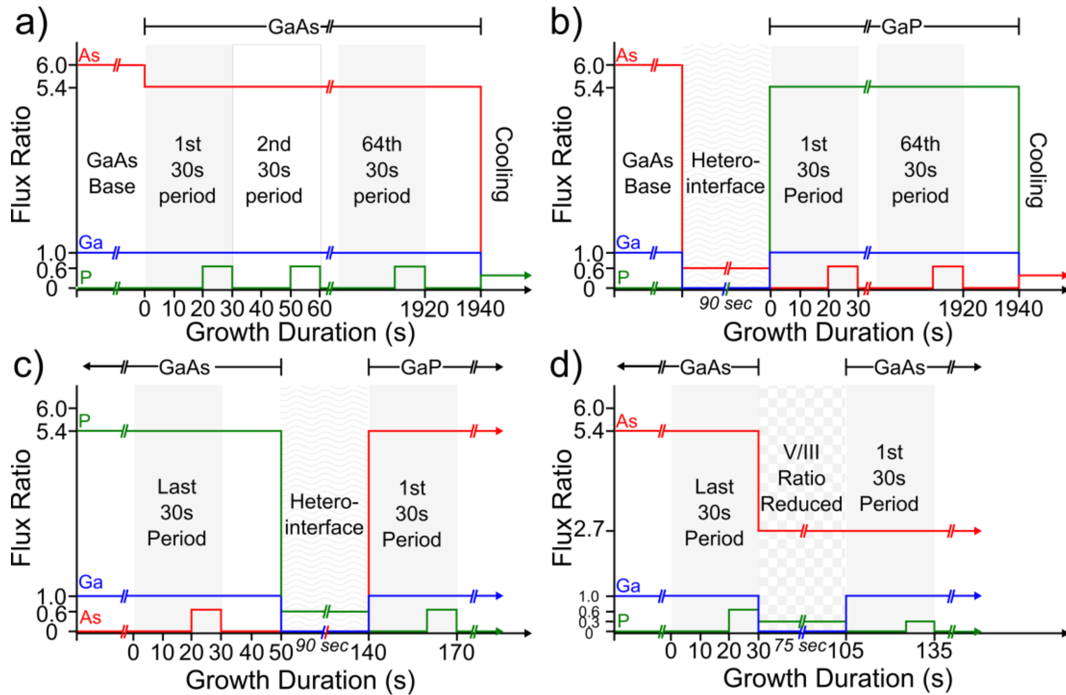

Figure 5.3: MBE group III and V impingement flux ratios normalized to Ga. a) Sample A. b) Sample B. c) Sample C, showing the procedure for forming a hetero-interface between GaAs and GaP as found in samples A and B, respectively. d) Sample D, showing the procedure used to reduce the V/III ratio.

After growth of the GaAs base, four different structures were grown. Sample A (Figure 5.2a and 5.3a) contained 64 periods with a repeating unit of 20s GaAs and 10s of $GaAs_{0.9}P_{0.1}$ (nominal). Similarly, sample B (Figure 5.2b and 5.3b) contained 64 periods with a repeating unit of 20s GaP and 10s $GaAs_{0.1}P_{0.9}$ (nominal). Next, sample C (Figure 5.2c and 5.3c) contained both a GaAs segment similar to sample A followed by a GaP segment similar to sample B, both containing 30 periods. Finally, sample D (Figure 5.2d and 5.3d) contained GaAs, GaP, and then GaAs segments each with 20 periods. The first 10 periods of the last GaAs segment were grown with a V/III flux ratio of 6, while the final 10 periods of GaAs were grown at a V/III flux ratio of 3.

During group V oscillations within GaAs (GaP) segments, the As_2 (P_2) flux was held at a V/III flux ratio of 5.4. During the formation of a $GaAs_{0.9}P_{0.1}$ ($GaAs_{0.1}P_{0.9}$) marker layer, a P_2 (As_2) flux equivalent to an incremental increase in V/III ratio of 0.6 was input, resulting in a total effective V/III flux ratio of 6. In this way, small compositional variations were introduced at the expense of small perturbations in V/III flux ratio. At the end of growth, each structure was cooled under group V overpressure. Samples A and D were cooled under P_2 flux in order to clearly distinguish the NW growth formed during droplet cooling. Similarly, structures B and C were cooled with As_2.

Hetero-interfaces in this experiment were formed with the procedure depicted in Figure 5.3(c). Following the final GaAsP marker, the segment ended with 20s of pure binary material. Next, the Ga cell was shuttered for 90s to adjust and stabilize the group V pressures for the upcoming segment. This is a standard practice to form abrupt hetero-interfaces. During this time, the group V species that was the majority constituent in the previous segment was held at a reduced pressure equivalent to a V/III flux ratio of 0.6. When growth was resumed by re-opening the Ga cell shutter, the new group V species replaced the old species with a V/III flux ratio of 5.4. Again, a pure binary segment was grown for 20s.

Finally, Figure 5.3(d) depicts the reduction in V/III flux ratio in sample D. During the growth of the final GaAs segment and after ten group V oscillations, the V/III flux ratio was reduced by a factor of two. As shown in Figure 5.3(d), the group V flux was reduced over a 75s period with the Ga source shuttered. During this time both the As_2 and P_2 flux were continued while reducing their nominal impingement values from 5.4

and 0.6, to 2.7 and 0.3, respectively. Upon the recommencement of growth, ten more group V oscillations were grown. This began with pure binary GaAs growth for 20s.

After growth, the NW morphology was observed using a JEOL JSM-7000 scanning electron microscope (SEM) operating at 5 kV. Bright-field (BF), selective area diffraction (SAD), high angle annular dark field (HAADF), and energy dispersive x-ray spectroscopy (EDS) analysis of individual NWs was performed in a JEOL-2010F transmission electron microscope (TEM) operating at 200 kV. For this purpose, NWs were transferred to a lacey carbon-coated copper TEM grid. This was accomplished by placing the patterned substrate in methanol or IPA solution, ultrasonicating for 2 min, and then dropping and drying several 2µL droplets onto a suspended TEM grid. Where multiple high magnification images were used, the images were stitched together using the image stitching function in the freely available microscopy analysis software package called FIJI [82,83]. Image scale calibrations were refined to an optimal thickness measurement error of 2% using a Mag*i*Cal SiGe quantum well superlattice sample from Norrox Scientific Ltd.

5.1.3 Results

A typical SEM image of NWs from sample A is shown in Figure 5.4, which is also representative of the other samples. Growth conditions were such that rod-shaped NWs grew with negligible tapering indicating negligible sidewall growth. The length and diameter of over fifty vertically oriented NWs were measured for all four samples, A to D. NW length including standard deviations for samples A, B, C, and D were 780 ± 160 nm, 680 ± 150 nm, 670 ± 130 nm and 560 ± 120 nm, respectively. NW diameter

including standard deviations for samples A, B, C, and D were 57 ± 5 nm, 56 ± 5 nm, 62 ± 4 nm and 55 ± 5 nm, respectively. As is evident in Figure 5.4, a rough 2D film grew between the NWs.

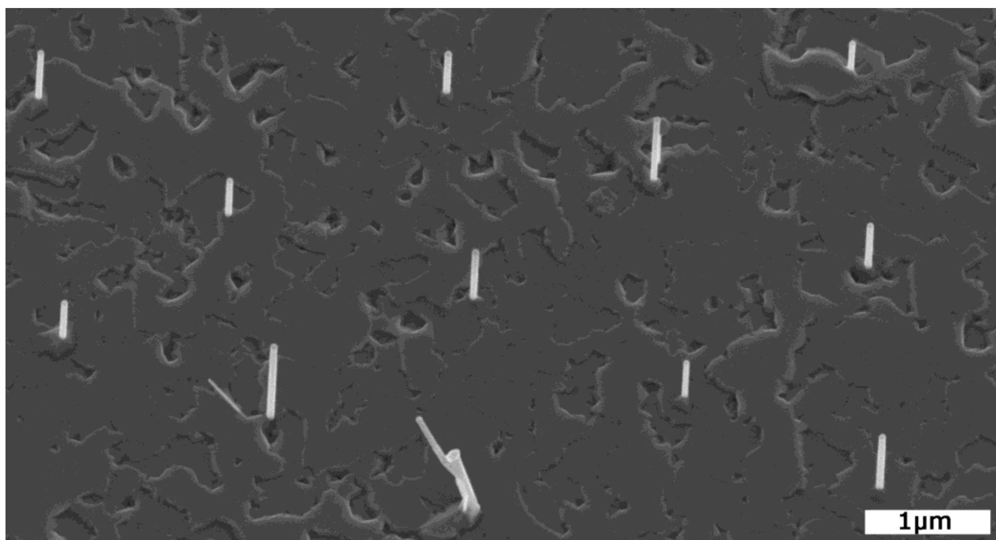

Figure 5.4: 25-degree tilted SEM image of NW array from sample A. Scale bar is 1 μm.

Multiple NWs were characterized by TEM from each sample. NWs were examined on the (2 -1 -1 0) zone axis in BF TEM and SAD mode to characterize the crystal structure. This analysis indicated that all NWs were wurtzite with occasional stacking faults. EDS analysis of the VLS droplet was performed to determine its composition. The common issue with interpreting such results is the lack of information as to how much Ga was lost during cooling due to incorporation into the NW cooling neck. Prior studies have identified the cooling neck based on the change in NW diameter or crystal phase [51,120]. Here, since cooling takes place under a different group V species, the cooling neck can be measured very accurately by its contrast in both HAADF and BF TEM. The alloy composition of the VLS droplet during growth can then be

calculated by estimating the droplet as a truncated sphere and the NW as a cylinder. By this method, the Ga composition of the droplet prior to terminating growth was determined to be 31 ± 2 at% across all NWs examined and all samples A-D.

This compositional estimate should be regarded as a minimum value as desorption or diffusion of Ga to the 2D film could not be accounted for. Previously, Harmand et al. compared MBE grown GaAs NWs cooled with and without As overpressure, finding 31 at% and 50 at% Ga, respectively [120]. It was concluded that as much as 20 at% Ga did not incorporate or remain in the droplet during cool down under As overpressure. Dubrovskii et al. have demonstrated that Ga may incorporate into the 2D film when the droplet is held under As overpressure [46]. Therefore, growth compositions of up to 50 at% Ga in this study may have been possible.

Next, the NWs were tilted to the (0 1 -1 0) zone axis where contrast contributions from stacking faults are invisible [121], allowing easier observation of the intentional composition modulations, as shown for example in Figure 5.5(a) for sample B. The HAADF intensity line profiles, such as that shown in Figure 5.5(b), were peak fitted to extract the instantaneous growth rate. It was assumed that the peak of each contrast oscillation coincided with the middle of the actual composition modulation.

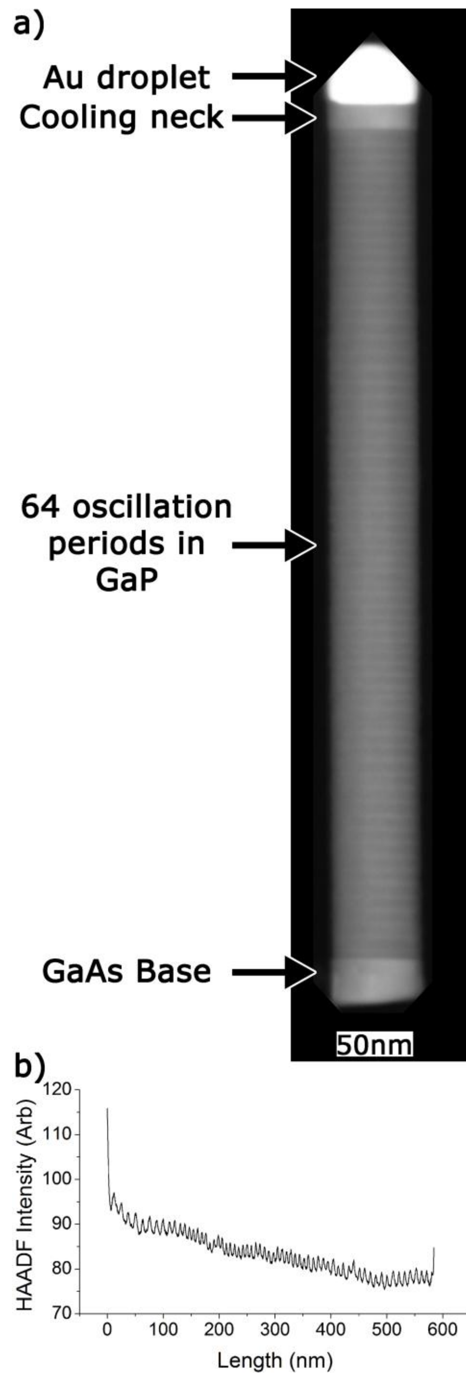

Figure 5.5: a) HAADF image of a NW from sample B. b) Typical HAADF profile for sample B.

5.1.4 Model Results

β and R_{eff} were fit to the HAADF intensity profiles using Equations (5.1) - (5.6). The Matlab code used to fit the model can be found in Appendix C. In addition, the contribution to the growth rate from direct impingement to the droplet, adatom diffusion from the NW sidewall, and adatom diffusion from the substrate was determined from the extracted model parameters. These results are summarized in Figure 5.6 for samples A, B and C. Sample D will be considered later.

Beginning with sample A (the GaAs structure), Figure 5.6(a) shows for several NWs that β decreased with time. However, Figure 5.6(b) shows the sidewall contribution and the total growth rate increasing with time, as is the common observation for diffusion-induced NW growth [30]. This seemingly contradictory behavior was the result of the sidewall cross-sectional area increasing with growth even though β was decreasing (see Equation (5.3)). In other words, more Ga adatoms were diffusing to the droplet and being collected despite the sidewall collection efficiency (β) decreasing. In all cases, β was below unity. The low β value meant that the growth rate contribution of diffusing adatoms from the substrate was negligible (Eq. 4); i.e., R_{eff} = 0, as indicated in Figure 5.6(a).

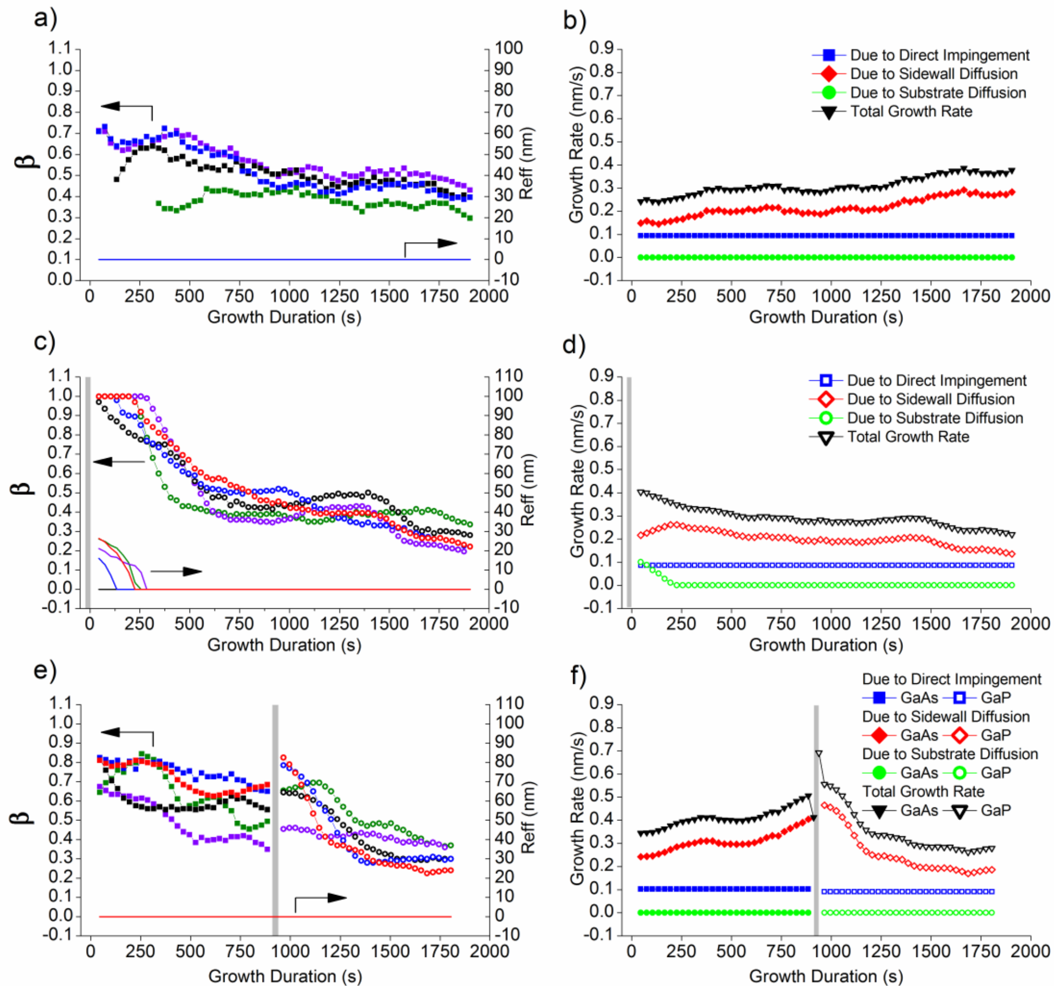

Figure 5.6: Left column shows β and R_{eff} values for several NWs. The right column shows the instantaneous growth rate as well as the separate contributions from direct impingement, sidewall diffusion, and substrate diffusion for a representative NW. Figures A) and B), C) and D), and E) and F) correspond to samples A, B, and C, respectively. The location of growth interruptions (hetero-interface) are indicated by grey shading.

Sample B (the GaP structure) exhibited starkly contrasting behavior in Figure 5.6(c) and (d). The initial GaP growth rate for NWs from sample B was greater than that of GaAs in sample A. Indeed, β was essentially unity at the initiation of GaP growth. During this time the GaP growth rate was so high that not only were all adatoms

collected from the sidewall, but an adatom diffusion flux from the substrate also contributed to the axial VLS growth. As a result, R_{eff} reached values up to 26 nm during this time. Figure 5.6(d) demonstrates that the magnitude of the flux from the substrate was on the order of the direct impingement flux to the droplet. As in sample A, β decreased as time progressed, resulting in a decrease then cessation of diffusion from the substrate. Unlike sample A for GaAs, the sharp decline in β with time resulted in a decrease of growth rate as shown in Figure 5.6(d).

To verify the qualitative behavior observed in samples A and B, the experiment was repeated in sample C which contained both a GaAs segment (as in sample A) followed by a GaP segment (as in sample B). As shown in Figure 5.6(e) and (f), β decreased with time for both the GaAs and GaP segments as observed in samples A and B. The growth rate for the GaAs segment increased with time, while the growth rate for the GaP segment decreased with time, also consistent with the behavior observed in samples A and B. Finally, β was larger for the GaP segment compared to the GaAs segment near the hetero-interface, again consistent with samples A and B.

From these observations, the following conclusions can be made. The transition from GaAs to GaP growth leads to a significant change in the ternary alloy droplet whereby the driving force for Ga adatom diffusion towards the droplet (β) is greatly enhanced. It is proposed that this sudden shift in the driving force arises due to the incorporation of P in the droplet.

VLS growth proceeds in a manner described as "nucleation anti-bunching" or "self-regulated pulsed nucleation" [33–35]. When the supersaturation (ζ) of the droplet

increases to a critical value, the formation of a 2D nucleus becomes highly probable. Following nucleation and fast island growth of the layer, the supersaturation of the droplet decreases sharply. The refilling of the droplet with growth species again leads to the supersaturation increasing to the critical value. For a fixed set of conditions, the rate of nucleation will be related by the rate of increase of the supersaturation during the droplet refilling stage.

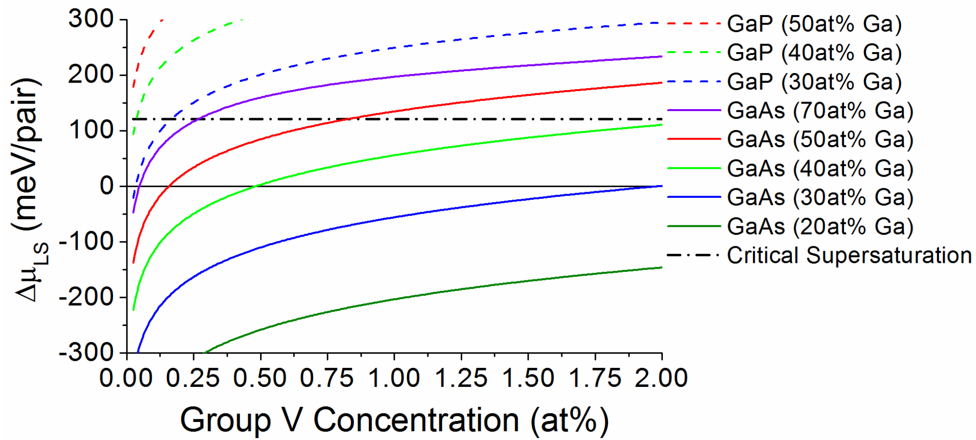

Figure 5.7: The chemical potential difference per pair between the alloy droplet and the solid crystal ($\Delta\mu_{LS}$) at 600°C and several different Ga concentrations.

To better understand our observations, the chemical potential difference per pair between the alloy droplet and the solid crystal ($\Delta\mu_{LS}$) for GaAs and GaP are plotted in Figure 5.7, using the data provided in Ref. [122]. The critical supersaturation of 121 meV was also plotted in Figure 5.7 based on an example given for MBE GaAs NW growth by Dubrovskii and using the relation $\Delta\mu_{LS}=k_BT\ln(\zeta+1)$ [34]. A similar value was reported by Krogstrup et al. for MBE Ga-assisted growth of GaAs NWs [35]. In the present analysis, this value is approximate and its absolute magnitude has little impact on the

qualitative understanding of the results. For simplicity, the critical supersaturation is assumed to be the same for both GaAs and GaP growth.

The striking aspect of Figure 5.7 is the large difference between $\Delta\mu_{LS}$ for GaAs and GaP growth. The range of group V concentration in Figure 5.7 is possible according to previous reports [33]. First, consider the growth behavior of sample A in the context of Figure 5.7, which is reproduced in Figure 5.8(a). For sample A, β was found to be decreasing with time. This is proposed to be the result of a slowly increasing Ga concentration in the droplet under the growth conditions used. This is qualitatively indicated in Figure 5.8(a) by the arrow from point A to B. This indicates that a growing Ga concentration will reduce the necessary As concentration in the droplet.

The growth of GaP in Samples B and C demonstrates very different behavior than observed for GaAs. In both cases, growth starts with GaAs. Growth is halted by terminating the Ga beam and reducing the V/III flux ratio from 5.4 to 0.6 and holding for a period of 90s. Experimental observations indicate a dip in the growth rate in the final GaAs period just prior to the hetero-interface in Figure 5.6(f). Since the growth rate of this segment is expected to be identical to those prior, this observation is interpreted as the dissolution of the final GaAs segment during the growth interruption. This behavior was ubiquitous for all GaAs-GaP hetero-interfaces in sample C and D. "Negative growth" has been both theorized and observed by Dubrovskii et al. for Au-assisted GaAs NWs grown by MBE [46]. Dubrovskii concluded that Ga could be absorbed from the NW crystal and held in the droplet or allowed to migrate down the NW to incorporate in the 2D film. The low As concentration due to a very low As overpressure and a diffusion flux

of Ga from the droplet to the substrate gradually decreases $\Delta\mu_{LS}$. Therefore, a negative $\Delta\mu_{LS}$ with reduced Ga and As content in the droplet is expected during the growth interruption and drawn accordingly in Figure 5.8(a) as the transition from point 1 to 2.

Following the 90 s interruption between GaAs and GaP, the Ga and P_2 sources are opened and the As_2 source is closed simultaneously. At this time the droplet became alloyed with P while the remaining As content desorbed or incorporated in subsequent growth. This change in group V species has drastic consequences for the droplet's supersaturation as shown by the arrow between points 2 and 3 in the magnified view of Figure 5.8(b), assuming no change in Ga content of the droplet.

When P incorporates following the GaAs-to-GaP hetero-interface, the critical supersaturation is attained almost instantaneously, triggering the first nucleation event. A rapid succession of nucleation events occur as only minute P concentrations are required to reach the critical supersaturation. This process results in a rapid depletion of Ga from the droplet shown by the arrow between points 3 and 4 in Figure 5.8(b).

Experimentally, this rapid purging of Ga from the droplet was observed as an abrupt increase in the growth rate of GaP immediately following the hetero-interface, which did not persist beyond the first oscillation period (see Figure 5.6(f)). The extra length of the initial GaP period compared with the subsequent periods was observed to be 5 nm on average, corresponding to a decrease in Ga concentration of the droplet by up to 10 at%. The purging of Ga from the droplet promoted a subsequent increase in the diffusion flux of Ga to the droplet; i.e., a sharp increase in β in Figure 6e followed by a decline in β for 250-500 s as an equilibrium in Ga flux was re-established. This process

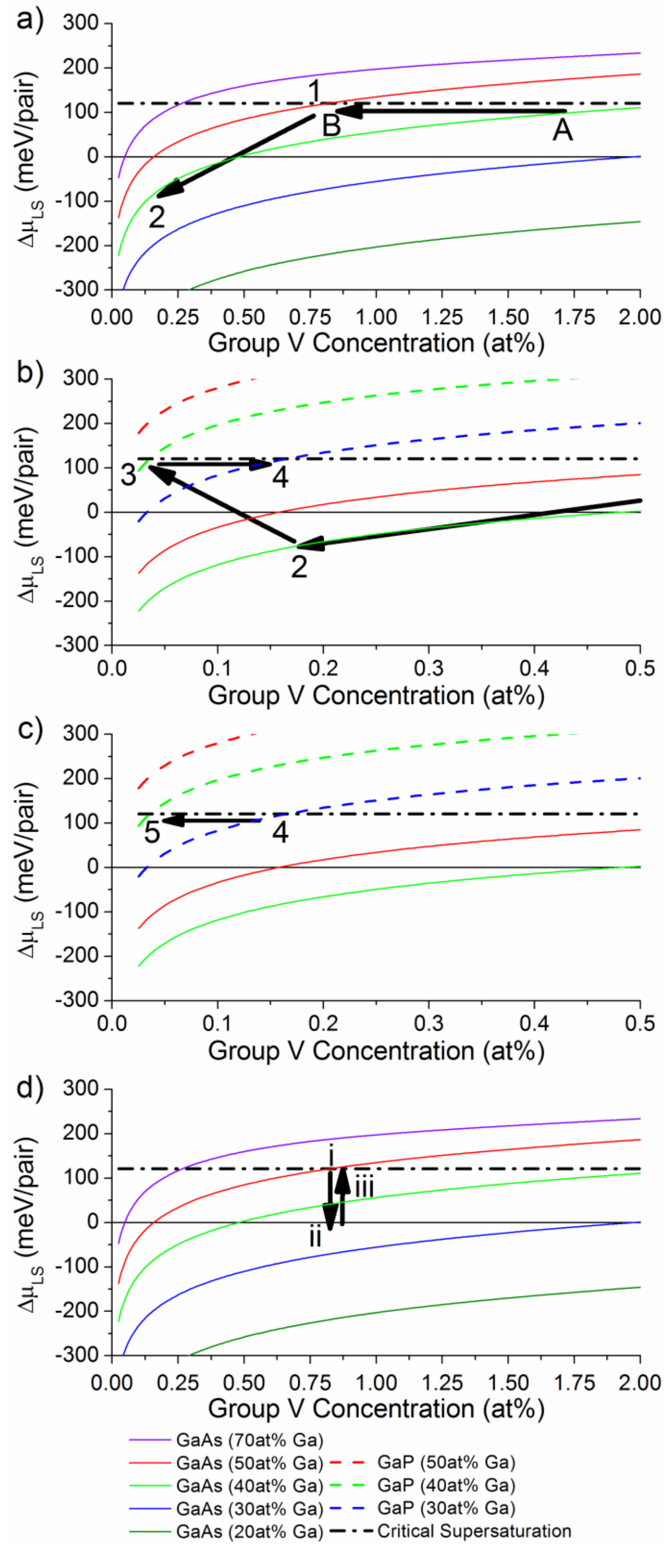

Figure 5.8: $\Delta\mu_{LS}$ at 600°C and several different Ga concentrations.

is shown by the arrow from 4 to 5 in Figure 5.8(c). Subsequently, the decline of β slows, taking a "steady-state" character like that observed for sample A.

Hetero-interfaces have been previously linked to stacking fault reduction or phenomena such as the appearance of 4H [13,51,52]. Here it has been shown that large changes to the droplet composition occur as the result of the change in group V species, which sheds further light as to how droplet compositions far outside of steady-state could lead to unique crystal phases such as 4H following a hetero-interface. Modified droplet compositions would lead to different surface energies, volumes, and contact angles, which are all expected to control crystal phase [39,104]. Changes in growth rate were linked with changes in crystal phase in a similar study of MBE grown GaP NWs [119].

Besides the implications for crystal phase purity, purging and transient growth rate behavior have serious implications for the fabrication of devices, the most obvious being a reduction in control when creating precise layered structures such as quantum dots within NWs. Further consideration towards the minimization of these effects will be required when engineering NW heterostructure devices.

5.1.5 Effect of V/III Ratio and GaP-to-GaAs transition

Sample D was grown with a change of the effective V/III flux ratio in the GaAs segment from 6 to 3 as shown in Figure 5.9. In all NWs, β did not change upon the reduction in the V/III flux ratio, but continued in a similar manner to that of sample A. This validates the assumption that during "steady-state" NW growth Ga is indeed the

limiting growth species, consistent with the phenomenological model implemented in this study.

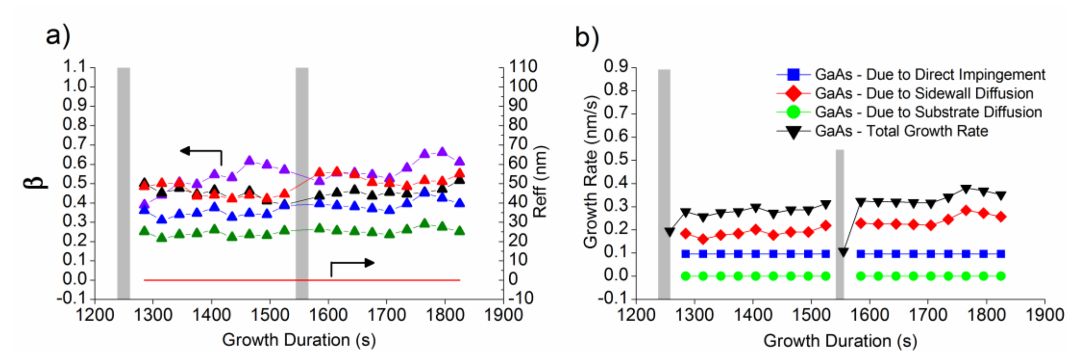

Figure 5.9: a) β and R_{eff} values several sample D NWs. b) Instantaneous growth rate as well as the separate contributions from direct impingement, sidewall diffusion, and substrate diffusion for a representative NW. The location of growth interruptions (left: GaP-to-GaAs hetero-interface; right: V/III ratio changes) are indicated by grey shading.

During the growth interruption required to reduce the group V pressure, a mixture of As_2 and P_2 flux was held during a period of 75s while the V/III ratio was reduced by half (see Figure 5.3(d)). As before, a loss of Ga from the droplet is expected, manifesting as the movement from point i to ii in Figure 5.8(d). Upon resuming the Ga flux, the supersaturation of the droplet was inadequate for nucleation to occur immediately. Instead, an incubation period occurred due to the delay caused by refilling the Ga content in the droplet, depicted as the transition from ii to iii in Figure 5.8(d). A return to the same Ga and As concentrations are expected since β was similar before and after the V/III ratio switch. As this behavior is related to the resumption of growth with GaAs, the same refilling behavior was observed following the growth interruption during the GaP to GaAs hetero-interface, as seen in the left edge of Figure 5.9(b).

The vertical nature of the movement in Figure 5.8(d) highlights that the As concentration was not anticipated to change. This assumption is based on the experimental evidence showing β remained constant despite the change in V/III flux ratio. If the As concentration in the droplet had decreased as a result of the lower As impingement rate then a larger Ga concentration would be required in order for growth to proceed. This higher Ga concentration would then lead to a lower driving force for Ga diffusion to the droplet and a lower β, which was evidently not the case.

5.2 Summary

The use of group V oscillations has been shown to be a powerful tool for investigating NW growth phenomenon. This study has investigated GaAs/GaP axial NW heterostructures and revealed many valuable insights. The most profound discovery was the large transient response of the GaP growth rate following a hetero-interface formed during a growth interruption, a common practice for fabricating abrupt interfaces. This transient behavior has been linked to the large difference in As or P alloy concentrations required to reach the critical Supersaturation.

The most obvious implication of the transient behavior is the highly non-linear growth rate. Furthermore, the growth interruption during hetero-interface formation also led to dissolution, purging, and refilling effects. This transient behavior complicates the process of forming precise layer structures such as periodic quantum wells. Further consequences are expected as well, such as non-uniform doping as well as crystal phase polytypism.

6 Conclusions and Future Work

6.1 Thesis Summary

The growth of Au-assisted VLS NWs with GaAs/GaP axial heterostructures was conducted by GS-MBE. Early results indicated several sources of inhomogeneity between NWs in the array:

i. NWs were grown using self-assembled VLS seeds formed during Au thin film annealing. These films cover the substrate with spatially random VLS seeds with a broad range of diameters. This led to a significant disparity in growth conditions from NW to NW under the diffusion-induced environment. This was a detriment to not only GaAs/GaP structures, but to all proposed NW devices.

ii. During the growth of GaAs/GaP superlattice structures, varying layer lengths within a NW were observed. This phenomenon was not expected and revealed VLS specific behavior.

iii. Subsequent experiments revealed transient growth phenomena were present following the transition from GaAs to GaP. The transient behavior led to changes in growth rate and crystal structure. Electron microscopy investigations of these heterostructures led to the discovery of 4H GaP, a previously unreported polytype.

From these findings, it was clear two objectives must be met. First, the use of substrates with patterned VLS seeds with highly uniform diameter would create more

homogeneous NW growth conditions within the MBE. Second, a better understanding of the transient behavior following the GaAs to GaP hetero-interface. Work towards these goals led to the following primary results:

a) The identification of a low temperature silicon oxide layer that forms in the presence of Au nanoparticles. The silicon oxide acted as a capping layer, preventing the VLS mechanism during MBE growth. The removal of this layer by etching immediately prior to MBE growth enabled VLS growth from patterned VLS seed arrays.

b) The attainment of Au-assisted patterned VLS growth by MBE with reproducible vertical yields above 50%, sufficient for studying growth processes.

c) A comprehensive electron microscopy study of patterned GaAs/GaP heterostructure NWs with group V oscillations led to the quantification of the instantaneous growth rate. Modeling of this data and the application of VLS growth principles led to an understanding of the transient behavior following the GaAs to GaP hetero-interface. This transient behavior was the result of the large difference in $\Delta\mu_{LS}$ when alloyed with As or P. Dissolution, purging, and refilling behavior that can occur during and immediately following growth interruptions was also described as a function of droplet composition.

6.2 Future Work

There is a strong motivation for further improvements in the homogeneity of NW growth by MBE. As alluded to in this thesis, the formation of uniform NW arrays is pivotal for the fabrication of NW device arrays whether they are heterostructure devices or not. To this end, further work on the patterning process for Au-assisted VLS growth is highly recommended. The positive preliminary results of over 90% vertical NW yield indicate that such a goal is not only possible, but is a matter of tuning the growth parameters to make it favorable. The optimal growth conditions may be realized by looking towards Ga-assisted VLS growth where vertical yields approaching 100% have been reported [106]. Indeed, the reduction of the droplet surface energy by making the alloy droplet more Ga rich may make the growth in the [111] direction more favorable than crawling along the Si(111) surface until it is covered with a GaAs(111) film. The use of a silicon oxide mask to cover the substrate between the designated NW positions is another concept used in Ga-assisted growth that holds promise; however, in order to properly mimic this effect, the droplet should fill the hole that exposes the Si(111) surface prior to growth, otherwise crawling behavior can still occur. A secondary benefit of using an oxide template is the reduction and possible elimination of thin film growth between the NWs. The elimination of the 2D film everywhere should enhance uniformity and reduce possible electronic transport issues [123].

The behavior of the VLS droplet during the formation of hetero-interfaces was elucidated qualitatively in Chapter 5. Further work to make a quantitative model would be a daunting but highly beneficial endeavor. The first step in making the model in

Chapter 5 more quantitative would require a Ga diffusion model to replace β and R_{eff} [32,46,95,124]. This model would use the existing knowledge of instantaneous growth rate and the phenomenological contribution from diffusion to estimate the concentration of Ga in the VLS droplet. This method would give quantitative insight into the droplet composition throughout growth and enable the correlation of polytypism.

A more complete theoretical formalism for Ga-assisted VLS growth was developed recently by Krogstrup et al. [35,71]. The Ga-As alloy droplet that develops during Ga-assisted growth is in many aspects simplified compared to the ternary Au-Ga-As alloy droplet that develops during Au-assisted VLS growth. Therefore, the complexity of such a formalism of Au-assisted growth would be great and the addition of different group V species would aggravate the complexity further; however, the benefits of such an approach can be numerous. With the proper experimental determination of many surface properties and transition state variables, a complete formalism can describe not only the flow of adatoms to the droplet, but the droplet composition, shape, and contact angle as a function of position on the NW top facet. These parameters are critical for determining the nucleation probability along the TPL and therefore the crystal structure. With the careful calibration of such a model, phase pure NWs may be realized along with the control to grow precise layered structures without transient effects.

7 Bibliography

[1] K. Hiruma, T. Katsuyama, K. Ogawa, M. Koguchi, H. Kakibayashi, and G. P. Morgan, Appl Phys Lett **59**, 431 (1991).

[2] M. Yazawa, M. Koguchi, A. Muto, M. Ozawa, and K. Hiruma, Appl Phys Lett **61**, 2051 (1992).

[3] M. C. C. Plante and R. R. R. LaPierre, J Cryst Growth **286**, 394 (2006).

[4] L. E. Jensen, M. T. Björk, S. Jeppesen, A. I. Persson, B. J. Ohlsson, L. Samuelson, and M. T. Bjork, Nano Letters **4**, 1961 (2004).

[5] R. S. Wagner and W. C. Ellis, Appl Phys Lett **4**, 89 (1964).

[6] M. S. Gudiksen, L. J. Lauhon, J. Wang, D. C. Smith, and C. M. Lieber, Nature **415**, 617 (2002).

[7] D. M. Cornet and R. R. LaPierre, Nanotechnology **18**, 385305 (2007).

[8] C. Chen, S. Shehata, C. C. Fradin, R. LaPierre, C. Couteau, and G. Weihs, Nano Letters **7**, 2584 (2007).

[9] P. K. Mohseni, A. D. Rodrigues, J. C. Galzerani, Y. A. Pusep, and R. R. LaPierre, J Appl Phys **106**, 124306 (2009).

[10] K. A. Dick, P. Caroff, J. Bolinsson, M. E. Messing, J. Johansson, K. Deppert, L. R. Wallenberg, and L. Samuelson, Semicond. Sci. Technol. **25**, 024009 (2010).

[11] J. B. Wagner, N. Sköld, L. Reine Wallenberg, and L. Samuelson, J Cryst Growth **312**, 1755 (2010).

[12] H.-Y. Chang, L. Tsybeskov, S. Sharma, T. I. Kamins, X. Wu, and D. J. Lockwood, Appl Phys Lett **95**, 133120 (2009).

[13] D. L. Dheeraj, G. Patriarche, H. Zhou, T. B. Hoang, A. F. Moses, S. Grønsberg, A. T. J. van Helvoort, B. Fimland, and H. Weman, Nano Letters **8**, 4459 (2008).

[14] T. Kuykendall, P. Ulrich, S. Aloni, and P. Yang, Nature Materials **6**, 951 (2007).

[15] C. Xu, L. Xue, C. Yin, and G. Wang, Physica Status Solidi (a) **198**, 329 (2003).

[16] C. P. T. Svensson, T. Mårtensson, J. Trägårdh, C. Larsson, M. Rask, D. Hessman, L. Samuelson, J. Ohlsson, T. Martensson, and J. Tragardh, Nanotechnology **19**, 305201 (2008).

[17] F. Qian, S. Gradecak, Y. Li, C.-Y. Y. Wen, and C. M. Lieber, Nano Letters **5**, 2287 (2005).

[18] F. Qian, Y. Li, S. Gradecak, H. Park, Y. Dong, Y. Ding, Z. L. Wang, and C. M. Lieber, Nature Materials **7**, 701 (2008).

[19] M. P. van Kouwen, M. H. M. van Weert, M. E. Reimer, N. Akopian, U. Perinetti, R. E. Algra, E. P. A. M. Bakkers, L. P. Kouwenhoven, and V. Zwiller, Appl Phys Lett **97**, 113108 (2010).

[20] J. A. Czaban, D. A. Thompson, and R. R. LaPierre, Nano Letters **9**, 148 (2009).

[21] R. R. LaPierre, a. C. E. Chia, S. J. Gibson, C. M. Haapamaki, J. Boulanger, R. Yee, P. Kuyanov, J. Zhang, N. Tajik, N. Jewell, and K. M. a. Rahman, Physica Status Solidi (RRL) - Rapid Research Letters **16**, (2013).

[22] J. Wallentin, N. Anttu, D. Asoli, M. Huffman, I. Aberg, M. H. Magnusson, G. Siefer, P. Fuss-Kailuweit, F. Dimroth, B. Witzigmann, H. Q. Xu, L. Samuelson, K. Deppert, and M. T. Borgström, Science (New York, N.Y.) **339**, 1057 (2013).

[23] F. Patolsky, G. Zheng, and C. M. Lieber, Analytical Chemistry **78**, 4260 (2006).

[24] T. Bryllert, L. E. Wernersson, T. Lowgren, and L. Samuelson, Nanotechnology **17**, S227 (2006).

[25] M. Egard, S. Johansson, A.-C. Johansson, K.-M. Persson, A. W. Dey, B. M. Borg, C. Thelander, L.-E. Wernersson, and E. Lind, Nano Letters **10**, 809 (2010).

[26] Y. Li, J. Xiang, F. Qian, S. Gradecak, Y. Wu, H. Yan, D. A. Blom, and C. M. Lieber, Nano Letters **6**, 1468 (2006).

[27] M. T. Björk, B. J. Ohlsson, T. Sass, A. I. Persson, C. Thelander, M. H. Magnusson, K. Deppert, L. R. Wallenberg, L. Samuelson, and M. T. Bjork, Appl Phys Lett **80**, 1058 (2002).

[28] H. a Nilsson, T. Duty, S. Abay, C. Wilson, J. B. Wagner, C. Thelander, P. Delsing, and L. Samuelson, Nano Letters **8**, 872 (2008).

[29] P. K. Mohseni, C. Maunders, G. A. Botton, and R. R. LaPierre, Nanotechnology **18**, 445304 (6 pp.) (2007).

[30] M. C. Plante and R. R. LaPierre, J. Appl. Phys. **105**, 114304 (2009).

[31] V. G. Dubrovskii, G. E. Cirlin, and V. M. Ustinov, Semiconductors **43**, 1539 (2009).

[32] J. C. Harmand, F. Glas, and G. Patriarche, Phys. Rev. B: Condens. Matter Mater. Phys. **81**, (2010).

[33] F. Glas, J. Harmand, and G. Patriarche, Phys. Rev. Lett. **104**, 2 (2010).

[34] V. G. Dubrovskii, Phys. Rev. B: Condens. Matter Mater. Phys. **87**, 195426 (2013).

[35] P. Krogstrup, H. I. Jørgensen, E. Johnson, M. H. Madsen, C. B. Sørensen, A. F. i Morral, M. Aagesen, J. Nygård, and F. Glas, 63 (2013).

[36] A. I. Persson, M. W. Larsson, S. Stenström, B. J. Ohlsson, L. Samuelson, L. R. Wallenberg, and S. Stenstrom, Nature Materials **3**, 677 (2004).

[37] S. Gibson and R. LaPierre, Physica Status Solidi (RRL) - Rapid Research Letters n/a (2013).

[38] F. Glas, J. Harmand, and G. Patriarche, Phys. Rev. Lett. **99**, 146101 (2007).

[39] P. Krogstrup, S. Curiotto, E. Johnson, M. Aagesen, J. Nygård, and D. Chatain, Phys. Rev. Lett. **106**, 1 (2011).

[40] V. G. Dubrovskii, N. V Sibirev, J. C. Harmand, and F. Glas, Phys. Rev. B: Condens. Matter Mater. Phys. **78**, 1 (2008).

[41] V. G. Dubrovskii and N. V Sibirev, J. Cryst. Growth **304**, 504 (2007).

[42] K. Hiruma, M. Yazawa, K. Haraguchi, K. Ogawa, T. Katsuyama, M. Koguchi, and H. Kakibayashi, J. Appl. Phys. **74**, 3162 (1993).

[43] E. Uccelli, J. Arbiol, C. Magen, P. Krogstrup, E. Russo-averchi, and M. Heiss, 1 (n.d.).

[44] M. C. C. Plante and R. R. R. LaPierre, J Cryst Growth **310**, 356 (2008).

[45] M. C. Plante and R. R. Lapierre, Nanotechnology **19**, 495603 (2008).

[46] V. G. Dubrovskii, N. Sibirev, G. Cirlin, A. Bouravleuv, Y. Samsonenko, D. Dheeraj, H. Zhou, C. Sartel, J. Harmand, G. Patriarche, and F. Glas, Phys. Rev. B: Condens. Matter Mater. Phys. **80**, 1 (2009).

[47] V. G. Dubrovskii, N. V Sibirev, G. E. Cirlin, J. C. Harmand, and V. M. Ustinov, Physical Review E **73**, 021603 (2006).

[48] C. Chatillon, F. Hodaj, and A. Pisch, J Cryst Growth **311**, 3598 (2009).

[49] a. C. E. Chia, M. Tirado, Y. Li, S. Zhao, Z. Mi, D. Comedi, and R. R. LaPierre, J Appl Phys **111**, 094319 (2012).

[50] C. M. Haapamaki, J. Baugh, and R. R. LaPierre, Journal of Applied Physics **112**, 124305 (2012).

[51] J. P. Boulanger and R. R. LaPierre, J Cryst Growth **332**, 21 (2011).

[52] P. K. Mohseni and R. R. LaPierre, Nanotechnology **20**, 025610 (2009).

[53] Y. Kim, H. J. Joyce, Q. Gao, H. H. Tan, and C. Jagadish, in *2005 IEEE LEOS Annual Meeting* (IEEE, Sydney, NSW, Australia, 2005), pp. 471–472.

[54] M. Jeppsson, K. A. Dick, J. B. Wagner, P. Caroff, K. Deppert, L. Samuelson, and L.-E. Wernersson, J Cryst Growth **310**, 4115 (2008).

[55] P. Caroff, M. E. Messing, B. Mattias Borg, K. A. Dick, K. Deppert, and L. Wernersson, Nanotechnology **20**, 495606 (2009).

[56] C. M. Haapamaki, J. Baugh, and R. R. LaPierre, Journal of Crystal Growth **345**, 11 (2012).

[57] C. M. Haapamaki and R. R. Lapierre, Nanotechnology **22**, 335602 (2011).

[58] K. L. Kavanagh, Semicond. Sci. Technol. **25**, 024006 (2010).

[59] L. C. Chuang, M. Moewe, C. Chase, N. P. Kobayashi, C. Chang-Hasnain, and S. Crankshaw, Appl Phys Lett **90**, 043115 (2007).

[60] G. E. Cirlin, V. G. Dubrovskii, I. P. Soshnikov, N. V Sibirev, Y. B. Samsonenko, A. D. Bouravleuv, J. C. Harmand, and F. Glas, Physica Status Solidi (RRL) - Rapid Research Letters **3**, 112 (2009).

[61] F. Glas, Phys. Rev. B: Condens. Matter Mater. Phys. **74**, 2 (2006).

[62] S. Raychaudhuri and E. T. Yu, Journal of Vacuum Science & Technology B: Microelectronics and Nanometer Structures **24**, 2053 (2006).

[63] S. Raychaudhuri and E. T. Yu, J Appl Phys **99**, 114308 (2006).

[64] E. Ertekin, P. A. Greaney, D. C. Chrzan, and T. D. Sands, J Appl Phys **97**, 114325 (2005).

[65] D. Kriegner, C. Panse, B. Mandl, K. A. Dick, M. Keplinger, J. M. Persson, P. Caroff, D. Ercolani, L. Sorba, F. Bechstedt, J. Stangl, and G. Bauer, Nano Letters **11**, 1483 (2011).

[66] H. J. Joyce, J. Wong-Leung, Q. Gao, H. H. Tan, and C. Jagadish, Nano Letters **10**, 908 (2010).

[67] P. Krogstrup, R. Popovitz-Biro, E. Johnson, M. H. Madsen, J. Nygård, and H. Shtrikman, Nano Letters **10**, 4475 (2010).

[68] B. Mandl, K. A. Dick, D. Kriegner, M. Keplinger, G. Bauer, J. Stangl, and K. Deppert, Nanotechnology **22**, 145603 (2011).

[69] D. Dheeraj, H. Zhou, A. Moses, and T. Hoang, in *Intechopen.com* (2010).

[70] C.-Y. Y. Yeh, Z. W. Lu, S. Froyen, and A. Zunger, Phys. Rev. B: Condens. Matter Mater. Phys. **46**, 10086 (1992).

[71] P. Krogstrup, Dynamical Theory and Experiments on GaAs Nanowire Growth for Photovoltaic Applications, University of Copenhagen, 2012.

[72] Y. Hu, M. Li, J.-J. He, and R. R. LaPierre, Nanotechnology **24**, 065402 (2013).

[73] Y. Hu, R. R. LaPierre, M. Li, K. Chen, and J.-J. He, J Appl Phys **112**, 104311 (2012).

[74] a C. E. Chia and R. R. LaPierre, Nanotechnology **22**, 245304 (2011).

[75] M. C. C. Plante and R. R. R. LaPierre, J. Cryst. Growth **310**, 356 (2008).

[76] J. P. Boulanger and R. R. LaPierre, Semicond. Sci. Technol. **27**, 035002 (2012).

[77] M. B. Panish, B. Laboratories, M. Hill, and L. N. Gun, J. Elecrochem. Soc.: Solid-State Science and Technology **127**, 2729 (1980).

[78] M. B. Panish and H. Temkin, *Gas Source Molecular Beam Epitaxy* (Springer-Verlag, Berlin and Heidelberg, 1993), p. 442.

[79] M. E. Messing, K. Hillerich, J. Bolinsson, K. Storm, J. Johansson, K. A. Dick, and K. Deppert, Nano Research **3**, 506 (2010).

[80] D. B. Williams and C. B. Carter, *Transmission Electron Microscopy : a Textbook for Materials Science* (Plenum Press, New York, 1996), p. 729.

[81] N. Yao and Z. Wang, *Handbook of Microscopy for Nanotechnology* (2005).

[82] J. Schindelin, I. Arganda-Carreras, E. Frise, V. Kaynig, M. Longair, T. Pietzsch, S. Preibisch, C. Rueden, S. Saalfeld, B. Schmid, J.-Y. Tinevez, D. J. White, V. Hartenstein, K. Eliceiri, P. Tomancak, and A. Cardona, Nat. Methods **9**, 676 (2012).

[83] S. Preibisch, S. Saalfeld, and P. Tomancak, Bioinformatics (Oxford, England) **25**, 1463 (2009).

[84] T. Mårtensson, M. Borgström, W. Seifert, B. J. Ohlsson, and L. Samuelson, Nanotechnology **14**, 1255 (2003).

[85] T. Martensson, P. Carlberg, M. Borgstrom, L. Montelius, W. Seifert, L. Samuelson, T. Mårtensson, and M. Borgström, Nano Letters **4**, 699 (2004).

[86] A. Pierret, M. Hocevar, S. L. Diedenhofen, R. E. Algra, E. Vlieg, E. C. Timmering, M. A. Verschuuren, G. W. G. Immink, M. A. Verheijen, and E. P. A. M. Bakkers, Nanotechnology **21**, 065305 (2010).

[87] Z. H. Wu, X. Y. Mei, D. Kim, M. Blumin, and H. E. Ruda, Appl. Phys. Lett. **81**, 5177 (2002).

[88] B. Fuhrmann, H. S. Leipner, H.-R. Höche, L. Schubert, P. Werner, and U. Gösele, Nano Letters **5**, 2524 (2005).

[89] C. Tseng, M. J. Tambe, S. K. Lim, M. J. Smith, and S. Gradecak, Nanotechnology **21**, 165605 (2010).

[90] S. C. Ghosh, P. Kruse, and R. R. LaPierre, Nanotechnology **20**, 115602 (2009).

[91] K. A. Dick, K. Deppert, L. Samuelson, L. R. Wallenberg, and F. M. Ross, Nano Letters **8**, 4087 (2008).

[92] E. Uccelli, J. Arbiol, C. Magen, P. Krogstrup, E. Russo-Averchi, M. Heiss, G. Mugny, F. Morier-Genoud, J. Nygård, J. R. Morante, and A. Fontcuberta I Morral, Nano Letters **11**, 3827 (2011).

[93] S. Breuer, M. Hilse, A. Trampert, L. Geelhaar, and H. Riechert, Phys. Rev. B: Condens. Matter Mater. Phys. **82**, 075406 (2010).

[94] R. W. Olesinski, N. Kanani, and G. J. Abbaschian, Bulletin of Alloy Phase Diagrams **6**, 362 (1985).

[95] V. G. Dubrovskii, N. Sibirev, G. Cirlin, I. Soshnikov, W. H. Chen, R. Larde, E. Cadel, P. Pareige, T. Xu, B. Grandidier, J.-P. Nys, D. Stievenard, M. Moewe, L. Chuang, and C. Chang-Hasnain, Phys. Rev. B: Condens. Matter Mater. Phys. **79**, 1 (2009).

[96] N. V. Sibirev, V. G. Dubrovskii, G. E. Cirlin, V. a. Egorov, Y. B. Samsonenko, and V. M. Ustinov, Semiconductors **42**, 1259 (2009).

[97] M. C. Plante and R. R. LaPierre, J. Appl. Phys. **105**, 114304 (2009).

[98] R. Kilaas, Journal of Microscopy **190**, 45 (1998).

[99] J. Johansson, C. P. T. Svensson, T. Martensson, L. Samuelson, W. Seifert, and T. Mårtensson, The Journal of Physical Chemistry. B **109**, 13567 (2005).

[100] J. Johansson, B. A. Wacaser, K. A. Dick, and W. Seifert, Nanotechnology **17**, S355 (2006).

[101] A. Fakhr, Y. M. Haddara, and R. R. Lapierre, Nanotechnology **21**, 165601 (2010).

[102] X. Ren, H. Huang, V. G. Dubrovskii, N. V Sibirev, M. V Nazarenko, A. D. Bolshakov, X. Ye, Q. Wang, Y. Huang, X. Zhang, J. Guo, and X. Liu, Semicond. Sci. Technol. **26**, 014034 (2011).

[103] G. Zhang, K. Tateno, H. Gotoh, T. Sogawa, and H. Nakano, Japanese Journal of Applied Physics **49**, 015001 (2010).

[104] R. E. Algra, M. A. Verheijen, L.-F. Feiner, G. G. W. Immink, J. P. Van Enckevort, E. Vlieg, E. P. A. M. Bakkers, and W. J. P. van Enckevort, Nano Letters **11**, 1259 (2011).

[105] D. Lucot, F. Jabeen, J.-C. Harmand, G. Patriarche, R. Giraud, G. Faini, and D. Mailly, Appl Phys Lett **98**, 142114 (2011).

[106] S. Plissard, G. Larrieu, X. Wallart, and P. Caroff, Nanotechnology **22**, 275602 (2011).

[107] D. A. Muller, T. Sorsch, S. Moccio, F. H. Baumann, and G. Timp, **399**, (1999).

[108] A. Hiraki, M.-A. Nicolet, and J. . Mayer, Appl Phys Lett **18**, 178 (1971).

[109] A. Hiraki, E. Lugujjo, and J. W. Mayer, J Appl Phys **43**, 3643 (1972).

[110] A. L. Roest, M. A. Verheijen, O. Wunnicke, S. Serafin, H. Wondergem, and E. P. A. M. Bakkers, Nanotechnology **17**, S271 (2006).

[111] N. Clément, G. Patriarche, K. Smaali, F. Vaurette, K. Nishiguchi, D. Troadec, A. Fujiwara, and D. Vuillaume, Small **7**, 2607 (2011).

[112] S. F. Fang, K. Adomi, S. Iyer, H. Morkoç, H. Zabel, C. Choi, and N. Otsuka, J Appl Phys **68**, R31 (1990).

[113] L. Vj, J. Oh, A. P. Nayak, A. M. Katzenmeyer, K. H. Gilchrist, S. Grego, N. P. Kobayashi, S.-Y. Wang, a. A. Talin, N. K. Dhar, and M. S. Islam, IEEE J Sel Top Quantum Electron **17**, 1002 (2011).

[114] M. S. Kang, C.-H. Lee, J. B. Park, H. Yoo, and G.-C. Yi, Nano Energy **1**, 391 (2012).

[115] K. A. Dick, Progress in Crystal Growth and Characterization of Materials **54**, 138 (2008).

[116] X. Zhuang, C. Z. Ning, and A. Pan, Adv Mater **24**, 13 (2012).

[117] Q. Gap, H. Joyce, Y. Kim, H. H. Tan, C. Jagadish, H. Wang, Y. N. Guo, and J. Zou, in *2007 International Workshop on Physics of Semiconductor Devices (IWPSD ’07)* (IEEE, Mumbai, India, 2007), p. 344.

[118] M. Tchernycheva, L. Travers, G. Patriarche, F. Glas, J.-C. C. Harmand, G. E. Cirlin, and V. G. Dubrovskii, J. Appl. Phys. **102**, 94313 (2007).

[119] F. Jabeen, G. Patriarche, F. Glas, and J.-C. Harmand, J Cryst Growth **323**, 293 (2011).

[120] J. C. Harmand, G. Patriarche, N. Péré-Laperne, M.-N. Mérat-Combes, L. Travers, and F. Glas, Appl Phys Lett **87**, 203101 (2005).

[121] J. Johansson, L. S. Karlsson, C. P. T. Svensson, T. Martensson, B. A. Wacaser, K. Deppert, L. Samuelson, and W. Seifert, Nature Mater. **5**, 574 (2006).

[122] F. Glas, Journal of Applied Physics **108**, 073506 (2010).

[123] R. R. LaPierre, J Appl Phys **109**, 034311 (2011).

[124] V. G. Dubrovskiĭ, N. V. Sibirev, R. a. Suris, G. É. Cirlin, V. M. Ustinov, M. Tchernysheva, and J. C. Harmand, Semiconductors **40**, 1075 (2006).

8 Appendix

8.1 Appendix A: Affine Transform Matlab Code

The Matlab code for correcting image drift using electron microscopy techniques that record in a serial nature. This program requires that you know the direction of the drift. It is beneficial to place this direction entirely along the x or y axis. The code below demonstrates this for a drift in the x-axis (x=-0.03).

```
I = imread('Title_of_Input_Image.tif');
% Variables to adjust affine matrix
x = -0.03;
y = 0;
tform = maketform('affine',[1 y 0; x 1 0; 0 0 1]);
J = imtransform(I,tform);
imshow(I), figure, imshow(J)
imwrite(J,'Title_of_Output_Image.tif','tif')
```

8.2 Appendix B: Electron Beam Lithography Procedure

The standard EBL preparation and development procedure for use with the EBPG 5000+ EBL instrument at the University of Toronto:

Procedure Step	**Description**
RCA Cleaning (optional):	Piranha etch • Pour 100 mL of H_2SO_4 (sulfuric acid) in a glass beaker • Slowly add 100 mL H_2O_2 (beaker will get hot) • Carefully place beaker on a hot plate at 90°C to ensure the reaction continues • Place the wafer in a basket and into the solution for 10 min • Rinse with DI water and dry with N_2 or keep submerged until the next etch HCL Etch • 100 mL of DI water in glass beaker • Add 25 mL HCL to DI water

	• Add 25 mL of H_2O_2 (beaker will get hot) • Place on hot plate at 90°C to ensure the reaction continues • Place a wafer in a basket into the solution for 10 min • Rinse the wafer thoroughly with DI water and dry with N_2 or keep submerged until the next etch Buffered HF (BHF) Etch • Add enough 10% BHF to submerge the wafer in a basket • Etch for 1 min • Rinse with DI water and N_2 dry
Oxide (optional):	• Deposit or grow thermally
Cleaning Prior to Spinning Resist	• 1 min ultrasonication in acetone • 1 min ultrasonication in IPA • N_2 Dry
Resist Coating:	• Set hotplate to 180°C • Set spinner to 6000 RPM, acceleration to 587, duration to 60 s • Dispense enough ZEP-520A to create a droplet half the diameter of the substrate • After the resist spin, immediately bake for 3 min at 180°C
Development:	• In two beakers pour ZEP-N50 and MIBK:IPA 90:10 • Place substrate in ZEP-N50 for 60 s and gently agitate • Move to MIBK:IPA beaker for 30 s • N_2 dry • Check Pattern with light microscope
Etch and Metallization:	• Prior to metallization, conduct an O_2 barrel ash for 20 s at 100 W • Place substrate in a buffered HF etch for 30 s (adjust time or etch method if a thick oxide was deposited prior) • Rinse and N_2 dry • Load wafer into load lock and pump down in less than 10 min to avoid oxide reformation • Metallize with Au (~20nm Au)
Lift-off	• Soak in ZD-MAC • If resist does not removal is not effortless, ultrasonication at elevated temperatures is recommended • Rinse and ultrasonication in acetone • Rinse and ultrasonication in IPA • O_2 plasma ash for 120 s at 100 W

Subsequent Cleaning (if organic residue persists):	• 20s dip in H_2SO_4:H_20 1:1 mixture
Immediately Prior to MBE Loading:	• 30 s 10% BHF etch • Rinse in DI water and N_2 dry • Immediately load into MBE load lock and evacuate chamber

8.3 Appendix C: Phenomenological Model Matlab Code

A phenomenological model was presented in Chapter 5. The matlab code below fit β and R_{eff} as well as calculated the contributions from direct impingement, sidewall diffusion, and substrate diffusion to axial VLS growth. The first file was the "launcher" file, which contains specific information about the nanowire and calls the growth rate and length data from an excel file. Each GaAs or GaP segment has its own excel file. For the case of growth 1384 (sample C), there were 2 files.

```
%% Clear and Close All Windows
close all
clear all

%% Select Which Model to Run
g=1;         only Beta is fit and R_eff is introduced if Beta=1 is
insufficient
segnum=2;    %Number of GaAs & GaP segments in NW
%% Set Model Parameters
for z=1:segnum

seg=z;
segstr=num2str(seg);

ExcelName='1384_D3_NW3';
if g==0
VariableName=[ExcelName '_G0'];
else
VariableName=[ExcelName '_G1'];
end
experimantalDataFilename=['NW-DATA\' ExcelName '-seg' segstr
'.xlsx']
str=date;
```

```
str2=datestr(datenum(str,'dd-mmm-yyyy'),'yyyy-mmm-dd');
VariableNameDate=[VariableName '-' str2];
direxists=exist(VariableNameDate,'dir');
if direxists==0
    mkdir(VariableNameDate);
end
variableOutputFilename=[VariableNameDate '\' VariableNameDate
'.xlsx'];

% Relevant NW Measurements  ***Change For Each Wire***
R_NW=52.5/2;
R_Au=54.1/2;
if seg==1
p=0;                    %GaAs NW growth p=0, GaP NW growth p=1
else
    p=1;
end

%Decide which column you want to compare the data against
wireColumn=2;           %Usually 1 + wire number
m=0;                    %number of missing cells at the beginning
DeltaHwMAX=0.6;         %Max DeltaHw to show in plots

if g==0
n=500;                  %resolution of iterations for Beta, R_eff
Beta_min=0;
Beta_max=1-Beta_min;
R_max=50;               %Maximum radius in nm around NW for
diffusion on substrate
H_xmax=100;             %If substrate absorbs sidewall adatoms,
H_x is the location of the maximum sidewall chemical potential
difference
NumFits=500;            %Select the number of fits to show
GrowthRateFittingG0
else
n=200;                  %resolution of iterations for Beta
Beta_min=0;
Beta_max=1-Beta_min;
R_max=50;               %Maximum radius in nm around NW for
diffusion on substrate

GrowthRateFittingG1MultiSeg

if z==segnum
GrowthRateFittingG1MultiSegPlotting
else
close all
clearvars -except segnum seg z g FinalRes
end
end
end
```

Below is the code referred to as "GrowthRateFittingG1MultiSeg" that finds the best β and R_{eff} fit for each instantaneous growth rate data point.

```
% Model Constants
alpha=35*pi/180;            %Impingement angle of Ga source in
radians
V=0.25*1000/3600;           %0.25um/h planar growth Rate in nm/s
for (100) GaAs
eta_A=0.95;                 %Fraction of nominal film growth rate
dH_f=V*eta_A;               %(111) film growth rate
chi_A=1;                    %Fraction of adatoms that directly
impinge on the droplet that contribute to growth
omega_GaAs=0.0452;          %Atomic volume of Ga in GaAs
omega_GaP=0.0405;           %Atomic volume of Ga in GaP
omega_GaAs100=omega_GaAs;   %Atomic volume of Ga in (100) GaAs
film calibration

if p==0
    omega_NW=omega_GaAs;    %Atomic volume of Ga in GaAs
elseif p==1
    omega_NW=omega_GaP;     %Atomic volume of Ga in GaP
end

% Fitting Variables
% H_w0=                     The NW height at the first oscillation
% Beta=                     Fraction of adatoms that impinge on
the NW and sidewall and contribute to aBetaal NW growth
% R_eff=                    Diffusion length on the substrate
surface to the NW

%% Import Experimental Data Sets
[experimental] = xlsread(experimantalDataFilename);

%This input is based on constant format of file
t=(experimental(:,1))';
DeltaHw_exp=(experimental(:,wireColumn))';
Hw_exp=(experimental(:,wireColumn+1))';
%Edit to Remove blanks
filelength=length(t);
for a=1:filelength;
        if isnan(DeltaHw_exp(a))
            DeltaHw_exp(a)=[];
            t(a)=[];
        end
end
filelength=length(t);

%% Iterate and Check Fit
```

```
%Define variables - values will be redefined later during
iterations
Beta=0;                    %defines Beta with a temporary value
H_x=0;                    %defines H_x with a temporary value
R_eff=0;                 %defines R_NW with a temporary value
FinalResults=zeros(filelength,13); %preallocate the results matrix
in memory
Error=zeros(1,filelength);  %predefine Error variable

%Impingement and growth surface area factor
PreFactor=(V*omega_NW/(omega_GaAs100*pi*R_NW^2));

%Account for thin film growth and height
H_f0=dH_f*30*60;            %Film height during the first
oscillation

%Define adatom pathways and initial NW height:

%Direct Impingement
DirectImpingementNWGR=PreFactor*(chi_A*pi*R_Au^2/cos(alpha));

%Initial NW height estimate
if seg==1
    InitialNWGR=DeltaHw_exp(m+1);
    H_w0= ((DirectImpingementNWGR + InitialNWGR)/2)*(30+m)*60;
%Nanowire height during the first oscillation
else
    H_w0=FinalRes{1,1}(1,5);
end

b=1;
Error=zeros(1,n);      %predefine Error variable
Output=zeros(8,n);   %predefine Betasave variable
DeltaHw_check=zeros(filelength,filelength);

%Direct Impingement
DirectImpingementNWGR=PreFactor*(chi_A*pi*R_Au^2/cos(alpha));

for b=1:filelength
loading=strcat(num2str(100*b/filelength),'%') %Progress bar
k=0;
H_fb=dH_f*t(b) + H_f0;          %Film height at time "t"
MAXSidewallNWGR(b)=PreFactor*(2*R_NW*tan(alpha)*(H_w0+Hw_exp(b)-
H_fb));
MAX_GR(b)=DirectImpingementNWGR+MAXSidewallNWGR(b);
if DeltaHw_exp(b)<= MAX_GR(b)
    for i=1:n                %Step Beta from 0 to 1 in n-steps
        k=1;
        Beta=Beta_max*i/n+Beta_min;
        R_eff=0;
        Output(1,i)=Beta;
        Output(2,i)=R_eff;
```

```
        %Sidewall Impingement and diffusion to the droplet

SidewallNWGR=PreFactor*(2*Beta*R_NW*tan(alpha)*(H_w0+Hw_exp(b)-
H_fb));
        SubstrateNWGR=0;

        %Equation to check fit against the experimental data:
        DeltaHw_check(b,i)= DirectImpingementNWGR + SidewallNWGR +
SubstrateNWGR;

        Output(3,i) =((DeltaHw_check(b,i)-
DeltaHw_exp(b))^2)/(DeltaHw_exp(b))^2;
        Output(4,i) = DirectImpingementNWGR;
        Output(5,i) = SidewallNWGR;
        Output(6,i) = SubstrateNWGR;
        Output(7,i) = DeltaHw_check(b,i);
        Output(8,1) = DeltaHw_exp(b);
    end
else
    for i=1:n              %Step Beta from 0 to 1 in n-steps
        Beta=1;
        R_eff=R_max*i/n;
        Output(1,i)=Beta;
        Output(2,i)=R_eff;

        %Sidewall Impingement and diffusion to the droplet

SidewallNWGR=PreFactor*(2*Beta*R_NW*tan(alpha)*(H_w0+Hw_exp(b)-
H_fb));

        %Substrate Impingement and diffusion to the droplet
        SubstrateNWGR=PreFactor*(2*pi*R_eff^2);

        %Equation to check fit against the experimental data:
        DeltaHw_check(b,i)= DirectImpingementNWGR + SidewallNWGR +
SubstrateNWGR;

        Output(3,i) =((DeltaHw_check(b,i)-
DeltaHw_exp(b))^2)/(DeltaHw_exp(b))^2;
        Output(4,i) = DirectImpingementNWGR;
        Output(5,i) = SidewallNWGR;
        Output(6,i) = SubstrateNWGR;
        Output(7,i) = DeltaHw_check(b,i);
        Output(8,1) = DeltaHw_exp(b);
    end
end
[Y,I]=sort(Output(3,:),'ascend');
SortedOutput=Output(:,I);
Beta=SortedOutput(1,1);
```

```
NWHeight=(H_w0+Hw_exp(b)-H_fb);

H_x=Beta*NWHeight;

R_eff=SortedOutput(2,1);
ErrorMin=SortedOutput(3,1);
DirectImpingementNWGR=SortedOutput(4,1);
SidewallNWGR=SortedOutput(5,1);
SubstrateNWGR=SortedOutput(6,1);
DeltaHw_check1=SortedOutput(7,1);
%Output results in a matrix
%Error is represented as 1/sum(Error) for plotting
FinalOutput(b,:)=[t(b) Beta H_x R_eff H_w0 1/ErrorMin
DirectImpingementNWGR SidewallNWGR SubstrateNWGR Hw_exp(b)
DeltaHw_exp(b) DeltaHw_check1  NWHeight];
end
FinalRes{z}=FinalOutput;
disp(['DONE!' 'seg' segstr]);
```

The following code is referred to as "GrowthRateFittingG1MultiSegPlotting", which saves the fitting data in an excel file and creates several plots for easy assessment:

```
%% Plot the Results

col = [
    0.00  0.00  1.00
    0.00  0.50  0.00
    1.00  0.00  0.00
    0.00  0.75  0.75
    0.75  0.00  0.75
    0.75  0.75  0.00
    0.25  0.25  0.25
    0.75  0.25  0.25
    0.75  0.75  0.75
];
colg0=[0.00  0.75  0.00];
colb0=[0.00  0.00  0.75];
colr0=[0.75  0.00  0.00];
if segnum==9
col1=[  1.00  1.00  1.00
    0.00  0.50  0.00
    1.00  1.00  1.00
    0.00  0.75  0.75
    1.00  1.00  1.00
    0.75  0.75  0.00
    1.00  1.00  1.00
```

```
    0.75  0.25  0.25
    1.00  1.00  1.00
];
colg=[  1.00  1.00  1.00
    0.00  0.75  0.00
    1.00  1.00  1.00
    0.00  0.75  0.00
    1.00  1.00  1.00
    0.00  0.75  0.00
    1.00  1.00  1.00
    0.00  0.75  0.00
    1.00  1.00  1.00
];
colb=[  1.00  1.00  1.00
    0.00  0.00  0.75
    1.00  1.00  1.00
    0.00  0.00  0.75
    1.00  1.00  1.00
    0.00  0.00  0.75
    1.00  1.00  1.00
    0.00  0.00  0.75
    1.00  1.00  1.00
];
colr=[  1.00  1.00  1.00
    0.75  0.00  0.00
    1.00  1.00  1.00
    0.75  0.00  0.00
    1.00  1.00  1.00
    0.75  0.00  0.00
    1.00  1.00  1.00
    0.75  0.00  0.00
    1.00  1.00  1.00
];
else
col1=[  0.00  0.00  1.00
    1.00  1.00  1.00
    1.00  0.00  0.00
    1.00  1.00  1.00
];
colg=[  0.00  0.75  0.00
    1.00  1.00  1.00
    0.00  0.75  0.00
    1.00  1.00  1.00
];
colb=[  0.00  0.00  0.75
    1.00  1.00  1.00
    0.00  0.00  0.75
    1.00  1.00  1.00
];
colr=[  0.75  0.00  0.00
    1.00  1.00  1.00
    0.75  0.00  0.00
    1.00  1.00  1.00
];
```

```
end
figure_Beta_t=figure;
plot(FinalRes{1}(:,1),FinalRes{1}(:,2),'Color',col(1,:),'Marker','
o','MarkerFaceColor',col1(1,:))
axis([0,2000,0,1])
xlabel('Growth Duration (s)')
ylabel('Beta')
title('Beta vs t')
hold on
if segnum>1
for e=2:segnum

plot(FinalRes{e}(:,1),FinalRes{e}(:,2),'Color',col(e,:),'Marker','
o','MarkerFaceColor',col1(e,:))
end
end
if segnum==1 && p==0
legend('GaAs')
elseif segnum==1 && p==1
legend('GaP')
elseif segnum==2
legend('GaAs','GaP')
elseif segnum==4
legend('GaAs1','GaP1','GaAs2','GaAs3 V/III=3')
elseif segnum==9
legend('GaP1','GaAs1','GaP2','GaAs2','GaP3','GaAs3','GaP4','GaAs4'
,'GaP5')
end
print(figure_Beta_t, '-dpng', '-r300', [VariableNameDate
'\figure_Beta_t.png']);

figure_Sidewall_Collection_Length=figure;
plot(FinalRes{1}(:,1),FinalRes{1}(:,3),'Color',colg0,'Marker','o',
'MarkerFaceColor',colg(1,:))
xlabel('Growth Duration (s)')
ylabel('Length (nm)')
title('Sidewall Collection Length')
hold on
plot(FinalRes{1}(:,1),
FinalRes{1}(:,13),'Color',colb0,'Marker','o','MarkerFaceColor',col
b(1,:))
if segnum>1
for e=2:segnum

plot(FinalRes{e}(:,1),FinalRes{e}(:,3),'Color',colg0,'Marker','o',
'MarkerFaceColor',colg(e,:))
    plot(FinalRes{e}(:,1),
FinalRes{e}(:,13),'Color',colb0,'Marker','o','MarkerFaceColor',col
b(e,:))
end
end
if segnum==1 && p==0
```

```
legend('H_x - GaAs','Nanowire Length -
GaAs','Location','NorthWest')
elseif segnum==1 && p==1
legend('H_x - GaP','Nanowire Length - GaP','Location','NorthWest')
elseif segnum==9
legend('H_x - GaP','Nanowire Length - GaP','H_x - GaAs','Nanowire
Length - GaAs','Location','NorthWest');
else
legend('H_x - GaAs','Nanowire Length - GaAs','H_x - GaP','Nanowire
Length - GaP','Location','NorthWest');
% elseif segnum==4
% legend('H_x - GaAs1','Nanowire Length - GaAs1','H_x -
GaP1','Nanowire Length - GaP1','H_x - GaAs2','Nanowire Length -
GaAs2','H_x - GaAs3 V/III=3','Nanowire Length - GaAs3
V/III=3','Location','NorthWest');
% elseif segnum==9
% legend('H_x - GaP1','Nanowire Length - GaP1','H_x -
GaAs1','Nanowire Length - GaAs1','H_x - GaP2','Nanowire Length -
GaP2','H_x - GaAs3','Nanowire Length - GaAs3','H_x -
GaP4','Nanowire Length - GaP4','H_x - GaAs4','Nanowire Length -
GaAs4','H_x - GaP1','Nanowire Length -
GaP1','Location','NorthWest');
end

print(figure_Sidewall_Collection_Length, '-dpng', '-r300',
[VariableNameDate '\figure_Sidewall_Collection_Length.png']);

% figure_DeltaHw_exp_DeltaHw_check=figure;
%
plot(FinalRes{1}(:,1),FinalRes{1}(:,11),'r',FinalRes{1}(:,1),Final
Res{1}(:,12),':b')
% axis([0,2000,0,DeltaHwMAX])
% title('DeltaHw_{exp} with Fit')
% xlabel('Growth Duration (s)')
% ylabel('Nanowire Growth Rate (nm/s)')
% hold on
% if seg>1
% for e=2:segnum
%
plot(FinalRes{e}(:,1),FinalRes{e}(:,11),'r',FinalRes{e}(:,1),Final
Res{e}(:,12),':b')
% end
% end
% legend('DeltaHw_{exp}','Fit','Location','NorthWest');
% print(figure_DeltaHw_exp_DeltaHw_check, '-dpng', '-r300',
[VariableNameDate '\figure_DeltaHw_exp_DeltaHw_check.png']);

figure_Growth_Rate_Contributions=figure;
plot(FinalRes{1}(:,1),FinalRes{1}(:,7),'Color',colb0,'Marker','o',
'MarkerFaceColor',colb(1,:))
axis([0,2000,0,DeltaHwMAX])
title('Growth Rate Contributions')
xlabel('Growth Duration (s)')
```

```
ylabel('Nanowire Growth Rate (nm/s)')
hold on
plot(FinalRes{1}(:,1),FinalRes{1}(:,8),'Color',colg0,'Marker','o',
'MarkerFaceColor',colg(1,:))
plot(FinalRes{1}(:,1),FinalRes{1}(:,9),'Color',colr0,'Marker','o',
'MarkerFaceColor',colr(1,:))
if segnum>1
for e=2:segnum

plot(FinalRes{e}(:,1),FinalRes{e}(:,7),'Color',colb0,'Marker','o',
'MarkerFaceColor',colb(e,:))

plot(FinalRes{e}(:,1),FinalRes{e}(:,8),'Color',colg0,'Marker','o',
'MarkerFaceColor',colg(e,:))

plot(FinalRes{e}(:,1),FinalRes{e}(:,9),'Color',colr0,'Marker','o',
'MarkerFaceColor',colr(e,:))
end
end
if segnum==9
legend('DirectImpingementNWGR GaP','SidewallNWGR
GaP','SubstrateNWGR GaP','DirectImpingementNWGR
GaAs','SidewallNWGR GaAs','SubstrateNWGR
GaAs','Location','NorthWest');
elseif segnum>1
legend('DirectImpingementNWGR GaAs','SidewallNWGR
GaAs','SubstrateNWGR GaAs','DirectImpingementNWGR
GaP','SidewallNWGR GaP','SubstrateNWGR
GaP','Location','NorthWest');
else
legend('DirectImpingementNWGR GaAs','SidewallNWGR
GaAs','SubstrateNWGR GaAs','Location','NorthWest');
end
title('Growth Rate Contributions')
xlabel('Growth Duration (s)')
ylabel('Nanowire Growth Rate (nm/s)')
print(figure_Growth_Rate_Contributions, '-dpng', '-r300',
[VariableNameDate '\figure_Growth_Rate_Contributions.png']);

%% Output results to an excel file

filename=variableOutputFilename;

FinalResOutputModelSettings={'n (Resolution)'; 'Beta_min';
'Beta_max'; 'chi_A'; 'eta_A'; 'H_f0'; 'H_w0'; 'p (0=GaAs,1=GaP)';
'g (1=Beta_A fit only)'};
FinalResOutputColumnTitles={'t', 'Beta', 'H_x', 'R_eff', 'H_w0',
'1/ErrorMin', 'DirectImpingementNWGR', 'SidewallNWGR',
'SubstrateNWGR', 'Hw_exp', 'DeltaHw_exp', 'DeltaHw_check1',
'NWHeight'};

xlswrite(filename, FinalResOutputModelSettings, 1, 'A1');
xlswrite(filename, n, 1, 'B1');
```

```
xlswrite(filename, Beta_min, 1, 'B2');
xlswrite(filename, Beta_max+Beta_min, 1, 'B3');
xlswrite(filename, chi_A, 1, 'B4');
xlswrite(filename, eta_A, 1, 'B5');
xlswrite(filename, H_f0, 1, 'B6');
xlswrite(filename, H_w0, 1, 'B7');
xlswrite(filename, p, 1, 'B8');
xlswrite(filename, g, 1, 'B9');
xlswrite(filename, FinalResOutputColumnTitles, 1, 'A10');

for y=1:segnum
    FinalResOutput=FinalRes{y};
    if y==1
    CellLocation{y}=11;
    else
    CellLocation{y}=CellLocation{y-1}+size(FinalRes{y-1},1);
    end
    CellLocationStr=num2str(CellLocation{y});
    xlswrite(filename, FinalResOutput, 1, ['A' CellLocationStr]);
end

disp('DONE!');
```